UNIVERSITY OF CALIFORNIA, SAN DIEGO

Buoyancy and Stratification in Boussinesq Flow with Applications to Natural Ventilation and Intrusive Gravity Currents

A dissertation submitted in partial satisfaction of the requirements for the degree Doctor of Philosophy

in

Engineering Sciences (Mechanical Engineering)

by

Morris R. Flynn

Committee in charge:

Professor Paul F. Linden, Chair
Professor Colm-cille P. Caulfield
Professor Stefan G. Llewellyn Smith
Professor W. Kendall Melville
Professor James W. Rottman
Professor William R. Young

2006

.

The dissertation of Morris R. Flynn is approved, and it is acceptable in quality and form for publication on microfilm:

Chair

University of California, San Diego

2006

Dedicated to my parents, Peter and Alida

One looks at maps, and does not truly apprehend the extent and variety of the world.

John Williams

The cold was straight from the glaciers, racing down the smoking ocean. He thrust junks of wood onto the coals, but the chimney barely drew. The wind, he thought, was blowing so hard it was like a cap over the chimney. If that was possible.

Annie Proulx

TABLE OF CONTENTS

LIST OF FIGURES

LIST OF TABLES

ACKNOWLEDGMENTS

Many people helped broaden my horizons at the University of California, San Diego. Although simple words cannot express my gratitude to these individuals, some record of their contributions is in order. First and foremost, I would like to thank my principal research supervisors Profs. Colm-cille P. Caulfield and Paul F. Linden, whose key insights, helpful suggestions and timely encouragement are reflected throughout the present studies. I am also grateful for the many positive conversations I enjoyed with Profs. James W. Rottman and William R. Young. The remaining members of my committee, Profs. Stefan G. Llewellyn Smith and W. Kendall Melville provided thoughtful feedback and criticisms during my Senate examination and annual research review meeting. I would also like to acknowledge the technical help provided by Prof. Thomas R. Bewley, Tom Chalfant and Alan Moxley as well as the collegial assistance of many fellow students, most especially Diogo Bolster, Thomas Boubarne, Devin Conroy and John Taylor. Lastly, sincere gratitude is due to my family and Heather MacNeil for their patience and on-going encouragement.

Financial support was generously provided by the following organizations: the Natural Science and Engineering Research Council of Canada, the Canadian Meteorological and Oceanographic Society, the University of California, San Diego (through an Academic Senate Research grant and a Teaching Assistantship), the Jacobs School of Engineering and the National Science Foundation through grant ATM 0222104.

Material drawn from chapter 3 has been submitted for publication to *Building and Environment*, 2006, Flynn, M. R. and C. P. Caulfield (Elsevier Science). Material drawn from chapter 4 has been published by the *Journal of Fluid Mechanics*, 2006, Flynn, M. R. and C. P. Caulfield, **564**, pp. 139–158 (Cambridge University Press). Material drawn from chapter 5 will be included as an extended abstract in the proceedings of the 6^{th} *International Symposium on Stratified Flows*,

2006, Flynn, M. R. and C. P. Caulfield (International Association of Hydraulic Engineering and Research). Material drawn from chapter 7 has been accepted for publication by the *Journal of Fluid Mechanics*, 2006, Flynn, M. R. and P. F. Linden (Cambridge University Press). Material drawn from chapter 8 has been submitted for publication to *Physics of Fluids*, 2006, Flynn, M. R., Boubarne, T. and P. F. Linden (American Physical Society). I was both the primary investigator and lead author of each of the papers described above.

VITA

1977	Born, Edmonton, Canada
2000	B.Sc. U. Alberta (Chemical Eng., Co-op)
2003	M.Sc., U. Alberta (Applied Mathematics)
2003–2006	Research Assistant, U. California, San Diego
2006	Teaching Assistant, U. California, San Diego
2006	Ph.D., U. California, San Diego (Eng. Sciences)

SELECTED PUBLICATIONS

MRF and P. F. Linden, 2006: Intrusive gravity currents. *J. Fluid Mech.*, 10 pages, in-press.

MRF and C. P. Caulfield, 2006: Natural ventilation in interconnected chambers. *J. Fluid Mech.*, **564**, 139–158.

Sutherland, B. R., **MRF** and K. Dohan, 2004: Internal wave excitation from a collapsing mixed region. *Deep-Sea Res. II*, **51**, 2889–2904.

MRF and B. R. Sutherland, 2004: Intrusive gravity currents and internal gravity wave generation in stratified fluid. *J. Fluid Mech.*, **514**, 355–383.

Sutherland, B. R., Kyba, P. J. and **MRF**, 2004: Intrusive gravity currents in two-layer fluids. *J. Fluid Mech.*, **514**, 327–353.

MRF, Onu, K. and B. R. Sutherland, 2003: Internal wave excitation by a vertically oscillating sphere. *J. Fluid Mech.*, **494**, 65–93.

FIELDS OF STUDY

Major Field: Fluid mechanics

Natural and low-energy building ventilation
Profs. Paul F. Linden and Colm-cille P. Caulfield (U. Cambridge)

Gravity current dynamics
Profs. Paul F. Linden and Bruce R. Sutherland (U. Alberta)

Linear internal gravity waves
Prof. Bruce R. Sutherland (U. Alberta)

ABSTRACT OF THE DISSERTATION

Buoyancy and Stratification in Boussinesq Flow
with Applications to Natural Ventilation and
Intrusive Gravity Currents

by

Morris R. Flynn
Doctor of Philosophy in Engineering Sciences (Mechanical Engineering)
University of California, San Diego, 2006
Professor Paul F. Linden, Chair

Natural ventilation offers an efficient strategy for concurrently disposing of waste heat and improving indoor air quality within the built environment. Most previous studies of naturally-ventilated buildings assume a one-chamber geometry. Here, we relax this assumption and examine by way of theory and experiments the flows that may develop within a multi-chamber domain. A complex internal stratification of buoyancy is typically observed, the details of which depend upon the relative sizes of the adjacent chambers and the size/vertical location of the internal/external openings. In contrast to simple geometries, this stratification is not necessarily eroded by the mechanical action associated with buoyant convection from an isolated internal thermal source. Consequently, the properties of the eventual steady state cannot be determined without investigating the system's transient evolution.

Hybrid buildings combine passive summer-time cooling by natural ventilation with active winter-time heating by conventional HVAC systems. A further objective is to explore the inherent challenges associated with this dual design, with particular reference to the hysteretic behavior that may occur when forcing

comes from two or more sources, for example internal heat gains and an external wind shear.

This thesis also presents a separate investigation of intrusive gravity currents or intrusions, which are associated with density-driven flow along a sharp interface. Theoretical descriptions often stress the similarity between intrusive gravity currents and those that propagate along a solid boundary. Though helpful in certain special cases, this association is inappropriate whenever the intrusion density differs from the depth-weighted mean density of the upper and lower layers, when interfacial waves must be excited. We present herein a more detailed analysis that properly accounts for this upstream influence using two-layer shallow water theory. Model results show good agreement with analogue experimental and numerical data.

Finally, we consider intrusions where the initial depth of intermediate density fluid is strictly less than the channel depth such that momentum and energy may be exchanged between the forward- and backward-propagating disturbances. When the upstream interface remains approximately flat, the intrusion speed is accurately predicted using a globally-conservative model.

1

Thesis outline and scope

Whereas most theses consider a handful of closely related topics, I have had the good fortune of pursuing parallel research projects during my time at the Univ. of California – San Diego. The present document reflects this dichotomy and presents detailed investigations of both natural ventilation and intrusive gravity currents. To be sure, certain similarities exist between these disparate branches of applied fluid mechanics, not the least of which is that both consider density-stratified, Boussinesq flow. Moreover, as we are reminded every time we open our front door on a cold winter's day, gravity currents are a ubiquitous example of the flows that may occur within real buildings. Nonetheless, most previous studies of gravity currents (be they boundary or intrusive flows) examine their role in environmental, rather than residential transport. This emphasis is preserved in the present discussion. Although a study that explores the impact of gravity currents on ventilated buildings is no doubt worthwhile, this shall not be the focus here.

The thesis is therefore divided into two parts with Chapters 2 through 5 examining natural ventilation and Chapters 6, 7 and 8 examining intrusive gravity currents in two-layer stratified media. In each case, the first chapter of the set provides an introduction to the major research topic. However, in the spirit of the "freestanding chapter" option, the discussion of Chapters 2 and 6 is relatively brief

as each remaining chapter also includes a self-contained introduction.

Chapter 3 explores hysteresis and its connection to building ventilation with particular reference to the thermal source and external wind gradient that provide the impetus for flow. This discussion is of particular relevance in the context of winter-time design of hybrid buildings and rigorously identifies conditions whereby multiple steady ventilation states may be avoided. However, a possible limitation of this analysis is that, as with the related studies of Linden, Lane-Serff & Smeed [55], Woods, Caulfield & Phillips [97], Kaye & Hunt [45], Heiselberg *et al.* [36] and many others, a relatively simple building geometry is considered. Thus, in Chapters 4 and 5 I identify some of the complications and non-intuitive flow behaviors that may arise in the ventilation of a more realistic, i.e. multi-chamber domain.

Chapter 7 investigates intrusive gravity currents (a.k.a. intrusions) as generated by a full-depth lock release. Further to the analyses of Sutherland, Kyba & Flynn [88] and Cheong, Kuenen & Linden [20], I demonstrate that a leading interfacial wave must be excited in front of the forward-propagating disturbance unless the intrusion density equals the depth-weighted mean density of the upper and lower layers. An analytical model is developed, which predicts the intrusion speed by combining shallow water theory with the classical, yet incomplete, description of intrusive gravity currents provided by Holyer & Huppert [37]. In this fashion, a substantial improvement to the existing theoretical exposition is made. Chapter 8 considers a somewhat more general circumstance where the intrusion does not initially span the entire channel depth. Thus the forward- and backward-propagating disturbances may under certain circumstances exchange momentum and energy. Following the related work of Shin, Dalziel & Linden [81], a theoretical model is derived that incorporates this front-to-back communication. Model equations, which apply to a particular, yet important limiting case, are shown to produce robust output that compares favorably with experimental and numerical data.

Table 1.1: Scientific contribution arising from the present thesis.

Chapter	Journal/Conference proceeding	Status	Co-author(s)
3	*Building Environ.*	Submitted	C. P. Caulfield
4	*J. Fluid Mech.*	Published	C. P. Caulfield
5	*Proc.* 6^{th} *ISSF*	To appear	C. P. Caulfield
7	*J. Fluid Mech.*	In press	P. F. Linden
8	*Phys. Fluids*	Submitted	P. F. Linden, T. Boubarne

Key conclusions arising from the present analyses are briefly reiterated in Chapter 9. Moreover, certain detailed calculations and discussions are included in the appendices. In particular, Appendix A presents a derivation of the filling-box equations following the studies of Baines & Turner [5], Manins [62] and Worster & Huppert [98]. These equations are used extensively in the design/analysis of naturally-ventilated buildings. Appendix B summarizes some of the challenges associated with natural ventilation in the context of fire safety. Appendix C provides a detailed derivation of a representative result from Chapter 5, which examines multi-chamber ventilation by a non-ideal thermal source, i.e. one that supplies both heat *and* mass to the interior environment. Appendix D considers Riemann invariant solutions to the one- and two-layer shallow water equations. This derivation makes explicit a result from Baines [4] and provides a helpful background for understanding the behavior of shallow water flows. Finally, Appendix E discusses the open-source DNS algorithm that is applied in studying intrusive gravity currents generated from a partial-depth lock release. As noted above, this numerical code is used to verify the accuracy of a complementary analytical model.

Many components of the thesis have been submitted or accepted for publication either as journal articles or as an extended abstract in a conference proceedings. Details are provided in the Acknowledgments section (page xi) and, more succinctly, in table 1.1.

But for the insights and helpful suggestions of my supervisors and committee members, all work summarized herein is fundamentally "my own," with one exception. The laboratory experiments described in Chapter 8 were conducted by Thomas Boubarne, who visited UCSD as part of an undergraduate research program from March to Aug. 2006. I supervised Thomas quite closely and was ultimately responsible for the design, if not the execution, of the experimental program. Moreover, I am familiar with the experimental methodology applied by Thomas, it being similar to that employed during my Master's degree at the Univ. of Alberta (see for example Flynn & Sutherland [29] and Sutherland *et al.* [88]). Thomas's experimental data is included here because it offers further support of the analytical model and numerical simulations described in Chapter 8.

2

Natural ventilation – overview

2.1 Buildings and energy consumption

Few in the developed world would question Santamouris' [78] observation that "energy consumption defines the quality of urban life..." Unfortunately, the energy demands of large urban areas pose a significant strain on environmental resources, as the following statistics illustrate. Each year, the world's urban population increases by approximately 60 million residents. However, for each 1% increase of population, urban energy consumption increases by more than 2%. A major culprit in these alarming figures is the energy used by modern buildings, which consume approximately 40% of the world's energy and are responsible for 50% of global anthropogenic CO_2 emissions. In the United States, which is the world's largest producer of CO_2, a significant fraction of the energy expended by buildings is devoted to summer-time cooling by high-consumption HVAC systems. Indeed, it is estimated that $3.5 \times 10^9\,\mathrm{m}^2$ of commercial space are actively cooled by traditional air conditioners at an annual energy cost of approximately 250 TWh. (See Santamouris [78] and the references therein.)

Natural ventilation seeks to reduce this energy demand by achieving adequate cooling through judicious use of freely-available resources such as wind forcing, solar radiation and unavoidable internal heat gains. Innumerable specific

strategies and technologies exist, many of which are novel adaptations of clever pre-industrial designs such as the wind towers or "malqafs" used by the ancient Arabians or the tepees favored the natives of the North American Plains (Ghiaus & Roulet [31], Roulet & Ghiaus [77], http://www.wbdg.org/design/naturalventilation.php). In almost all cases, however, small pressure differences, as may arise from stack effects or wind shadows, are exploited to drive air flow between the internal and external environment and thereby remove excess heat from the interior space. This reduces or even eliminates the need for mechanical blowers and/or heat pumps, which are costly to install, operate and repair.

Naturally-ventilated buildings often exhibit a strong vertical stratification of temperature. In contrast to conventional, yet inefficient HVAC systems, the goal is to cool only that portion of the interior environment that is actively used by building occupants or temperature-sensitive equipment. Strong internal variations of temperature (i.e. density) are favored because *(i)* these give rise to the largest possible exchange flows, and, *(ii)* a building's thermodynamic efficiency is improved as the temperature of the exiting fluid increases. When hot, buoyant air is discharged from the roof of a building, it is simultaneously replaced with cooler ambient air, which is advected into the building near ground level.

Clearly, natural ventilation is a poor cooling strategy in very hot and/or hot and humid climates where even the external climactic conditions are beyond one's threshold for comfort. Nonetheless, the advantages of natural ventilation are several-fold and not restricted simply to building cooling. As noted by Santamouris [78], "natural ventilation is [also an] effective instrument to improve indoor air quality in urban areas..."

2.2 Indoor air quality

Estimates provided by the United Nations Centre for Human Settlements suggest that 30% of the world's buildings are inadequately ventilated such that the

indoor air is of substandard quality (Santamouris [78]). In part, this statistic is a reflection of external pollution, for example due to automobile or industrial exhaust. It must be emphasized, however, that the built environment introduces its own surfeit of noxious chemicals. In the developed world, these include formaldehyde and vinyl chloride, which are minor constituents of many common building materials (http://www.npr.org/templates/story/story.php?storyId=3851857). In developing countries, indoor pollution is more often associated with other sources. Smith [84] observes that "about half the population of the world continues to rely for cooking and associated space heating on simple household stoves using unprocessed solid fuels [most often wood] that have high emission factors for a range of health-damaging air pollutants." As a result, each year there are approximately 2 million fatalities worldwide due to the adverse health effects associated with indoor cooking fires (Santamouris [78]).

Consequently enhanced ventilation through natural processes may also serve an important health benefit, particularly for those without reliable access to electricity or other power sources. As noted by Santamouris [78], "the efficient and cheap design of components to enhance ventilation in [under-developed] settlements is a very simple task, involving low or negligible cost."

Notwithstanding this inherent simplicity, however, it must be reiterated that the *external* resources that provide the impetus for fluid flow may be difficult to regulate and therefore some care must be exercised in the design of naturally-ventilated structures. Exacerbating this complication is the challenge of parameterizing turbulent flow in confined geometries. Proper implementation therefore requires a multifaceted approach that draws insights from complementary theoretical, numerical and experimental studies. A concise review of the advantages and limitations of each of these modes of analysis is provided in the following section.

2.3 Modeling naturally-ventilated buildings

Theoretical descriptions of natural ventilation using various degrees of simplification have been developed by numerous researchers (see Linden [53] and the references therein). Quite often, simple geometries are considered with compact internal thermal sources, the convection from which is parameterized using the turbulent plume equations developed by Morton, Taylor & Turner [66]. Typically, conduction and radiation to/from the building's exterior surface are ignored, as is dissipation due to viscous effects. Moreover, insofar as many models simplify mixing dynamics and neglect the transient approach towards steady state, the interior environment is often assumed to consist of a hot upper layer and cool lower layer, which are separated by a sharp interface of infinitesimal thickness. Clearly, this is a somewhat rudimentary approximation to the vertical density profile expected in real buildings where a smooth and gradual variation of temperature is predicted, especially when the thermal forcing is by a number of broadly separated and time varying sources (Liu & Linden [59]).

As described in more detail in § A.5, different considerations apply to distributed thermal sources for which the interior space is typically well-mixed such that spatial gradients of temperature are negligible. Gladstone & Woods [33] show that convective fluid motions may in this case be described through a suitable adaptation of the Rayleigh-Bénard equations. Such a treatment is required, for example, when studying the areal heating supplied by solar radiation through large windows.

Complementary numerical models have also been developed using commercial software such as STAR-CD (http://www.cd-adapco.com) or CFX (http://www-waterloo.ansys.com). The advantage of numerical modeling is that it offers more flexibility in describing (at least qualitatively) the ventilation characteristics of non-simple geometries. Here again, however, certain limiting assumptions must be applied. For numerical models that restrict their attention to flows within

the building's interior, an appropriate boundary condition must be employed to connect the internal and external environments. In addition, Reynolds-averaged Navier Stokes (RANS) algorithms of the type specified above must apply a turbulence closure model to describe sub-grid dissipative effects. Typically, a so-called $k - \epsilon$ model is used, which presumes a particular relationship between the turbulent kinetic energy, k, and its rate of viscous dissipation, ϵ. Although favorable agreement has been observed between the predictions of RANS algorithms and the results of particular ventilation experiments (Linden [53]), commercial codes may also become unstable or produce unreliable output for flows that are very strongly stratified (D. T. Bolster – personal communication, Versteeg & Malalasekera [94]).

In addition, three-dimensional numerical simulations, even those that parameterize sub-grid dissipation and employ a relatively coarse grid, require significant computational resources and therefore remain prohibitively expensive in many cases. As a result, building designers and architects often employ so-called network models, which reduce distinct rooms, office spaces or corridors to discrete nodes that may exchange mass and energy only with their nearest neighbors, and possibly, the external environment. The information provided by such low-order models has proved useful in many instances. However, internal temperature stratifications cannot be accurately accounted for except through certain ad-hoc approaches. Consequently, network models, particularly those without a strong theoretical foundation, may be of limited utility in the context of integrated, low-energy design.

As a way of addressing these deficiencies, complementary physical experiments have also been performed, both at full- and reduced-scale. Although the former provide perhaps the most unadulterated quantitative data, they are difficult and expensive to perform, particularly in view of the large spaces and myriad of measurement equipment/software that may be required. A more attractive alternative, therefore, is to conduct physical experiments in the laboratory using salt and fresh water as the working fluids. These are selected for the purposes of

Table 2.1: Comparison between the dynamically-relevant parameters for building flows and their laboratory analogues. Sources: Kundu [49], Potter & Wiggert [69], http://www.www.d.umn.edu/∼ssternbe.

	Laboratory scale [water]	Building scale [air]
g' [m/s^2]	0.35	0.15
$\hat{H}$ [m]	0.3	3.0
ν [m^2/s]	1.0×10^{-6}	1.5×10^{-5}
D [m^2/s]	2.5×10^{-9}	2.1×10^{-5}
Re	9.7×10^{4}	1.3×10^{5}
Pe	3.9×10^{7}	9.6×10^{4}

achieving a flow that is dynamically-similar to that encountered in real buildings (Simpson [82]). Consider for example, the Reynolds and Peclet numbers, given respectively by

$$\mathrm{Re} = \frac{\hat{u}\,\hat{H}}{\nu}\,, \qquad \mathrm{Pe} = \mathrm{Re}\,\sigma = \frac{\hat{u}\,\hat{H}}{D}\,, \tag{2.1}$$

where ν is the kinematic viscosity, D is the coefficient of molecular or thermal diffusivity, σ is the Schmidt or Prandtl number, $\hat{H}$ is a characteristic vertical length scale and $\hat{u}$ is a characteristic velocity (Linden [53]). The latter quantity is proportional to $(g'\,\hat{H})^{1/2}$ for buoyancy-driven flow where $g' = g\,\Delta\rho/\rho_0$ in which $\Delta\rho$ is a characteristic density difference and ρ_0 is a reference density. Therefore

$$\mathrm{Re} \sim \frac{g'^{1/2}\hat{H}^{3/2}}{\nu}\,, \qquad \mathrm{Pe} \sim \frac{g'^{1/2}\hat{H}^{3/2}}{D}\,. \tag{2.2}$$

Representative values of g', $\hat{H}$, ν, D, Re and Pe for both laboratory-scale and building-scale flows are presented in Table 2.1. It is observed from columns 6 and 7 that the Reynolds and Peclet numbers are large in both cases and thus the flow is dominated by inertial as opposed to molecular effects. By contrast, viscosity would be much more important if the reduced-scale experiments employed air instead of water as the working fluid.

Reduced-scale experiments offer a number of advantages. As described by Linden [53], flows may be easily visualized using food coloring and thus important

transient flow phenomena can be easily identified. In addition, precise quantitative insights may also be discerned with the help of image processing equipment.

A disadvantage of this approach is that conductive and radiative effects to/from solid boundaries cannot be modeled if salt is chosen as the active scalar. Although this particular shortcoming may be partially resolved by employing hot/cold rather than fresh/salty water, this selection limits the range of accessible density differences and introduces other experimental difficulties. Therefore, this method has not been rigorously pursued by experimentalists in the field (C. P. Caulfield – personal communication). Moreover, proper modeling of wind shear effects requires a circulating water channel, which can be both expensive to fabricate and difficult to operate. Finally, laboratory-scale experiments are not suitable for investigating natural ventilation by a combination of temperature and humidity effects.

Clearly, no single methodology for studying natural ventilation is sufficient to provide an exhaustive description of the flow dynamics for a geometry of arbitrary complexity. Thus, although the studies of Chapters 3, 4 and 5 focus primarily upon a theoretical development that relaxes some of the simplifying assumptions of previous analyses, comparisons with experimental data (both our own and that generously provided by Dr. G. R. Hunt) are made where possible and appropriate. In so doing, we hope to elucidate some of the potential difficulties associated with multi-season design of hybrid buildings and also identify some of the key considerations associated with the ventilation of multi-chamber enclosures. Both represent important outstanding problems for the "green architecture" community.

3

Hysteresis effects in natural, blocked and mixed ventilation

3.1 Abstract

The summer-time cooling efficiency of hybrid buildings depends critically upon exploiting multiple environmental resources to dispose of waste heat. To this end, many previous studies have explored the role of wind, which exerts different static pressures on a building's windward and leeward facades. Here, we consider how this methodology may be extended to the converse problem of winter-time heating wherein hot, buoyant air is purposefully supplied to the interior space. Thus a "blocked" flow regime is favored such that cold air infiltration is avoided. In well-defined regions of parameter space, blocked conditions represent a unique solution to the flow equations. Hence, for a given building geometry, the likelihood of blocking may be increased through prudent choice of extraction vent size/orientation depending on the external forcing conditions. A discussion of the inherent tradeoffs associated with multi-season design of hybrid buildings is also presented.

3.2 Introduction

Natural ventilation harnesses freely-available resources such as solar radiation, internal heat gains and wind forcing to drive fluid flows within buildings. It offers an economically-attractive alternative to ventilation by traditional mechanical systems, particularly when two or more resources work in tandem to boost system efficiency. For example during summer months, occupant comfort is maximized by removing the waste heat produced by electrical equipment and other machinery. This is most effectively achieved using a displacement ventilation scheme, which exploits pronounced vertical gradients of temperature in the indoor environment (see *e.g.* figure 1(b) of Linden [53]). By judiciously locating lower and upper openings to the exterior along the building's windward and leeward facades, respectively, the driving force for fluid motion may be enhanced whereby system performance is substantially improved. More specifically, Hunt & Linden [41] examine the ventilation of a single chamber by an isolated thermal source of zero volume flux. Consistent with the above discussion, the depth and temperature of the buoyant layer that collects along the chamber's ceiling decrease as the external forcing becomes more severe.

Unfortunately, the wind direction often exhibits diurnal or seasonal variations. A reversed external flow results in an adverse static pressure gradient that acts against the natural direction of the internal buoyant convection. This effect has been examined for both distributed (Gladstone & Woods [33], Li & Delsante [50], Li *et al.* [51], Lishman & Woods [57]) and isolated (Hunt & Linden [42], Heiselberg *et al.* [36]) thermal sources. With the exception of Gladstone & Woods [33], these analyses assume that the thermal forcing is independent of the internal temperature, T, and hence the effective source temperature, T_s, and reduced gravity, $g'_s = g\,\alpha_e\,(T_s - T_a)$, are singular. (The source is said to be "ideal" in this circumstance.) Here, g is gravitational acceleration, α_e is the fluid's coefficient of thermal expansion and T_a is the temperature of the external ambient. It is observed

that the ventilation flow supports multiple stable states for many combinations of source strength and wind forcing. Hysteretic behavior is therefore observed such that the transition between buoyancy- and wind-dominated flows proceeds along different (often poorly-quantified) quasi-steady paths depending upon the flow's time history.

Because hysteresis effects represent a non-trivial impediment to optimizing building/ventilation design, it is desirable to identify conditions such that multiple steady states cannot occur. Non-trivial bounds to this effect may be derived for an ideal thermal source by including wall conduction effects (Li & Delsante [50]) or by considering an enclosure with three or more openings to the external environment (Lishman & Woods [57]). As we demonstrate herein, the possibility of hysteresis may be similarly curtailed by considering a "non-ideal" source, *i.e.* one that supplies both heat *and* mass to its surroundings. Paradoxically, this analysis is of particular utility in the context of *winter-time* design of hybrid buildings where deliberate heat addition to indoor spaces is required. During winter both the naturally-ventilated and wind-dominated regimes described by Hunt & Linden [42] are undesirable because they involve, respectively, infiltration of cold exterior air at low- and high-level, which is likely to yield uncomfortable internal conditions. Rather a "blocked" ventilation scheme is preferred such that there is outflow through openings at all heights and indoor vertical gradients of temperature are removed. By determining the maximal range over which multiple steady solutions may occur, it is then straightforward to identify the area of parameter space in which this favorable intermediate state must be realized.

3.3 Wind opposes ventilation

3.3.1 Ideal vs. non-ideal sources

The ventilation of a single chamber by an isolated, ideal, floor-level source in the presence of an adverse wind that imposes a static pressure drop Δp between

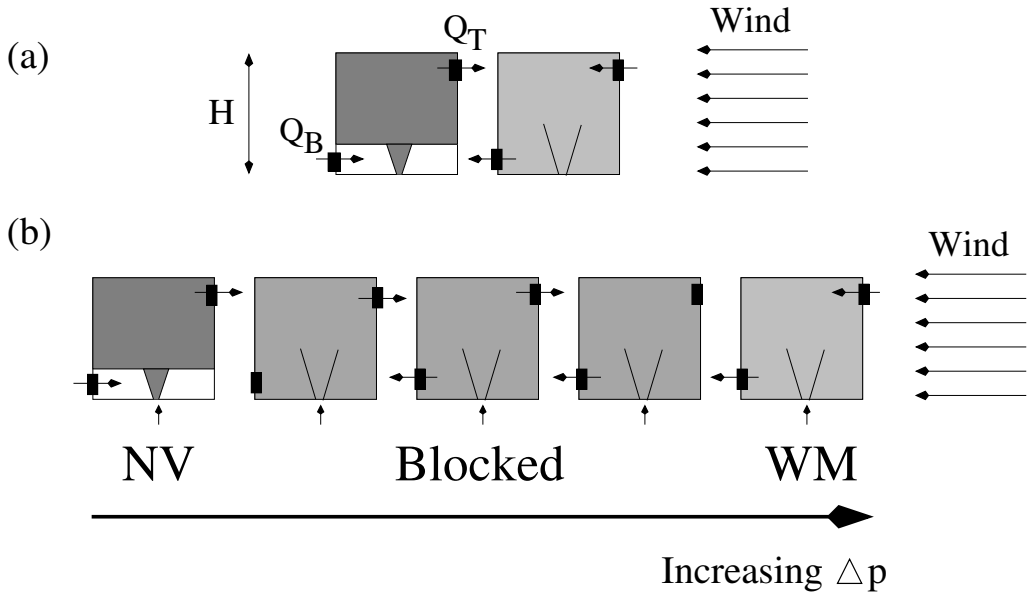

Figure 3.1: Schematic illustration of observable flow regimes in the presence of an adverse wind assuming (a) a zero volume flux source of infinite temperature, and, (b) a finite volume flux source of finite temperature. In the former circumstance, only naturally-ventilated (NV) and well-mixed (WM) states are possible. Conversely, when the source supplies heat *and* mass to its surroundings, blocking may occur in which case there is no inflow of ambient air to the chamber.

upper and lower openings is depicted schematically in figure 3.1a. A buoyancy-dominated, naturally-ventilated regime with inflow of dense ambient fluid through the lower leeward opening (effective cross-sectional area A_B) and outflow of buoyant fluid through the upper windward opening (effective cross-sectional area A_T) is favored only when the magnitude of the thermal forcing exceeds that exerted by the external wind. In this circumstance, the fluid inside the chamber is comprised of two distinct layers that are separated by a sharp interface, as illustrated schematically in figure 3.1a(i). The (dimensional) interface height, $\xi\, H$, can be determined by solving

$$\frac{A_\star}{H^2} = \frac{\lambda^{3/2}\, \xi^{5/3}}{\left(\frac{1-\xi}{\xi^{5/3}} - \frac{\Delta p}{\rho_0} \cdot \frac{\lambda\, H^{2/3}}{B_s^{2/3}} \right)^{1/2}} \tag{3.1}$$

(see (8) of Heiselberg *et al.* [36]). Here B_s is the source buoyancy flux, H is the chamber height, ρ_0 is a characteristic reference density (whose precise value is immaterial if the Boussinesq approximation is applied) and $A_\star$ is the effective area defined by (2.4)b of Linden, Lane-Serff & Smeed [55]

$$A_\star = \frac{2^{1/2} A_T\, A_B}{(A_T^2 + A_B^2)^{1/2}}\,. \tag{3.2}$$

In this ventilated regime, it is assumed that turbulent convection above an isolated source is well-described by turbulent plume theory and the "filling-box" equations of Baines & Turner [5]. Thus λ denotes the universal plume constant

$$\lambda = \frac{6\alpha}{5} \left(\frac{9\alpha}{10} \right)^{1/3} \pi^{2/3} \tag{3.3}$$

based on the assumption that the plume satisfies "top-hat" distributions for the vertical velocity and buoyancy profiles (Turner [90]). Here, $\alpha \simeq 0.1$ is the entrainment constant, which gives the ratio of the lateral entrainment velocity to the mean vertical velocity at any height between the level of the source ($z = 0$) and the level of the interface ($z = \xi\, H$).

Although (3.1) provides an accurate description of dynamical behavior for moderate ξ (see *e.g.* figures 9 through 11 of Hunt & Linden [42]), it also

predicts that $\xi > 0$ for arbitrarily large Δp. Because this situation is clearly unphysical, Hunt & Linden [42] argue that the flow must eventually transition in a discontinuous fashion to a wind-dominated, well-mixed mode in which there is inflow through the windward opening and outflow through the leeward opening (figure 3.1a(ii)). Here, the stable two-layer stratification that characterizes the naturally-ventilated regime is replaced by a uniform layer of relatively buoyant fluid that occupies the chamber's entire vertical extent[1].

Interestingly, the discontinuous adjustment described in the previous paragraph disappears if *(i)* the source is non-ideal with $Q_s > 0$ and $g'_s < \infty$ where Q_s and g'_s denote, respectively, the source volume flux and reduced gravity, and, *(ii)* the following inequality is satisfied

$$\frac{Q_s}{A_B} \geq (g'_s\, H)^{1/2} \tag{3.4}$$

in which $(g'_s\, H)^{1/2}$ denotes a characteristic velocity associated with the thermal forcing. If *(i)* and *(ii)* are satisfied, the following sequence is expected as the wind forcing is augmented in incremental steps starting with a small external wind velocity. Initially, a naturally-ventilated state is anticipated with $0 < \xi < H$, $Q_T > Q_s > 0$ and $Q_B < 0$ (figure 3.1b(i) – state NV). As the wind forcing is increased, however, the interface must slowly descend toward the level of the source, *i.e.* the buoyant layer becomes thicker. A critical condition is achieved once this layer exactly fills the chamber such that $\xi = 0$ at which point flow through the lower opening is arrested (*i.e.* $Q_B = 0$) and hence by mass balance $Q_T = Q_s$ (figure 3.1b(ii)). For any Δp larger than this critical value, $0 < (Q_T,\, Q_B) < Q_s$ and this state is maintained until the chamber's internal stack pressure is insufficient to drive a flow through the upper opening (Gladstone & Woods [33]). At this point the wind forcing will have exactly impeded the buoyancy-driven flow and hence $Q_T = 0$ while $Q_B = Q_s$ (figure 3.1b(iv)). Finally, for any further increase of Δp,

[1]Similar discontinuities are observed in the studies of Li & Delsante [50] and Li *et al.* [51] although in these analyses temperature is well-mixed over the chamber height in both the buoyancy- and wind-dominated regimes. Indeed, it is shown by Heiselberg *et al.* [36] that the details of the buoyancy stratification do not impact the quasi-steady transition between disparate states.

Q_T must become negative and the chamber can only support a well-mixed flow of the type described previously (figure 3.1b(v) – state WM)[2].

Moreover, with $Q_s/A_B \geq (g'_s\, H)^{1/2}$, the variation described above is continuous in the reverse direction as well. Thus if Δp is subsequently decreased, each of the five flow regimes illustrated in figure 3.1b are revisited. By contrast, qualitatively different behavior is observed when $Q_s > 0$ but $Q_s/A_B < (g'_s\, H)^{1/2}$ in which case the system cannot transition to/from the well-mixed mode in a continuous fashion. Indeed, discontinuities may be of such severity that the blocked regime is avoided altogether during the reverse transition towards the naturally-ventilated state.

3.3.2 Non-ideal sources - Theory

The relative importance of wind *vs.* internal buoyancy may be quantified by considering the characteristic volume flux associated with each type of forcing. These are given, respectively, by

$$Q_w = A_\star \left(\frac{\Delta p}{\rho_0}\right)^{1/2}, \qquad Q_v = A_\star^{2/3}\, B_s^{1/3}\, H^{1/3}\,. \tag{3.5}$$

Consistent with (2.8) of Hunt & Linden [42], a non-dimensional wind forcing or Froude number, F, is defined as the ratio of these fluxes, *i.e.*

$$\mathrm{F} \equiv \frac{Q_w}{Q_v} = \left(\frac{\Delta p}{\rho_0}\right)^{1/2} \left(\frac{A_\star}{B_s\, H}\right)^{1/3}. \tag{3.6}$$

Similarly, the non-dimensional source volume flux is given by $q_s = Q_s/Q_v$. It provides a measure of the deviation from the ideal source condition considered by Hunt & Linden [42]. A small departure is expected during summer months when Q_s is small (or identically zero) whereas adjustable openings such as windows have a broad cross-sectional area, which facilitates communication between the interior and exterior environments. Conversely, during winter months, a notable deviation

[2]It is assumed throughout that the driving force for fluid expulsion through the upper opening comes strictly from the internal stack pressure, *i.e.* we neglect the motive force provided by auxiliary fans or blowers, which are found on the roofs of many commercial buildings. This assumption is considered in further detail in § 3.5.

Table 3.1: Characteristic polynomial equations for q_T in the naturally-ventilated, blocked and well-mixed regimes. Equations are derived using the procedure outlined in §§ 2.1 and 2.2 of Hunt & Linden [42]. Here ξ is the non-dimensional interface height, which becomes vanishingly small as $q_T \to q_s$.

Regime	Characteristic polynomial
Naturally-ventilated, $q_T > q_s$ **(eqn. 1)**	$0 = q_T^3 - 2(1-a^2)\,q_s\,q_T^2 + q_T\,[(1-a^2)q_s^2 + \mathrm{F}^2] - 1 + \xi$
Blocked, $0 \le q_T \le q_s$ **(eqn. 2)**	$0 = (1-2a^2)\,q_s\,q_T^2 - 2(1-a^2)q_s^2\,q_T + (1-a^2)\,q_s^3$ $-q_s\,\mathrm{F}^2 + 1$
Well-mixed, $q_T < 0$ **(eqn. 3)**	$0 = q_T^3 - (3-2a^2)\,q_s\,q_T^2 + [3(1-a^2)\,q_s^2 - \mathrm{F}^2]\,q_T$ $-(1-a^2)\,q_s^3 + q_s\,\mathrm{F}^2 - 1$

from ideal source behavior is anticipated because heat is purposefully added to the space *e.g.* through a forced air system. Also, windows are typically closed so that $A_\star$ is small[3]. Hence, q_s is appreciably larger than zero. In the following analysis, system performance is considered in both limiting cases $q_s \simeq 0$ and $q_s \not\simeq 0$.

Associated with the naturally-ventilated, blocked and well-mixed flow regimes of figure 3.1b are unique polynomial equations that relate the non dimensional volume flow rate through the upper opening, $q_T = Q_T/Q_v$, to F, q_s and the geometric parameter

$$a^2 = \frac{A_\star^2}{2A_T^2} = \frac{A_B^2}{A_T^2 + A_B^2} \tag{3.7}$$

(see table 3.1). Naturally-ventilated conditions are possible provided the wind forcing is sufficiently weak to allow a volumetric flow of $q_T > q_s$ through the upper opening. The critical condition illustrated in figure 3.1b(ii) is achieved when

[3]Clearly $A_\star \not\to 0$ because of deliberate and non-deliberate communication with the exterior. This is achieved, respectively, via extraction vents and imperfect seals around window and door frames.

Table 3.2: Characteristic range of F^2 associated with the flow regimes of figure 3.1b. Column 3 indicates whether the criteria of Column 2 are necessary or sufficient to achieve the corresponding flow state.

Regime	Range of F^2	Necessary/sufficient
Naturally-ventilated	$F^2 < \frac{1-a^2\,q_s^3}{q_s} \equiv F^2_{NV}$	Necessary, not sufficient
Blocked	$F^2_{NV} \equiv \frac{1-a^2\,q_s^3}{q_s} \leq F^2 \leq \frac{1+(1-a^2)\,q_s^3}{q_s} \equiv F^2_{BL}$	Necessary, not sufficient
Well-mixed	$F^2 > \frac{1+(1-a^2)\,q_s^3}{q_s} \equiv F^2_{BL}$	Sufficient, not necessary

$q_T = q_s$ whereupon

$$F^2 = \frac{1 - a^2\,q_s^3}{q_s} \equiv F^2_{NV} \tag{3.8}$$

(see equations 1 and 2 of table 3.1). Therefore a ventilated state is anticipated only if $F < F_{NV}$ and hence $q_T > q_s$. Note that $F^2_{NV} \to \infty$ as $q_s \to 0$, and so naturally-ventilated behavior is always at least theoretically possible for $q_s = 0$, as predicted previously. By contrast, the flow will be blocked if $0 \leq q_T \leq q_s$ in which case there is no infiltration of outside air through either opening. The critical condition illustrated in figure 3.1b(iv) is realized when $q_T = 0$. In this circumstance, equations 2 and 3 of table 3.1 show that

$$F^2 = \frac{1 + (1 - a^2)\,q_s^3}{q_s} \equiv F^2_{BL}\,. \tag{3.9}$$

Thus blocked conditions are possible only for intermediate wind speeds corresponding to $F_{NV} \leq F \leq F_{BL}$, and so blocking cannot occur as $q_s \to 0$. (Consistent with this interpretation, we show in § 3.5 that $F_{NV} < F_{BL}$ over the admissible range of q_s and a^2.) Conversely, when $F > F_{BL}$, only well-mixed conditions with $q_T < 0$ are possible. However, very importantly, equation 3 of table 3.1 also admits physical roots (*i.e.* with $q_T < 0$) for $F < F_{BL}$ and even $F < F_{NV}$ and thus well-mixed con-

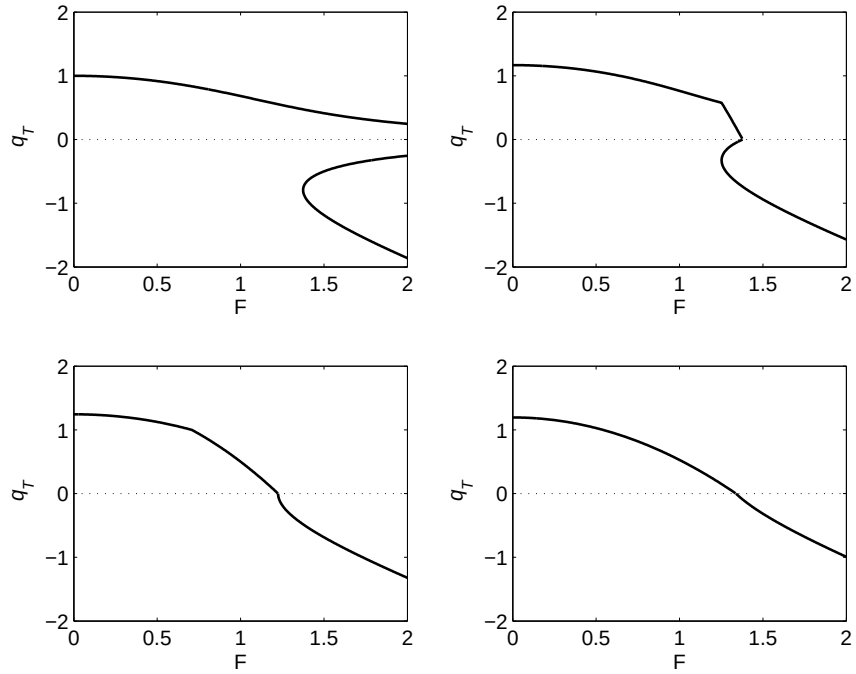

Figure 3.2: Non-dimensional flow rate, q_T, as a function of F for $a^2 = \frac{1}{2}$ and (a) $q_s = 0$, (b) $q_s = 0.5765$, (c) $q_s = 1$, and (d) $q_s = 1.5$. Panel (c) shows the critical case $q_s^3 = \frac{1}{2}(1 - a^2)^{-1}$ for which multiple steady states are exactly avoided.

ditions may be observed for $\mathrm{F} < \mathrm{F}_{BL}$ and/or $\mathrm{F} < \mathrm{F}_{NV}$. (This is the non-zero q_s generalization of the observations of Hunt & Linden [42].) Therefore, the critical conditions quantified by (3.8) and (3.9) must be interpreted with care. Specifically, as summarized by table 3.2, they provide necessary, though not sufficient, conditions describing the existence of the naturally-ventilated and blocked regimes. Refining the above analysis by deriving more concrete existence/uniqueness bounds for the distinct flow regimes is a central objective of the present study.

For illustrative purposes, solutions to the polynomial equations of table 3.1 for $a^2 = \frac{1}{2}$ are shown in figure 3.2 for a variety of q_s. Although, a well-mixed mode with $q_T < 0$ does not appear until F has surpassed a minimum threshold, in general, two well-mixed solutions of the correct sign (*i.e.* with $q_T < 0$) are predicted thereafter (figures 3.2a,b). As described by Li & Delsante [50], Hunt & Linden [42]

and Lishman & Woods [57], however, only the lower branch of the curve is stable: along the upper branch $|q_T|$ is predicted to decrease as Δp increases, which is physically unreasonable. Therefore, whereas each individual flow regime admits at most one stable solution, multiple stable states are nonetheless possible wherever the composite curves of figure 3.2 become multi-valued in F, corresponding mathematically to the well-mixed polynomial equation having three real (one positive, two negative) roots. As illustrated schematically in figure 3.3, hysteresis is associated with an asymmetric transition (resulting from quasi-steady variations to Δp and g_s') to/from the well-mixed mode.

As noted above, for an ideal source with $q_s = 0$, F_{NV}, $\mathrm{F}_{BL} \to \infty$ and the curves corresponding to the naturally-ventilated and well-mixed flow regimes never intersect (figure 3.2a). As a result, the location of the forward transition point $\mathrm{F} = \mathrm{F}_{BL}$ is necessarily ill-defined (Hunt & Linden [42]). For $q_s > 0$, however, (3.8) and (3.9) show that $\mathrm{F}_{NV} < \mathrm{F}_{BL} < \infty$. By virtue of the blocked intermediate state, which connects the naturally-ventilated and well-mixed flow regimes, the forward transition point is now well-defined.

Regardless of q_s, the reverse transition point is also well-defined. As suggested by figure 3.3, however, its location is dictated by the bifurcation point that separates the stable and unstable branches of the well-mixed curve. Clearly, this bifurcation point occurs when equation 3 of table 3.1 has a double non-positive real root. With reference to this equation, we note that the coefficient of the linear term changes sign once

$$\mathrm{F}^2 = 3(1-a^2)\, q_s^2 \equiv \mathrm{F}_\star^2\,, \tag{3.10}$$

and so $\mathrm{F}^2 > \mathrm{F}_\star^2$ is a necessary (though not sufficient) condition for there to exist well-mixed solutions simultaneously with either blocked or naturally-ventilated solutions. Equating (3.9) and (3.10) shows that no bifurcation point can appear in the lower half-plane when $q_s^3 \geq \frac{1}{2}\,(1-a^2)^{-1}$ in which case there exists a smooth and continuous transition between the blocked and well-mixed regimes through the point $q_T = 0$ (see (3.4)). By contrast when $q_s^3 < \frac{1}{2}\,(1-a^2)^{-1}$, both stable

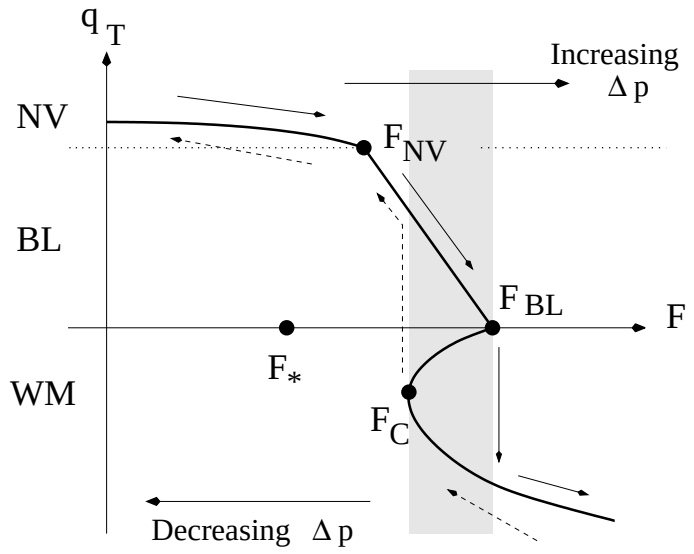

Figure 3.3: Flow regime transition in the (F, q_T) plane. With $q_s^3 < \frac{1}{2}(1-a^2)^{-1}$, multiple steady states will occur for $\mathrm{F}_C \leq \mathrm{F} \leq \mathrm{F}_{BL}$, *i.e.* in the shaded region. The forward and backward transitions are indicated, respectively, by the solid and dashed arrows. Flow regimes are as indicated where NV, BL and WM stand for naturally-ventilated, blocked and well-mixed, respectively.

and unstable branches to the well-mixed polynomial appear. (Notice once again that the limiting case $q_s \to 0$ implies the possibility of multiple solutions for all a^2.) Figure 3.2c considers the limiting case $q_s^3 = \frac{1}{2}(1-a^2)^{-1}$ whereupon the bifurcation point falls exactly on the line $q_T = 0$. Conversely figure 3.2b considers the limiting case $q_s = 0.5765$ whereby the reverse transition exactly bypasses the blocked regime. Thus the system displays a pronounced asymmetry: as Δp is progressively increased from zero, well-mixed conditions may only be achieved through an intermediate blocked state. As Δp is subsequently decreased, however, the well-mixed mode transitions directly to the naturally-ventilated regime and thus blocked conditions are never encountered. In addition, as figure 3.2b makes especially clear, even with $q_s^3 < \frac{1}{2}(1-a^2)^{-1}$, multiple steady states can occur only for certain choices of F, here corresponding to the range $\mathrm{F}_C = 1.252 \leq \mathrm{F} \leq 1.379 = \mathrm{F}_{BL}$. In the present context, the critical lower bound, $\mathrm{F}_C\,(\geq \mathrm{F}_\star, \leq \mathrm{F}_{BL})$, represents the minimum Froude number at which multiple steady states may appear for fixed

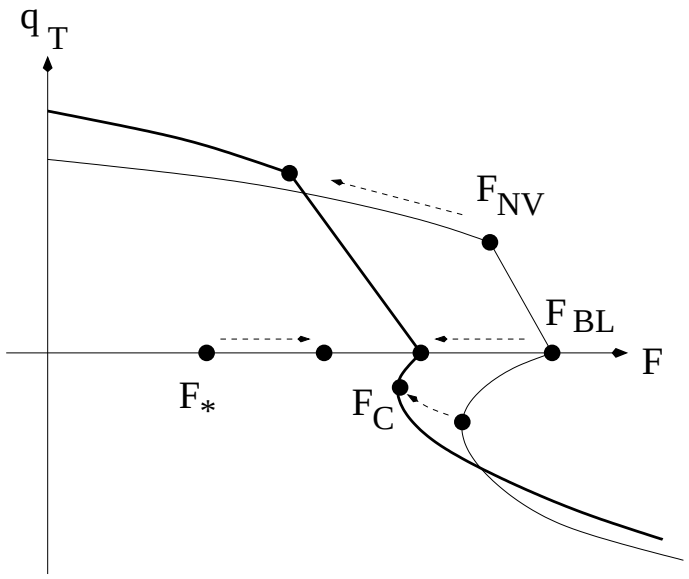

Figure 3.4: Variation of the critical points F_{NV}, F_{BL} and F_C as q_s is increased. For completeness, we also indicate the variation of $\mathrm{F}_\star$.

a^2 and $q_s < \left[\frac{1}{2}(1-a^2)^{-1}\right]^{1/3}$. In contrast to F_{NV} and F_{BL}, F_C can only be determined numerically, except for the special case $q_s^3 = \frac{1}{2}(1-a^2)^{-1}$ whereby $\mathrm{F}_C = \mathrm{F}_\star = \mathrm{F}_{BL}$ and hence F_C is given by (3.9) or equivalently (3.10) – see figure 3.2c. Furthermore, when $q_s^3 < \frac{1}{2}(1-a^2)^{-1}$, it is the magnitude of F_C relative to F_{NV} and F_{BL} that determines the qualitative nature of the hysteresis as well as the breadth of wind forcing over which multiple steady states may occur. Further to figures 3.2 and 3.3, this is illustrated schematically in figure 3.4, which shows how F_{NV}, F_{BL} and F_C change with q_s for fixed a^2.

A corresponding quantitative analysis is summarized by figure 3.5, which delineates the system's hysteretic behavior for arbitrary a^2 and q_s. The solid curve, which passes through $(a^2, q_s) = (\frac{1}{2}, 1)$, shows the locus of points satisfying $\mathrm{F}_C = \mathrm{F}_\star = \mathrm{F}_{BL}$ wherein $q_s^3 = \frac{1}{2}(1-a^2)^{-1}$. By contrast, the dashed curve, which passes through $(\frac{1}{2}, 0.5765)$, shows the locus of points satisfying $\mathrm{F}_C = \mathrm{F}_{NV}$. Consistent with the above discussion, hysteresis is not predicted if $q_s^3 \geq \frac{1}{2}(1-a^2)^{-1}$ in which case F_C is not defined because no bifurcation point appears for $q_T < 0$ and there is an exact forward-backward symmetry of the type suggested

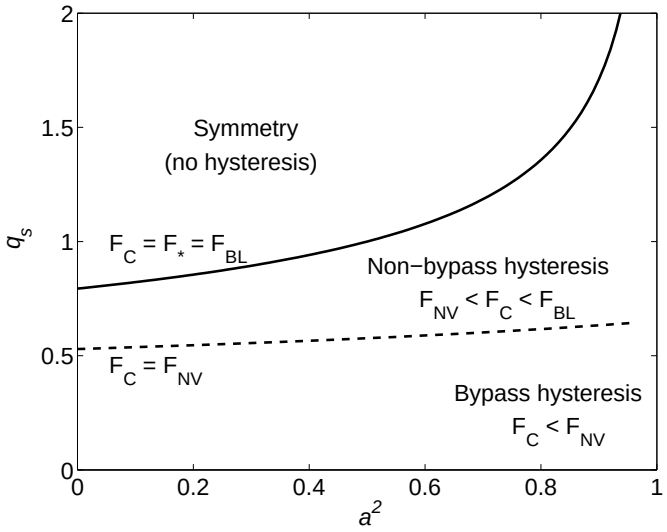

Figure 3.5: Hysteresis regime diagram.

by figure 3.2d. Conversely, between the solid and dashed curves, hysteresis is observed, however a blocked regime separates the naturally-ventilated and well-mixed modes in both directions. Finally, below the dashed curve, blocking is encountered only during the forward transition towards well-mixed conditions; the blocked regime is bypassed during the reverse transition from the well-mixed to the naturally-ventilated state. The disparate regimes identified in figure 3.5 stand in stark contrast to the study Hunt & Linden [42] for which *(i)* the intermediate blocked regime is always inaccessible, and, *(ii)* hysteresis effects are anticipated for all combinations of physical parameters. Thus, only one of the three regimes is achieved.

Regardless of a^2, figure 3.5 suggests that bypass hysteresis will occur for $q_s \lesssim 0.53$. Indeed as $q_s \to 0$, $(\mathrm{F}_{BL} - \mathrm{F}_C)$ increases and thus the range of F over which there exist multiple steady solutions grows significantly. Moreover, for small q_s, $\mathrm{F}_{BL}^2 \simeq q_s^{-1}$ and hence the forward transition to the well-mixed mode is expected once

$$\mathrm{F}^2 \gtrsim q_s^{-1} \,. \tag{3.11}$$

Consistent with the study of Gladstone & Woods [33], therefore, naturally-ventilated

Table 3.3: Flow behaviors for various q_s. Abbreviations are as given in figure 3.3 with MSS indicating multiple steady states.

Source volume flux	Permissible flow regimes	MSS/hysteresis possible?	Description
$q_s \gg 0$	BL, WM	No	$\mathrm{F}_{NV} \leq 0$
$q_s > 0$	NV, BL, WM	No	Symmetry
$q_s \gtrsim 0$	NV, BL, WM	Yes	Non-bypass
$q_s \gtrsim 0$	NV, BL, WM	Yes	Bypass
$q_s = 0$	NV, WM	Yes	$\mathrm{F}_{NV}, \mathrm{F}_{BL} \to \infty$

and blocked solutions are impossible once $(\Delta p/\rho_0)^{1/2} > (g'_s H)^{1/2}$. Here $(\Delta p/\rho_0)^{1/2}$ denotes a characteristic vertical velocity *inside* the chamber associated with the *external* static pressure drop exerted by the wind. When $(\Delta p/\rho_0)^{1/2} = (g'_s H)^{1/2}$ the opposing influences of wind and buoyancy are exactly balanced *i.e.* there is outflow through both openings with $Q_T = Q_B$. At this unique point, the system neither approaches nor recedes from the buoyancy- or wind-dominated regimes as the opening areas are adjusted. Because $g'_s = B_s/Q_s$ is not well-defined as $Q_s \to 0$, no comparable equilibrium point can be identified in the equivalent zero source volume flux problem. Indeed $Q_T = Q_B$ does not represent a steady solution to the constant flux model equations considered by Hunt & Linden [42] because $Q_T = Q_B$ implies $Q_T = Q_B = 0$ such that buoyancy accumulates inside the chamber *ad-infinitum* (Lishman & Woods [57]).

From the preceding discussion we may identify five distinct categories of flow behaviors (see table 3.3). We demonstrate in § 3.5 how this classification may be fruitfully applied to multi-season design.

3.3.3 Comparison with experiments - Reverse transition

In the case of an ideal source, (discontinuous) transition from the well-mixed to the naturally-ventilated mode is expected once $\mathrm{F} < 3^{1/2}/2^{1/3}$. For the

most part, favorable agreement has been observed when comparing this result against experimental data (see *e.g.* figure 8 of Li *et al.* [51] and figures 13 and 14 of Hunt & Linden [42]). By necessity, however, experiments are performed using a small but non-zero source volume flux, Q_s. Therefore, where sufficient description of the experimental apparatus and procedure is provided, a meaningful comparison can be drawn between existing laboratory data and the predictions of the present model. Here focus is restricted to the data generously provided by Dr. G. R. Hunt (personal communication) in which there is relatively easy communication between the internal and external spaces. Specific details of the equipment design are summarized in Hunt & Linden [42].

Table 3.4 compares the critical values of F at which the reverse transition from the well-mixed to the naturally-ventilated mode occurs. Consistent with previous analyses, the agreement between theory and experiment is reasonable, especially considering the non-trivial challenges associated with collecting robust physical data.

3.3.4 Comparison with experiments - Forward transition

Because F_{NV}, $\mathrm{F}_{BL} \to \infty$ as $q_s \to 0$, the ideal source model equations cannot predict the critical Froude number, $\mathrm{F}_{forward}$, corresponding to the forward transition to the well-mixed regime. However, Hunt & Linden [42] conclude from experimental measurements that $\mathrm{F}_{forward} \simeq 1.6-1.7$ whereas Heiselberg *et al.* [36] argue that $\mathrm{F}_{forward} \simeq 1.7-2.4$ based on a combination of experimental and numerical investigations. Moreover, figure 14 of the former study suggests that $\mathrm{F}_{forward}$ is independent of the opening area. With $q_s \simeq 0$, however, this last observation contradicts (3.11), which predicts that $\mathrm{F}_{forward} \propto A_\star^{1/3}$. This apparent discrepancy is most likely due to the unstable character of the naturally-ventilated mode as $\xi \to 0$. In this limit, Heiselberg *et al.* [36] note that "the [naturally-ventilated] flow becomes very sensitive to any perturbations and the flow is [readily] switched to the [well-mixed] state." (Complementary mathematical arguments are summarized in

Table 3.4: Comparison between measured and predicted values of F at which the flow reverts from wind- to buoyancy-dominated.

q_s	$\mathrm{F}_{expt.}$	$\mathrm{F}_{theo.}$
0.0152	1.36 to 1.43	1.3704
0.0176	1.41 to 1.51	1.3697
0.0215	1.31 to 1.37	1.3686
0.0280	1.50 to 1.59	1.3667
0.0446	1.49 to 1.54	1.3621

§ 4 of their study.) In other words, unless changes to Δp are made excruciatingly slowly (a particular difficulty in the context of physical experiments), well-mixed conditions may be realized before $\mathrm{F}^2 \simeq q_s^{-1}$. These factors appear to be at play in figure 12c of Hunt & Linden [42] in which case the interface is heavily deformed such that there is outflow (inflow) through the lower (upper) opening and yet $\bar{\xi} > 0$. Here, $\bar{\xi}$ denotes the horizontally-averaged non-dimensional interface height.

Assuming Δp varies in a quasi-steady fashion inevitably leads to the most conservative estimate of the forward transition point. Nonetheless, the model equations of §§ 3.3.2 are helpful because they provide a hard upper bound in describing regions where multiple steady states may occur. This idea is further explored in § 3.5.

3.4 Wind assists ventilation

In contrast to the discussion of § 3.3, analytical complications are by and large avoided when the wind and buoyancy forcing reinforce one another so that $\Delta p < 0$ and therefore by (3.6) $\mathrm{F}^2 < 0$. This situation is realized when the lower and upper openings are located, respectively, along the chamber's windward and leeward facades. In this circumstance, the well-mixed ventilation mode depicted in figure 3.1 with inflow through the upper opening is clearly impossible: only

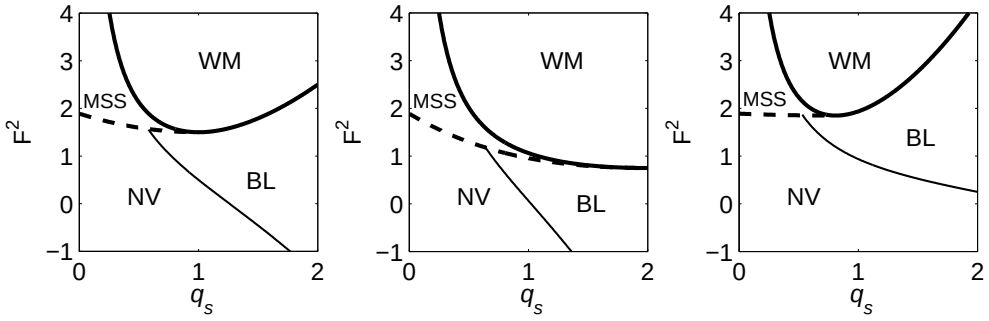

Figure 3.6: Ventilation flow regimes as functions of F^2 and q_s assuming (a) $a^2 = \frac{1}{2}$, (b) $a^2 = \frac{15}{16}$, and (c) $a^2 = \frac{1}{16}$. Abbreviations are as given in figure 3.3 and table 3.3. The thick solid line shows the curve $\mathrm{F}^2 = \mathrm{F}^2_{BL}$ – see (3.9). Conversely, the thin solid line shows the curve $\mathrm{F}^2 = \mathrm{F}^2_{NV}$ over the range where multiple steady states are impossible – see (3.8).

naturally-ventilated and blocked conditions are physically obtainable. Consistent with the previous discussion, the boundary between these disparate states is easily identified as

$$\mathrm{F}^2 = \mathrm{F}^2_{NV} \,. \tag{3.12}$$

As with the analysis of Woods, Caulfield & Phillips [97], (3.12) predicts $a^2\, q_s^3 = 1$ as the critical (non-dimensional) condition for blocking in the absence of an imposed wind.

3.5 Discussion

The preceding analysis provides a complete picture of the disparate flow regimes that are possible when ventilating a single chamber in the presence of either an adverse or favorable wind. In particular for prescribed F, a^2 and $q_s > 0$ it is possible to identify categorically regions where multiple steady states cannot be realized, *i.e.* the flow regime is unique.

During summer months, focus is placed upon waste heat removal. Be-

cause this is greatly facilitated by enhancing communication between the interior and exterior spaces, we assume $q_s \simeq 0$ and thus source conditions are of secondary importance. In addition, Linden *et al.* [55] suggest that q_T is principally determined by the smaller of A_T and A_B and therefore system performance is optimized (*i.e.* q_T is maximized) by selecting $A_T \simeq A_B$. A regime diagram illustrating the various ventilation modes appropriate to this geometrical configuration is depicted in figure 3.6a. The thick and thin solid curves correspond, respectively, to $\mathrm{F}^2 = \mathrm{F}^2_{BL}$ and $\mathrm{F}^2 = \mathrm{F}^2_{NV}$. The latter curve is shown only where the flow regime is unique and thus does not extend into the region labeled "MSS." Hence if the wind forcing opposes ventilation (*i.e.* $\mathrm{F}^2 > 0$), naturally-ventilated conditions are assured only below the dashed curve. Therefore, for any increase of F^2, q_s must be decreased by opening more windows to the exterior. Although this will further increase F^2, the above strategy will nonetheless increase the level of the interface and thereby increase and decrease, respectively, the overall flow rate through the system and the average interior temperature.

Conversely, during winter months, heat addition/retention is of critical importance so that extraction vents represent the only deliberate openings to the exterior. Thus, a blocked flow regime is favored in which the internal pressure exceeds the external pressure at all heights. Moreover, because (3.12) depends on A_T, but not A_B, a transition from naturally-ventilated to blocked conditions is greatly facilitated by choosing $A_T \simeq 0$, *i.e.* $a^2 \simeq 1$. With A_T small and supposing $\mathrm{F}^2 > 0$, however, it is in turn easier to transition from blocked to well-mixed conditions. By contrast if $a^2 \simeq 0$, blocking is observed over a wider (narrower) range of opposing (assisting) wind forcings. These trends are illustrated in figures 3.6b,c which show regime diagrams of the ventilation modes assuming $a^2 = \frac{15}{16}$ and $a^2 = \frac{1}{16}$, respectively.

Figure 3.6 suggests a variety of alternatives with respect to optimizing cold weather design. If the wind is predominantly unidirectional (or extraction vents may be installed on multiple building faces and opened/closed as needed),

there is a clear advantage in concentrating extraction vents at ceiling-level along the building's windward facade (*i.e.* $a^2 \simeq 0$; figure 3.6c). By contrast, if the wind speed and direction are highly variable, greater flexibility may be achieved by distributing the extraction vents both along the ceiling and the floor so that $a^2 \gtrsim \frac{1}{2}$ (figure 3.6a). Finally, in regions of relatively light wind activity, optimum performance is obtained by placing extraction vents at floor-level only (*i.e.* $a^2 \simeq 1$; figure 3.6b).

Whichever design strategy is selected, the obvious operating objective is to tune ventilation parameters so that blocked conditions are maintained for a variety of external forcings. Because blocking is favored as q_s is increased, this requires striking some reasonable balance between the volumetric flow rate, Q_s, and reduced gravity, g'_s, of the warm supply air. Contrary to common practice, this procedure may be more delicate than simply increasing the air temperature, which only exacerbates floor-level drafts! Alternatively, Δp (*i.e.* F^2) may be adjusted by employing auxiliary fans or blowers at the extraction vents. This approach must be applied with caution, however. Suppose for example, that extraction vent(s) are located at ceiling-level (*i.e.* $a^2 \simeq 0$). It is energetically wasteful to reduce Δp beyond $\mathrm{F}^2 = \mathrm{F}^2_{NV}$ because at this point cold air will be advected into the building at low levels.

3.6 Conclusions

The design of hybrid buildings in regions displaying a strong seasonal cycle is necessarily complicated by the need to provide adequate ventilation and cooling/heating for a variety of external conditions. Here, we explore one particular aspect of this dilemma in the context of the hysteresis effects that appear when a building is forced by both an internal heat source and an external wind. Further to the analyses of Li & Delsante [50] and Lishman & Woods [57], who considered, respectively, buildings with non-trivial conductive losses and buildings

that contain three openings to the exterior, we demonstrate that the parametric region over which multiple steady states are possible may be significantly reduced by considering a *non-ideal* thermal source with a non-dimensional source volume flux, q_s. Indeed, for sufficiently large q_s there exists an intermediate flow regime between the buoyancy- and wind-dominated states identified by Hunt & Linden [42]. Specifically, for moderate wind forcing, the building may become blocked by which source fluid is discharged to the external environment through both high- and low-level openings (Woods, Caulfield & Phillips [97]).

This discussion is of limited significance in the context of summer-time cooling for which waste heat disposal by natural ventilation is of central concern and deviations from ideal source behavior (*e.g.* by hot machinery) are small. However, the present analysis pertains very directly to the converse problem of winter-time heating (*e.g.* by a forced air system) for which the assumption of ideality cannot be applied. In this circumstance, a blocked flow regime is favored because here alone is infiltration of cold outside air suppressed. Thus, by identifying areas of parameter space in which multiple steady states may occur, we can concurrently identify regions in which blocked conditions represent a unique flow solution to the governing equations. Moreover, for a variety of external forcings (as quantified here by the non-dimensional parameter F of (3.6)), particular designs that optimize ventilation performance may be discerned.

The above results demonstrate that subtle tradeoffs may be needed for buildings that require both active heating and passive cooling. In particular, cooling by natural ventilation favors large opening areas with $a^2 = A_B^2/(A_B^2 + A_T^2) \simeq \frac{1}{2}$. By contrast, winter-time heating favors small opening areas with $a^2 \not\simeq \frac{1}{2}$ in general. Although much of these difficulties may be accommodated by selecting adjustable openings to the exterior, detailed understanding of external conditions and cooling/heating requirements is a clear prerequisite for effective multi-season design. It is hoped that the engineering methodology of § 3.5 provides insights into how such considerations may be applied to real buildings.

Material drawn from this chapter has been submitted for publication to *Building and Environment*, 2006, Flynn, M. R. and C. P. Caulfield (Elsevier Science).

4

Multi-chamber ventilation (ideal source)

4.1 Abstract

Ventilation of adjacent, connected chambers forced by an isolated point source of buoyancy is investigated. There are floor- and ceiling-level external openings in the forced and unforced chambers, respectively, while the partition between the chambers has both a floor- and ceiling-level opening. The flow evolves on the time scale over which the volume flux associated with the plume at the ceiling would fill both chambers. The steady state in the forced chamber is analogous to the single chamber flow described by Linden, Lane-Serff & Smeed [55], with a well-mixed buoyant upper layer which is deeper than in the single chamber flow due to the extra pressure drop at the upper interior opening. The steady state in the unforced chamber inevitably exhibits vertical stratification, and depends on the transient flow, all the opening areas, and the relative plan area of the two chambers, as is verified by laboratory experiments. When the upper interior opening is relatively large, the buoyant layer in the unforced chamber is deeper than the buoyant layer in the forced chamber, which contradicts model predictions based on the assumption that the layers are always well-mixed.

4.2 Introduction

Natural ventilation, by which air circulations within buildings are forced by non-mechanical means, is a cost-effective and energy-efficient way of controlling indoor climate in the presence of internal sources of heat. Although the equations that describe buoyant plumes and thermals have been well-known for some time (see for example Morton, Taylor & Turner [66], Turner [89], Baines & Turner [5], Germeles [30], Manins [62], List [58] and Worster & Huppert [98]), it is only within the past two decades that the benefits of applying this knowledge to architectural design have become fully appreciated (see the review of Linden [53] for details). Most of the studies that have been performed to date consider the ventilation of a single chamber that is connected to the exterior by one or more openings. Analyses have examined both steady state and transient behavior of isolated (Linden *et al.* [55], herein referred to as LLS90, Kaye & Hunt [45]) and distributed sources (Gladstone & Woods [33]), as well as the effect of a finite source volume flux (Woods, Caulfield & Phillips [97]).

The properties of the final steady state may be determined directly from the source conditions and/or the chamber geometry. Whereas interesting phenomena may be encountered during the transient flow approach toward steady state (*e.g.* the 'overshoot' of layer depth remarked upon by Kaye & Hunt [45]), the flow's time history does not affect the steady state.

To demonstrate that this behaviour is not generic, we consider the flow shown schematically in figure 4.1. There is a point source of (constant) buoyancy flux F_0 alone in the left hand (forced) chamber of depth H, and cross-sectional area A_f. (We follow the convention that upper case roman letters are used for dimensional quantities.) This chamber has three openings, with in general different effective cross-sectional areas. (For simplicity of exposition, we absorb experimentally determined discharge coefficients into the various opening areas, and assume that the pressure is constant at openings, i.e. they have infinitesimal depth. This

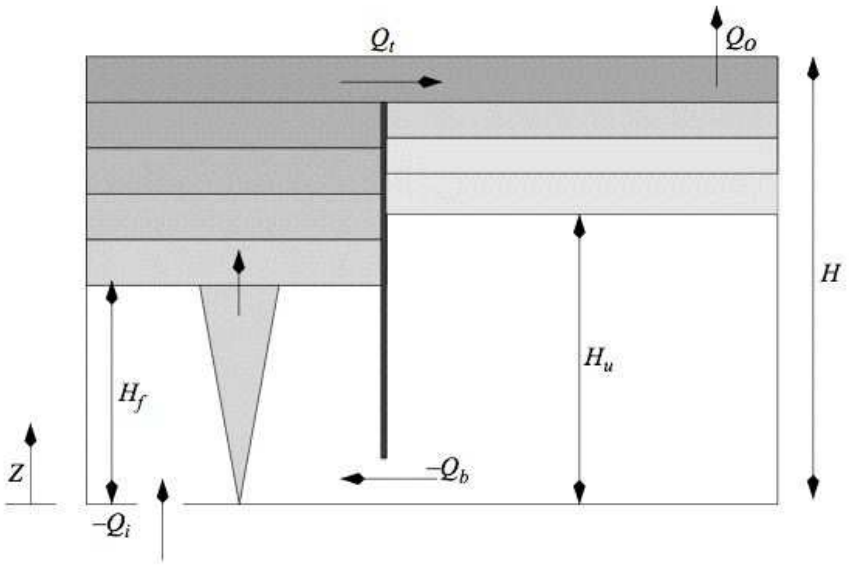

Figure 4.1: Schematic figure of the flow geometry.

ensures unidirectional flow through each opening.) There is one opening (opening 'i' in the figure) to the exterior at the bottom of the chamber $Z = 0$, with effective cross-sectional area A_i. There are also openings at the bottom ($Z = 0$) and top ($Z = H$) of the chambers (labelled 'b' and 't' in the figure) connecting the left hand forced chamber to the right hand (unforced) chamber, (of cross-sectional area A_u). These openings in the central partition have effective cross-sectional areas A_b and A_t respectively. Finally, the unforced chamber has an upper opening at $Z = H$ to the exterior (labelled 'o') with effective cross-sectional area A_o. Although filling box flows in interconnected chambers have been considered before (see Wong & Griffiths [96], Lin & Linden [52]) the principal focus has been on the transient dynamics. The flow geometry considered here tends towards a steady state, which nevertheless is determined by the flow's time history.

In section 4.3, we review the the single chamber model of LLS90, focussing on the aspects of the flow which are particularly relevant to the more general interconnected chamber flow considered here. In section 4.4, we develop models to describe both the steady state and transient flows in the interconnected chamber flow, treating separately cases where the buoyant layers in each chamber

are assumed to be well-mixed or stratified at intermediate times. In section 4.5 we discuss the important characteristics of the results of these models, briefly considering some of the implications for real ventilation flows. In section 4.6 we compare the results of laboratory experiments to our theoretical models, and in section 4.7 we draw conclusions.

4.3 Single chamber dynamics

LLS90 considered the flow in a single forced chamber with high and low level openings to the exterior (i.e. the flow shown in figure 1 in the absence of the central partition). As the buoyant plume fluid rises to the top of the chamber, a filling box flow is assumed to develop (essentially an assumption on the aspect ratio of the chamber: see Baines & Turner [5], Hunt, Cooper & Linden [39] and Conroy, Llewellyn Smith & Caulfield [21] for more detailed discussion), with a buoyant layer deepening towards the floor. The presence of this buoyant layer leads to the pressure $P_f(H)$ within the chamber at $Z = H$ becoming greater than the pressure in the exterior $P_e(H)$ at that height. This pressure differential drives a flow Q_o through the upper opening, which is given by Bernoulli's equation

$$Q_o = A_o \left[\frac{2}{\rho_e} \left(P_f(H) - P_e(H) \right) \right]^{1/2}, \tag{4.1}$$

where ρ_e is the (constant) exterior reference density, and a discharge coefficient has been absorbed into the effective area A_o. This outflow is balanced by an equal and opposite inflow (by convention negative) through the lower opening 'i', i.e.

$$Q_0 + Q_i = 0. \tag{4.2}$$

Assuming that the pressure inside and outside the chamber varies hydrostatically,

$$\begin{aligned} \frac{P_e(0) - P_f(0)}{\rho_e} &= \frac{G}{\rho_e} \int_{H_f}^{H} (\rho_e - \rho_f) \, \mathrm{d}Z - \frac{P_f(H) - P_e(H)}{\rho_e} \\ &= \int_{H_f}^{H} G'_f \, \mathrm{d}Z - \frac{P_f(H) - P_e(H)}{\rho_e}, \end{aligned} \tag{4.3}$$

where H_f is the interface location of the buoyant layer, $\rho_f(Z,T)$ is the density within this buoyant layer, G is the acceleration due to gravity and G'_f is the reduced gravity of the buoyant fluid in this layer. Using Bernoulli's equation at $Z = 0$, we obtain

$$Q_i = -A_i \left[2 \int_{H_f}^{H} G'_f dZ - \frac{Q_o^2}{A_o^2} \right]^{1/2} \tag{4.4}$$

$$\rightarrow -Q_i = Q_o = \frac{A_o A_i}{\left[\frac{1}{2}(A_o^2 + A_i^2)\right]^{1/2}} \left(\int_{H_f}^{H} G'_f \, \mathrm{d}Z \right)^{1/2} \equiv A_\star (I_f)^{1/2}, \tag{4.5}$$

defining the effective opening area parameter $A_\star$ and the buoyancy integral of the forced chamber I_f.

The equation for conservation of mass, under the assumption that diffusive processes are insignificant compared to advective processes, is

$$\frac{\partial}{\partial T}\rho_f = -W_f \frac{\partial}{\partial Z}\rho_f, \tag{4.6}$$

where W_f is the vertical velocity of the buoyant fluid. For the flow to be in steady state, either $\partial \rho_f / \partial Z = 0$, or $W_f = 0$. At steady state, the density is constant everywhere except across a stationary interface at $Z = H_f(t \rightarrow \infty) \equiv H_l$ between a well-mixed buoyant layer and a denser layer of exterior fluid.

In the single chamber flow, the buoyancy integral I_f increases monotonically with time towards a steady state value, although the location of the interface does overshoot its steady state value. The depth of the buoyant layer increases due to the 'filling box' flow of plume fluid entering the layer, and decreases due to the 'draining' outflow Q_o. Q_o increases monotonically with I_f, while the plume volume flux decreases monotonically as the depth of the layer increases. Since we assume that the plume fluid spreads instantaneously horizontally with no vertical mixing upon arrival at the ceiling of the chamber, the buoyant layer always exhibits some vertical stratification for $t < \infty$.

The depth of the stratified layer always reaches its steady state value before I_f has grown to its ultimate steady state value. This mismatch inevitably leads to an overshoot in the depth of the buoyant layer, as $Q_o < Q_p(H_l)$ at this time.

(Kaye & Hunt [45] discuss the time-dependent behaviour of this system in some detail, under the different simplifying assumption that the buoyant layer is well-mixed for all time, which leads to the different conclusion that the interface location does not always overshoot. Although for flows in single chambers this difference of approach leads to only slight quantitative differences, as we discuss in more detail below, the well-mixed assumption cannot be applied to both interconnected chambers without leading to significant quantitative error.)

As the buoyancy flux F_0 in the plume is constant before its arrival at the interface, the reduced gravity of the plume fluid G'_p at the interface can be simply determined from the classical point source similarity solution of Zeldovich [102] and Morton *et al.* [66]:

$$G'_p(Z) = \frac{F_0}{Q_p(Z)} = \frac{F_0}{\lambda F_0^{1/3} Z^{5/3}};\ \lambda = \frac{6\alpha}{5}\left(\frac{9\alpha\pi^2}{10}\right)^{1/3}, \tag{4.7}$$

where α is the (assumed universal) entrainment constant. The requirements of constant steady state density and volume of the buoyant layer are that $G'_f = G'_p(H_l)$ and $Q_p(H_l) = Q_o$, and so the purely geometric condition defined by LLS90 must hold:

$$\lambda^3 H_l^5 = {A_\star}^2 (H - H_l). \tag{4.8}$$

Furthermore, the steady state is completely independent of the flow's time history.

4.4 Interconnected chamber dynamics

For interconnected chambers, as shown in figure 4.1, (4.2) must still hold. Considering each chamber separately, we obtain

$$Q_b + Q_t = Q_o = -Q_i, \tag{4.9}$$

where Q_b and Q_t are defined as being positive for outflow from the forced chamber.

There is always outflow through opening 'o', inflow through opening 'i', and outflow from the forced chamber through opening 't'. This implies that

$P_f(H) > P_u(H) > P_e(H)$ and $P_e(0) > P_f(0)$, and so

$$\begin{aligned} Q_o &= A_o \left[\frac{2}{\rho_e}\left(P_u(H) - P_e(H)\right)\right]^{1/2}, \\ Q_t &= A_t \left[\frac{2}{\rho_e}\left(P_f(H) - P_u(H)\right)\right]^{1/2}, \\ Q_i &= -A_i \left[\frac{2}{\rho_e}\left(P_e(0) - P_f(0)\right)\right]^{1/2}. \end{aligned} \tag{4.10}$$

where we have absorbed any discharge coefficients into the effective areas. Assuming that the pressure distribution is hydrostatic, we obtain

$$\frac{P_e(0) - P_f(0)}{\rho_e} = I_f - \frac{([P_f(H) - P_u(H)] + [P_u(H) - P_e(H)])}{\rho_e}, \tag{4.11}$$

and so

$$\frac{Q_i}{A_i} = -\left(2I_f - \frac{Q_o^2}{A_o^2} - \frac{Q_t^2}{A_t^2}\right)^{1/2} \rightarrow -Q_i = Q_o = A_\star \left(I_f - \frac{Q_t^2}{2A_t^2}\right)^{1/2} \tag{4.12}$$

Comparing (4.5) to (4.12), the presence of the unforced chamber, and hence the associated two stage pressure drop between the forced chamber and the exterior at $Z = H$ manifests itself by a reduction in the ventilation flow through the entire system.

4.4.1 Steady state flow for interconnected chambers

In steady state, since the depths of both buoyant layers are constant, $Q_b(0) = 0$ and hence $P_f(0) = P_u(0)$. Therefore

$$\begin{aligned} 0 = \frac{2}{\rho_e}[P_f(0) - P_u(0)] &= \frac{2}{\rho_e}[P_f(H) - P_u(H)] + 2\int_{H_u}^{H} G'_u \, \mathrm{d}Z - 2I_f, \\ &= \frac{Q_t^2}{A_t^2} - 2(I_f - I_u), \end{aligned} \tag{4.13}$$

where $G'_u = G(\rho_e - \rho_u)/\rho_e$ is the reduced gravity of the buoyant layer in the unforced chamber, and I_u is the related buoyancy integral. Combining this expression with (4.12), we obtain

$$\begin{aligned} Q_i^2 = Q_t^2 = Q_o^2 = {A_\star}^2 I_u &= \frac{2A_o^2 A_i^2 A_t^2 I_f}{A_o^2 A_i^2 + A_o^2 A_t^2 + A_i^2 A_t^2} \\ &= {A_\star}^2 I_f \left(\frac{2A_t^2}{{A_\star}^2 + 2A_t^2}\right). \end{aligned} \tag{4.14}$$

At steady state, the properties of the buoyant layer in the forced chamber can be simply determined, and the depth and reduced gravity of this layer are completely independent of the flow's time history. The volume flux out of the buoyant layer in the forced chamber (here Q_t) must be balanced by the volume flux into the layer from the plume, while the density of the (well-mixed) layer in the forced chamber must be balanced by the incoming density of the plume, and so the analogue of (4.8) is

$$\lambda^3 H_{f\infty}^5 = {A_\star}^2 (H - H_{f\infty}) \left(\frac{2A_t^2}{{A_\star}^2 + 2A_t^2} \right) = {A_\dagger}^2 (H - H_{f\infty}), \qquad (4.15)$$

defining a new effective opening area $A_\dagger$ for the interconnected chamber flow. Since $A_\dagger \leq A_\star$, the steady state buoyant layer is always deeper in the interconnected forced chamber than in the single chamber, (i.e. $H_{f\infty} < H_l$ where H_l is defined in (4.8)) and hence the ventilation flow Q_o is always less, due to the extra pressure drop across the unforced chamber.

When $A_t \gg A_\star$, $A_\dagger \simeq A_\star$, and so the presence of the partition has little influence on the steady state flow. Conversely, when $A_t \ll A_\star$, the interface location is completely dominated by the value of A_t, as (4.15) reduces to $\lambda^3 H_{f\infty}^5 \simeq 2A_t^2 (H - H_{f\infty})$. This is analogous to the behaviour of the single chamber flow, as noted in LLS90, where if A_i and A_0 are very different in size, $A_\star \simeq \sqrt{2}\min(A_i, A_o)$, and the flow is controlled by the smaller of the two opening areas.

From (4.14), the steady state flow can also be related to the buoyancy integral I_u for the unforced chamber, in a form identical to the condition (4.5) which pertains in the single chamber flow, since at steady state $P_f(0) = P_u(0)$. Therefore, the pressure difference driving the flow through Q_i is the same as the pressure difference between the exterior and the *unforced* chamber at $Z = 0$. However, everywhere except at the ceiling of the unforced chamber, where since $Q_t = Q_o$ the buoyant fluid entering the unforced chamber immediately leaves, the steady state flow is stationary in the unforced chamber, and so the properties of the unforced layer cannot be determined without considering the complete flow history. Indeed, since the buoyant layer develops transiently due to more buoyant fluid flowing

into the unforced chamber (through opening 't' from the forced chamber) than is driven out to the exterior through opening 'o' to the exterior, the buoyant layer in the unforced chamber must be vertically stratified in a way determined by the transient evolution.

4.4.2 Transient flow dynamics for interconnected chambers

As we discuss in Appendix A, it is possible to establish that $Q_b \leq 0$, and so there is never any flow through opening 'b' from the forced chamber into the unforced chamber, if the buoyant layer in the unforced chamber is assumed to be stratified. Therefore,

$$Q_b = -A_b \left(\frac{2}{\rho_e} [P_u(0) - P_f(0)] \right)^{1/2} = -A_b \left[2(I_f - I_u) - \frac{Q_t^2}{A_t^2} \right]^{1/2}, \tag{4.16}$$

using (4.10), closing the transient system. It is convenient for the subsequent analysis to nondimensionalize the flow quantities.

From the properties of the steady state, $A_\star$ still figures prominently, and so we use $A_\star$ to scale the two interior opening areas

$$a_t = \frac{A_t}{A_\star},\ a_b = \frac{A_b}{A_\star},\ a_\dagger = \frac{A_\dagger}{A_\star} = \left(\frac{2a_t^2}{1 + 2a_t^2} \right)^{1/2}. \tag{4.17}$$

(We follow the convention that lower case roman letters are used for nondimensional quantities.) Volume fluxes are nondimensionalized with the volume flux Q_H which a point source plume with buoyancy flux F_0 satisfying the similarity solution (4.7) would have at the ceiling, i.e.

$$q_o = \frac{Q_o}{Q_H},\ q_i = \frac{Q_i}{Q_H},\ q_t = \frac{Q_t}{Q_H},\ q_b = \frac{Q_b}{Q_H},\ Q_H = \lambda F_0^{1/3} H^{5/3}. \tag{4.18}$$

The natural time scale for the flow is the filling box time scale for the *two* chamber system, defined here as

$$T_f = \frac{(A_f + A_u)H}{Q_H}, \tag{4.19}$$

i.e. the time that a source with volume flux Q_H would take to fill both chambers (with total cross-sectional area $A_f + A_u$). The relative volume of the two chambers

plays a critical role in the time-dependent behaviour of the system, and so we define the nondimensional quantity $a_u = A_u/A_f$. We also scale vertical distances with the depth H, i.e. $z = Z/H$, $h_f = H_f/H$, $h_u = H_u/H$, $h_{f\infty} = H_{f\infty}/H$, and $h_l = H_l/H$.

We choose to use H and $G'_H = F_0/Q_H$, the reduced gravity at the ceiling of a point source plume with buoyancy flux F_0 to scale the buoyancy integrals, i.e.

$$i_u = \frac{I_u}{G'_H H} = \frac{\lambda H^{2/3} I_u}{F_0^{2/3}},\ i_f = \frac{\lambda H^{2/3} I_u}{F_0^{2/3}}. \tag{4.20}$$

Therefore, at steady state

$$i_u = {a_\dagger}^2 i_f, \tag{4.21}$$

while, in general

$$q_o + q_i \ = \ 0,\ q_b + q_t = q_o,\ 2q_o^2 + \frac{q_t^2}{a_t^2} = \frac{2i_f}{\mu^2}, \tag{4.22}$$

where μ is the nondimensional opening area parameter (or equivalently time scale ratio) as defined in Kaye & Hunt [45], i.e.

$$\mu^2 = \frac{\lambda^3 H^4}{A_\star^2} = \frac{T_d^2}{T_f^2}. \tag{4.23}$$

The draining time scale T_d is defined as

$$T_d = \frac{(A_f + A_u)H}{A_\star (G'_H H)^{1/2}}. \tag{4.24}$$

This time scale is the characteristic time scale for buoyant fluid with this reduced gravity to drain from the two chambers, in the absence of the internal partition. (See Kaye & Hunt [45] for a more detailed discussion.)

Nondimensionalizing (4.16), we obtain

$$\frac{q_b^2}{a_b^2} = \frac{2(i_f - i_u)}{\mu^2} - \frac{q_t^2}{a_t^2}. \tag{4.25}$$

Combining this equation with (4.22), it is apparent that, provided $q_o \le q_t$,

$$i_u \le \mu^2 q_o^2 \le {a_\dagger}^2 i_f, \tag{4.26}$$

and so ${a_\dagger}^2 i_f - i_u \geq 0$, and i_u approaches its steady state value from below for circumstances where the buoyant layer in the unforced chamber is assumed to remain stratified, since as discussed in Appendix A, the flow through opening 'b' is unidirectional.

Using (4.22) and (4.25), to eliminate q_b and q_t, q_o^2 must satisfy a quadratic equation. Requiring that q_o converges towards its steady state value $q_o \to \sqrt{i_u}/\mu$, we obtain

$$\begin{aligned} q_o^2 &= \frac{i_u}{\mu^2} + \frac{4a_b^2 i_u + [1 + 2(a_t^2 + a_b^2)][1 + 2a_t^2][{a_\dagger}^2 i_f - i_u]}{\mu^2[1 - 4(a_b^2 - a_t^2) + 4(a_b^2 + a_t^2)^2]} \\ &\quad - \frac{[16a_b^4 i_u^2 + 16a_b^2(1 + 2a_t^2)({a_\dagger}^2 i_f - i_u)(a_b^2 i_u + a_t^2 i_f)]^{1/2}}{\mu^2[1 - 4(a_b^2 - a_t^2) + 4(a_b^2 + a_t^2)^2]}. \end{aligned} \tag{4.27}$$

All the other volume fluxes can be determined from (4.22).

We assume that the plume is rising from a 'point' source of buoyancy flux alone. We also assume that the plume is sufficiently narrow so that it may be modelled as isolated, and so that, at all heights within the plume $\pi B^2 \ll A_f$, where B is the plume radius. This conventional assumption (see Conroy *et al.* [21] for a detailed discussion) also ensures that the aspect ratio of the chamber is sufficiently small for a quasi-steady approximation to be made, so the plume rising through the chamber may be treated as flowing through a time-independent ambient, which in turn evolves on a very much slower time scale.

Also, as mentioned in the Introduction, we assume that the aspect ratio is sufficiently small so that a 'filling box' flow can develop, with the plume fluid arriving at the top of the chamber and spreading to form a buoyant layer (thus leading to stratification in the chamber) rather than driving an overturning, mixing the fluid in the entire chamber. Finally, we assume that the flow is at sufficiently high Reynolds numbers so that advective processes dominate diffusive processes. We make a similar assumption in the unforced chamber, so that flow through opening 't' is not fast enough to overturn the buoyant layer in the unforced chamber. Nevertheless, for solving the transient problem, four different possibilities exist, since the buoyant layer in each chamber can be modelled as either well-mixed or

continuously stratified.

Stratified buoyant layer in the forced chamber

In the forced chamber, using the nondimensionalization chosen, the plume equations are

$$\begin{aligned} \frac{\partial}{\partial z}q &= \frac{5}{3}m^{1/2}, \\ \frac{\partial}{\partial z}m &= \frac{4fq}{3m}, \\ \frac{\partial}{\partial z}f &= -q\frac{\partial}{\partial z}g'_f, \end{aligned} \tag{4.28}$$

where

$$q = \frac{Q}{Q_H},\ m = \frac{M}{M_H} = \frac{M}{\left(\frac{9\alpha\pi^2 F_0 H^2}{10}\right)^{2/3}},\ f = \frac{F}{F_0},\ g'_f = \frac{G'_f}{G'_H}, \tag{4.29}$$

and the boundary conditions are $q(0) = 0 = m(0)$, $f(0) = 1$. The system is closed by considering the equation for conservation of mass (4.6) at all heights in the forced chamber. Under the above assumptions, the return velocity W_f of ambient fluid in the forced chamber is $-(Q - Q_t)/A_f$, as there is a net flow of Q_t through the chamber. Therefore, g'_f satisfies

$$\frac{\partial}{\partial t}g'_f = -(q - q_t)(1 + a_u)\frac{\partial}{\partial z}g'_f, \tag{4.30}$$

with initial condition $g'_f(z) = 0$.

Equations (4.28) and (4.30) can be solved using the method of Germeles [30], who developed a numerical model for single chamber flow to solve (4.28) and (4.30). The plume equations are integrated through the ambient chamber stratification, modelled by a sufficiently large number of discrete layers, separated by interfaces. The location of each interface is then updated using (4.30). At every time step, a new layer is added at the ceiling of the chamber , with reduced gravity $g'_p(1)$ given by the reduced gravity of the arriving plume fluid, which is assumed to spread out instantly without any mixing. This model can be straightforwardly generalized to the interconnected chamber case by tracking correctly the volume

flux q_t and the reduced gravity of fluid which leaves through opening 't' at any time instant. Using (4.22) and (4.27), q_t can be determined provided i_u and i_f are determined. The integrals i_f and i_u are calculated directly from the chambers' reduced gravity distribution.

Well-mixed buoyant layer in the forced chamber

As noted by Baines & Turner [5], and discussed by Worster & Huppert [98], the density stratification which develops typically has a weak variation through much of the buoyant layer, with a region of strong variation near the base. Also, as noted by Kaye & Hunt [45], in laboratory experiments, there is inevitably some mixing as the plume fluid spreads at the ceiling of the chamber. It is appealing to assume that the layer is well-mixed, (mimicking the steady state) and so only the interface location h_f and the well-mixed layer reduced gravity g'_f need to be modelled. We obtain

$$\frac{\mathrm{d}}{\mathrm{d}t}h_f \;=\; (1+a_u)(q_t - h_f^{5/3}),\;\; \frac{\mathrm{d}}{\mathrm{d}t}g'_f = \frac{(1+a_u)(1-g'_f h_f^{5/3})}{1-h_f}. \qquad (4.31)$$

These coupled equations then can be used to describe the evolution of the buoyant layer in the forced chamber, once again provided q_t can be identified, and hence provided i_u is known, as in this case, there is the simple relationship $i_f = g'_f(1-h_f)$.

Stratified buoyant layer in the unforced chamber

Since the unforced chamber is supplied horizontally through opening 't', the likelihood of substantial overturning within the chamber as the buoyant layer develops is not as significant as in the forced chamber, and the steady state is not necessarily well-mixed. As already noted $q_o \leq q_t$ at all times, and so the buoyant layer is continually supplied by incoming fluid from the forced chamber through opening 't', of reduced gravity $g'_t = g'_p(1)$ if the forced chamber is assumed to be stratified, or $g'_t = g'_f$ if it is assumed to be well-mixed. If we assume that there is no mixing in the unforced chamber, the net volume flux of $q_t - q_o$ spreads

out layer by layer, developing a vertical stratification in the unforced chamber. The depth of this layer, and the value of the integral i_u can be calculated by tracking all these incoming layers, which descend at the same nondimensional speed $(q_o - q_t)(1 + a_u)/a_u$ in the unforced chamber.

Well-mixed buoyant layer in the unforced chamber

Of course, if it is assumed that the fluid in the unforced chamber is well-mixed, it can be characterized by a single reduced gravity g'_u and the interface location h_u. The equations for the evolution of these quantities then take the form

$$\frac{\mathrm{d}}{\mathrm{d}t}h_u = \frac{(q_t - q_o)(1 + a_u)}{a_u}, \ \frac{\mathrm{d}}{\mathrm{d}t}g'_u = \frac{(g'_t - g'_u)(1 + a_u)q_t}{a_u(1 - h_u)}, \tag{4.32}$$

where g'_t is the reduced gravity of the fluid entering through opening 't'. This last equation is particularly interesting, as it does not involve the flow through opening 'o' at all. Indeed, as we discuss in Appendix B, for this well-mixed model it is possible for the flow to reverse direction through opening 'b', and hence for the interface location h_u in the unforced room to overshoot its final position. The steady state associated with this well-mixed model occurs when $q_t = q_o$, and hence the two interfaces are stationary. However, (4.32) implies at steady state that $g'_f = g'_u$. Therefore, from (4.14), at steady state,

$$g'_u(1 - h_u) = a_\dagger^2 g'_f(1 - h_f) \rightarrow (1 - h_u) = \frac{2a_t^2}{1 + 2a_t^2}(1 - h_f), \tag{4.33}$$

and so the buoyant layer depth in the unforced chamber is predicted to be always less than the buoyant layer depth in the forced chamber.

We are not aware of a careful analysis of the dependence of the predictions of transient models on mixing assumptions within developing layers, even in the single chamber case. Here we will compare the results of the two extreme situations, i.e. we will assume that both chambers remain stratified, (which we refer to subsequently as the S-S model, denoting stratification in both chambers) or that both may be modelled with well-mixed buoyant layers (referred to as the M-M model, denoting well-mixed models in both chambers).

There is still a very large parameter space which could be considered. We choose a single value of $\mu = 4$, which corresponds to a steady state interface for the single chamber flow at the midpoint $h_l = 1/2$ of the chamber. This choice avoids extreme values for the buoyant layer depth in the forced chamber of the interconnected chamber flow. We are considering a situation where the draining time scale T_d (4.24) is larger than the filling box time scale T_f, (4.19) but of the same order. To identify the influence of the other parameters, we consider eight different situations in detail, with essentially 'large' and 'small' values for each of the three areas a_t, a_b and a_u. We are particularly interested in the extent to which the reduced well-mixed M-M model agrees with the more detailed stratified S-S model.

We have chosen the parameters deliberately to avoid certain complicated flow regimes, which though potentially interesting, are beyond the scope of the present study. For example, if the opening areas are chosen to be sufficiently small, so that $H_{f\infty}$ (as defined in (4.15)) is sufficiently close to zero, exchange flow may occur at opening 'b' of buoyant fluid between the two chambers. A similar phenomenon may occur (particularly when the unforced chamber is sufficiently narrow compared to the forced chamber, and $H_{f\infty}$ is sufficiently small) with the buoyant layer flowing from unforced chamber into the forced chamber, thus leading to a recycling of buoyant fluid (a phenomenon related to the some of the flows considered in Wong & Griffiths [96]).

4.5 Model results

We consider the eight different combinations of $a_u = 1/2$ and 2, (corresponding to our experimental situation) $a_t^2, a_b^2 = 1/10$, and $a_t^2, a_b^2 = 10$. In figures 4.2-4.4, we compare the important mean flow quantities predicted by the M-M and S-S models for the various flow geometries: the flow rates q_t and q_o out of the forced chamber and unforced chamber; the buoyant layer depths h_f and h_u; and

the mean (or well-mixed) reduced gravities, which for the S-S model, are defined as

$$\overline{g'_f} = \frac{i_f}{1-h_f},\ \overline{g'_u} = \frac{i_u}{1-h_u}. \tag{4.34}$$

As shown in figure 4.2, in general there is a quite close agreement between the flow rates predicted by the well-mixed M-M model and the stratified S-S model, implying that the predicted values of i_f and i_u also agree closely. From (4.14), increasing a_t increases the steady state value of the flow rate through the system. Perhaps most interestingly, increasing a_t and especially a_b leads to significant transient increase in q_t, which is substantially larger than q_o particularly when the forced room is relatively small compared to the unforced room, (and hence a_u is large). This transient response is due to the combination of two effects: the relatively rapid deepening of the buoyant layer in the forced room, and the large cross-sectional area of the internal openings allowing substantial flow from the forced room to the unforced room. For the well-mixed M-M model, typically $q_t < q_o$ eventually, so (4.39) is used to determine the flow rates, and the M-M model predicts overshoot of the unforced layer interface, although this overshoot is quite small.

As is apparent in figures 4.3 and 4.4, for the forced chamber, the well-mixed M-M model also agrees closely with the stratified S-S model, as the plume dynamics rapidly lead to the density distribution in the forced chamber being well-mixed. The interface location in the forced chamber also exhibits overshoot, and typically converges to a value somewhat less than that predicted for a single chamber flow, ($h_l = 1/2$). When the interconnecting openings are relatively large, and so flow between the two chambers is relatively large, the reduction in the steady state interface location is relatively small. However decreasing a_t can reduce the interface location substantially, as in this case the controlling opening area $A_\dagger \sim A_t$ in (4.15). This reduction in turn increases the steady state value of $\overline{g'_f}$ substantially.

When a_t^2 is small, the system with a relatively small forced chamber cross-sectional area (i.e. a_u large, plotted with dashed lines) exhibits slightly more rapid

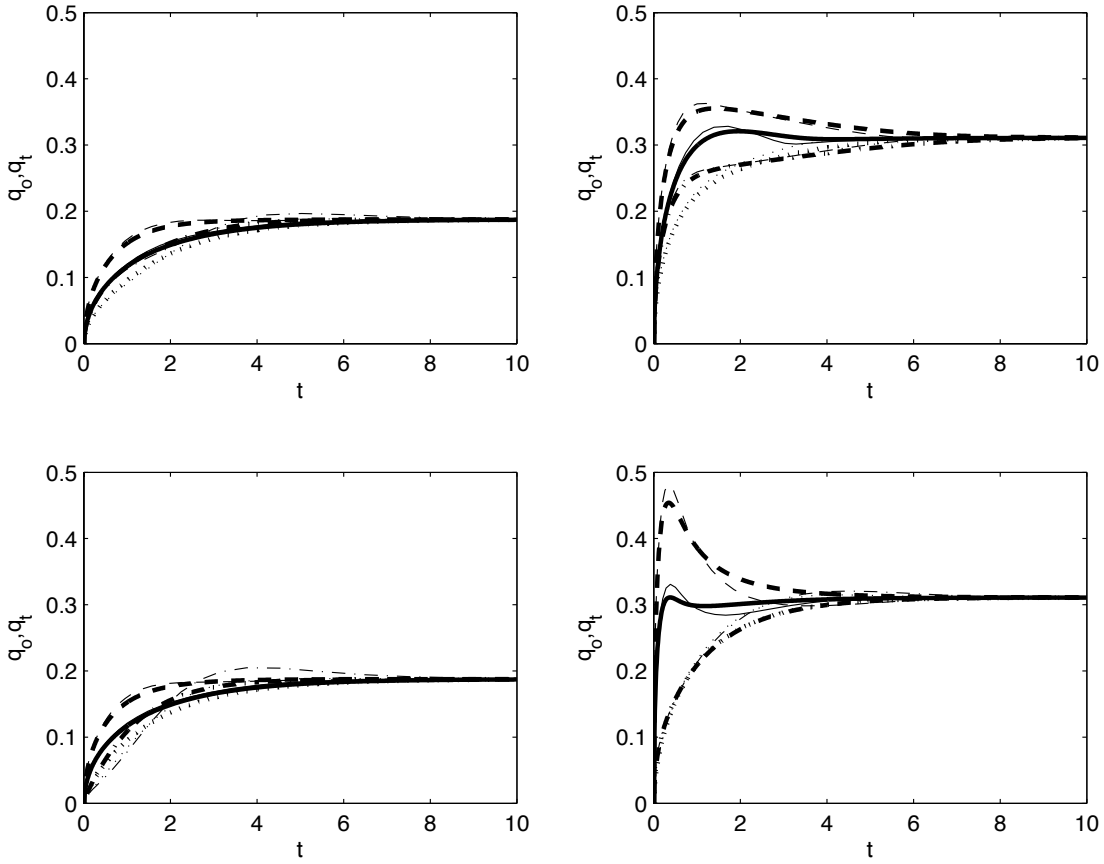

Figure 4.2: Plots against time of q_t (plotted with a solid line for systems with $a_u = 1/2$, and with a dashed line for $a_u = 2$) and q_o (dotted line for $a_u = 1/2$ and dot-dashed line for $a_u = 2$) as predicted by the stratified S-S model (thick lines) and reduced M-M model (thin lines) for systems with $h_l = 1/2$ and: a) $a_t^2 = 0.1$, $a_b^2 = 0.1$; b) $a_t^2 = 10$, $a_b^2 = 0.1$; c) $a_t^2 = 0.1$, $a_b^2 = 10$; d) $a_t^2 = 10$, $a_b^2 = 10$.

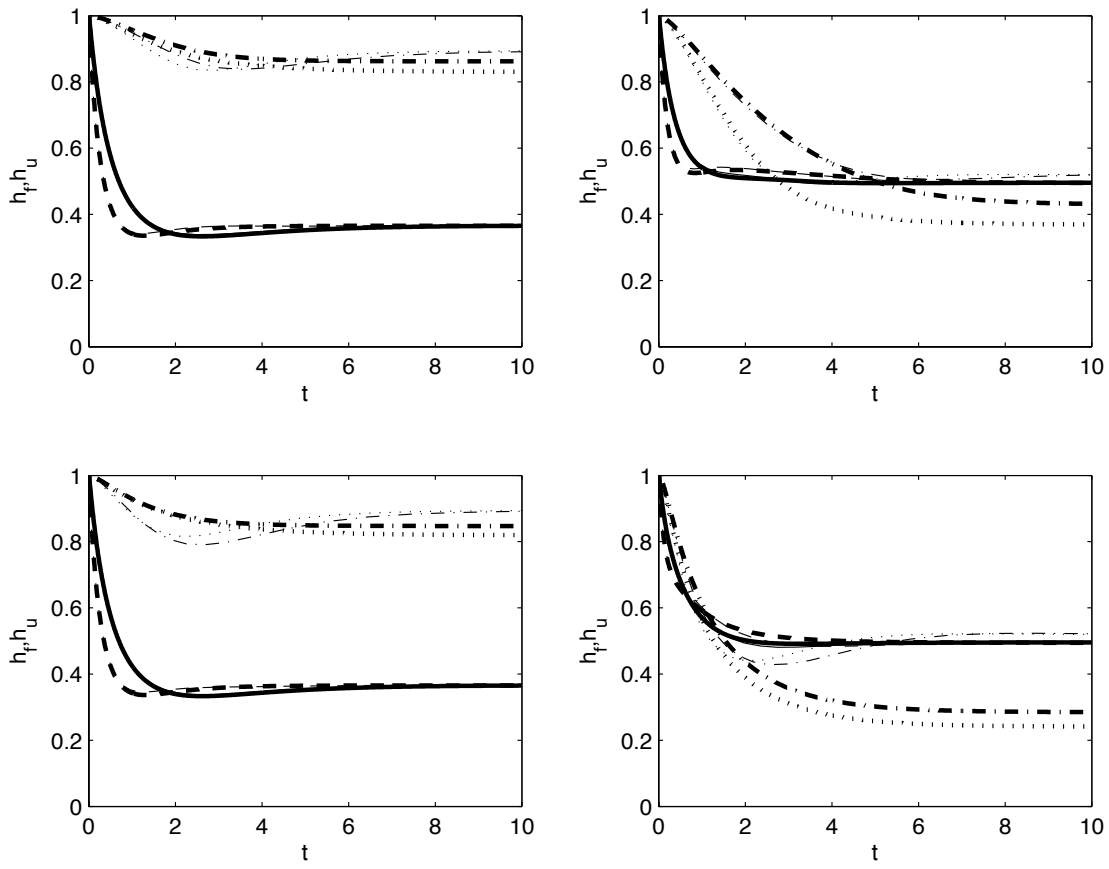

Figure 4.3: Plots against time of the forced chamber interface location h_f (plotted with a solid line for systems with $a_u = 1/2$, and with a dashed line for $a_u = 2$) and the unforced chamber interface location h_u (dotted line for $a_u = 1/2$ and dot-dashed line for $a_u = 2$) as predicted by the stratified S-S model (thick lines) and reduced M-M model (thin lines) for systems with $h_l = 1/2$ and: a) $a_t^2 = 0.1$, $a_b^2 = 0.1$; b) $a_t^2 = 10$, $a_b^2 = 0.1$; c) $a_t^2 = 0.1$, $a_b^2 = 10$; d) $a_t^2 = 10$, $a_b^2 = 10$.

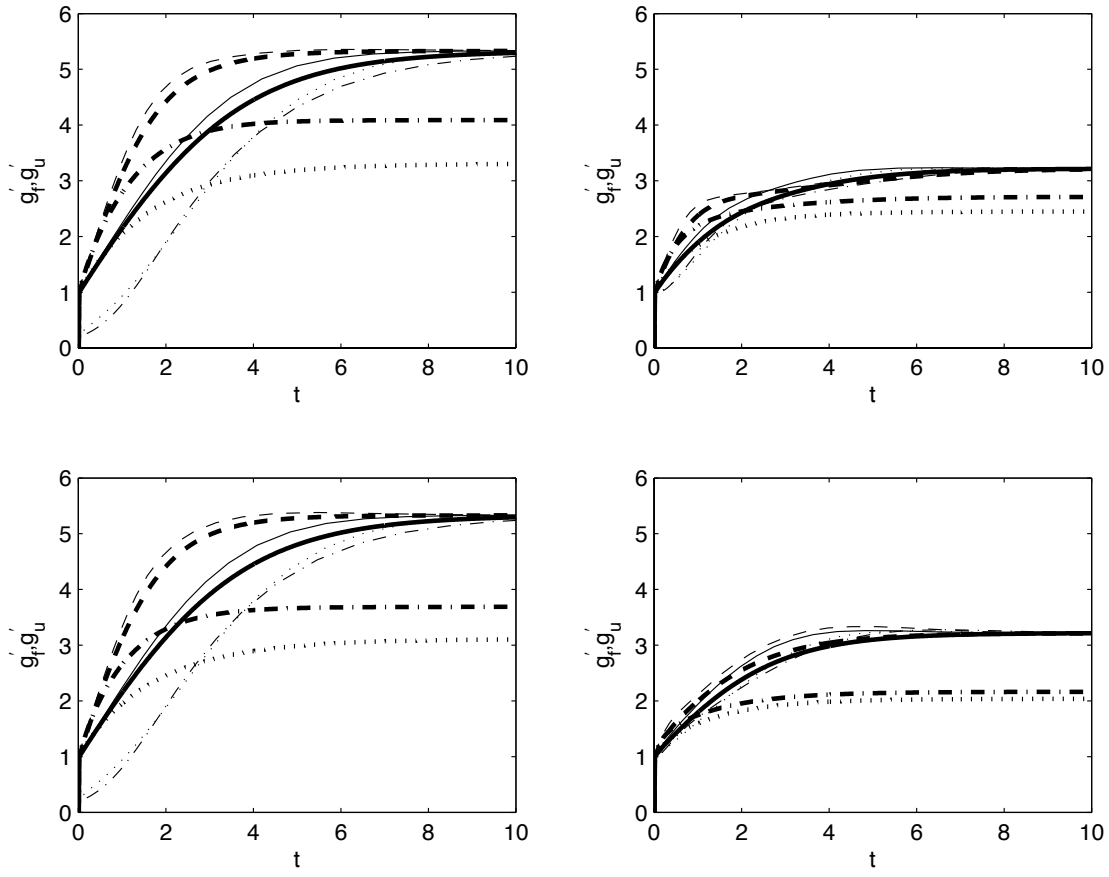

Figure 4.4: Plots against time of the mean or well-mixed forced chamber reduced gravity $\overline{g'_f}$ (plotted with a solid line for systems with $a_u = 1/2$, and with a dashed line for $a_u = 2$) and the mean or well-mixed unforced chamber reduced gravity $\overline{g'_u}$ (dotted line for $a_u = 1/2$ and dot-dashed line for $a_u = 2$) as predicted by the stratified S-S model (thick lines) and reduced M-M model (thin lines) for systems with $h_l = 1/2$ and: a) $a_t^2 = 0.1$, $a_b^2 = 0.1$; b) $a_t^2 = 10$, $a_b^2 = 0.1$; c) $a_t^2 = 0.1$, $a_b^2 = 10$; d) $a_t^2 = 10$, $a_b^2 = 10$.

deepening and rapid increase in $\overline{g'_f}$ than the system with smaller a_u (plotted with solid lines). This is due to the restriction of flow through opening 't' leading to a disproportionate amount of buoyant fluid remaining in the forced chamber, which leads both to rapid deepening and more rapid increase in reduced gravity. The area of the lower 'b' opening also has an effect on the speed of convergence of the forced layer to its steady state value, particularly when a_t is large, although there is no effect of either a_u or a_b on the ultimate steady state in the forced chamber. As is apparent in figures 4.2b and d, smaller a_b corresponds to a smaller peak value of q_t, as the communication between the two chambers is somewhat suppressed.

There are significant differences between the predictions of the two models for the properties of the flow in the unforced chamber. For the stratified S-S model, there is strong dependence of the ultimate steady states on all of the area parameters: a_t, a_b and a_u. In general, increasing a_u increases the steady state values of h_u and $\overline{g'_u}$ in such a way that the steady state value of $i_u = \overline{g'_u}(1 - h_u)$ is constant. When a_u is larger, the buoyant layer tends to be shallower in the unforced chamber, and so the steady state reduced gravity is somewhat larger. The relative change in $\overline{g'_u}$ is largest when a_b and in particular a_t is small, as that corresponds to small values of the unforced chamber's buoyant layer depth $1 - h_u$, which exhibit large relative changes with a_u.

Although increasing a_b tends to decrease both interface height and reduced gravity at steady state, by far the strongest effects are associated with variations in a_t. Increasing a_t, and thus allowing for increased volume flow between the two chambers even at steady state, leads inevitably to a significant increase in the depth of the unforced buoyant layer. This deeper layer typically also has a smaller reduced gravity. Relatively more of its volume comes from the early, transient, peak of volume flow through the upper opening, which has low reduced gravity since it comes from plume fluid which has been diluted through entrainment by ambient fluid through virtually all of its rise.

Furthermore, typically, the mean reduced gravity is lower eventually in

the unforced chamber than in the forced chamber, due to the fact that the buoyant layer in the unforced chamber always contains fluid of relatively low reduced gravity from early in the flow evolution, when the plume has been strongly diluted. Essentially, the stratified S-S model predicts widely varying relative depths of the two buoyant layers. Small values of a_t, (and thus little flow between the two chambers at early times) implies that $h_u > h_f$, (figure 4.3a) while larger values of a_t (and to a lesser extent a_b) and hence larger flow rates q_t imply substantially smaller values of h_u (figure 4.3d).

The predictions of the well-mixed M-M model are qualitatively different. The reduced gravity of the unforced layer always converges to that of the forced layer. This forces the interface location to be given by the simple formula (4.33), predicting that $h_u > h_f$ in all cases, which is qualitatively different from the S-S model, as shown in figure 4.3. The M-M model predicts overshoot in the unforced layer's interface location in all cases, and a little variation in h_u with the parameter a_u. Figure 4.4 shows that the predictions for $\overline{g'_u}$ also depend weakly on a_u. For smaller values of a_t, convergence to g'_f is somewhat slower, due to the restriction of flow between the two chambers.

For the S-S model, we also plot the evolution of the vertical profiles of reduced gravity g'_f and g'_u in figures 4.5 and 4.6 respectively at $t = n/2$, $n = 1, 2, \ldots, 20$ for systems with $a_u = 1/2$, $h_l = 1/2$, and the four previously used choices of a_t and a_b. (The interfaces move downwards slightly more rapidly in the forced chamber and conversely more slowly in the unforced chamber when $a_u = 2$, as in each case the downwards propagation is relatively faster in the relatively smaller chamber.) The evolution of the reduced gravity profile in the forced chamber is very similar to the emptying filling box behaviour in a single chamber previously considered in LLS90. Quite rapidly, the buoyant layer becomes essentially well-mixed, and there is little vertical variation in density, and hence little impact on q_t, h_f and $\overline{g'_f}$, and so it is unsurprising that the predictions of the two models agree closely.

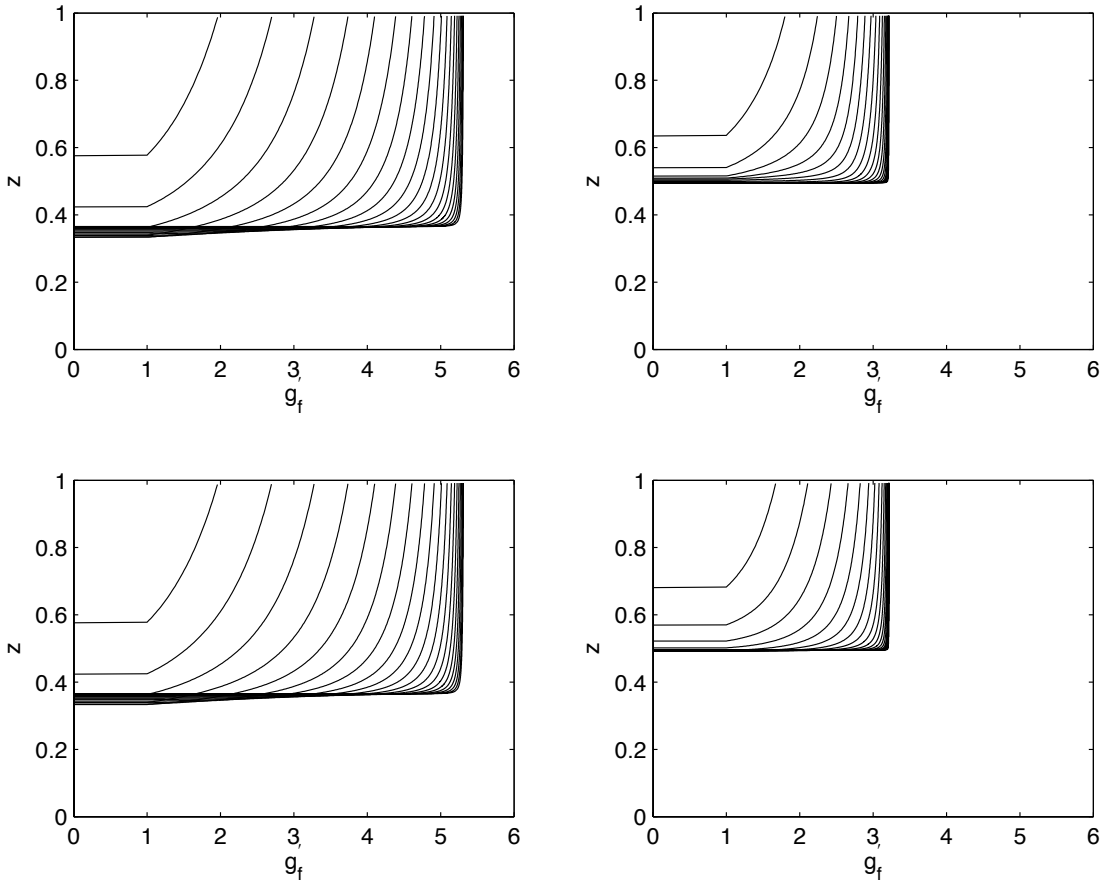

Figure 4.5: Profiles of $g'_f(z)$ predicted by the stratified S-S model at times $t = n/2$, $n = 1, 2, \ldots, 20$ for systems with $a_u = 1/2$, $h_l = 1/2$, and: a) $a_t^2 = 0.1$, $a_b^2 = 0.1$; b) $a_t^2 = 10$, $a_b^2 = 0.1$; c) $a_t^2 = 0.1$, $a_b^2 = 10$; d) $a_t^2 = 10$, $a_b^2 = 10$.

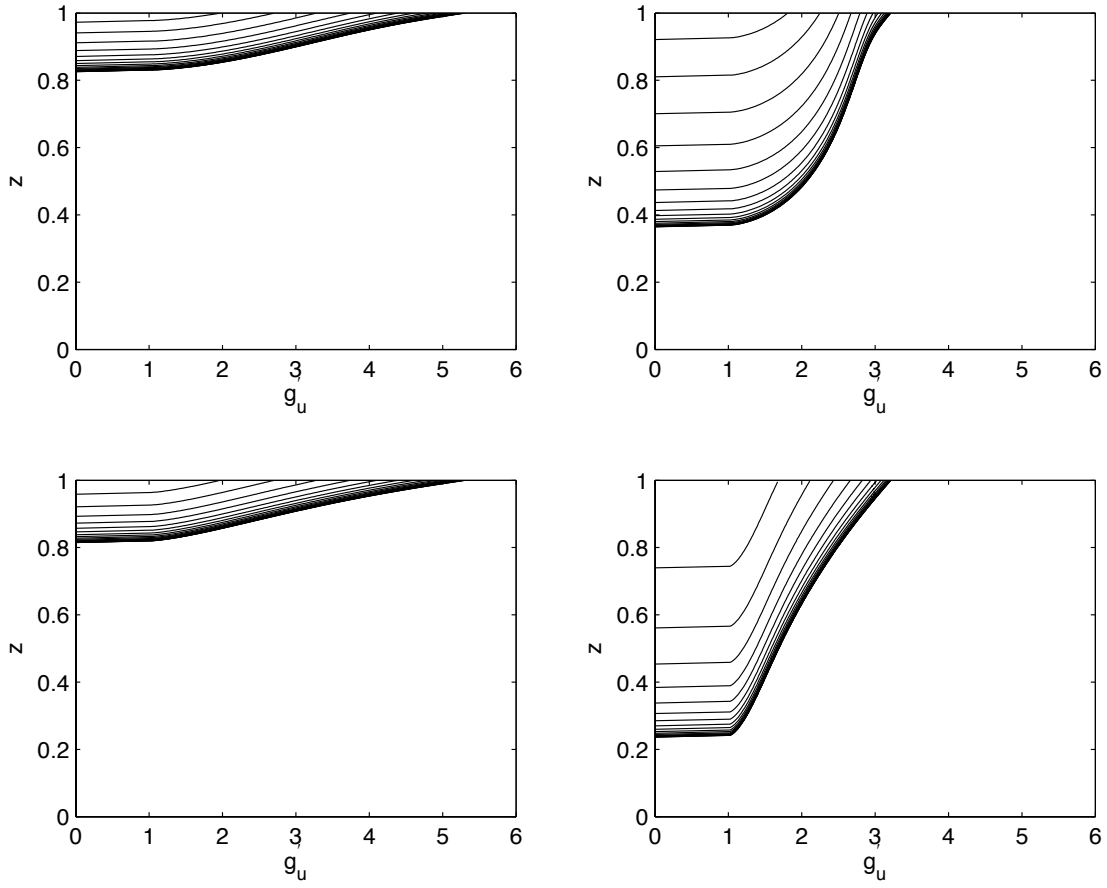

Figure 4.6: Profiles of $g'_u(z)$ predicted by the stratified S-S model at times $t = n/2$, $n = 1, 2, \ldots, 20$ for systems with $a_u = 1/2$, $h_l = 1/2$ and: a) $a_t^2 = 0.1$, $a_b^2 = 0.1$; b) $a_t^2 = 10$, $a_b^2 = 0.1$; c) $a_t^2 = 0.1$, $a_b^2 = 10$; d) $a_t^2 = 10$, $a_b^2 = 10$.

The predictions are markedly different for the profiles of g'_u in the unforced chamber. When a_t is small, the steady state buoyant layer in the unforced chamber is relatively shallow, while the steady state value of $\overline{g'_f}$ is relatively large. Therefore small quantities of fluid with relatively rapidly varying reduced gravity are deposited in the unforced chamber. This variation leads to a strongly stratified final steady state in the unforced chamber. At steady state the unforced chamber has no vertical motion (unlike the forced chamber) and so nonzero values of $\partial\rho/\partial z$ are not inconsistent with $\partial\rho/\partial t = 0$ in (4.6). Indeed, although their structure is somewhat more complicated for larger values of a_t and a_b, (associated with the non-trivial variation with time of the flow rates through the openings) all the profiles of g'_u appear to exhibit strong vertical stratification for all times.

The time scale of convergence towards steady state is the filling box time scale T_f for the two chamber system as defined in (4.19). Therefore, in circumstances where the cross-sectional area of the unforced chamber is substantially larger than that of the forced chamber (i.e. $A_f \ll A_u$ as defined in figure 4.1) the approach to steady state of the forced chamber is substantially delayed by the presence of the large, yet finite unforced chamber. This phenomenon of delayed convergence may have relevance in real buildings, where smaller chambers (e.g. offices, shops) are connected to larger atria. The character of the steady state in the unforced chamber is typically stratified, and depends strongly on the time-dependent evolution of the flow. Particularly when the upper opening 't' is relatively large, the unforced chamber's buoyant layer is deeper at steady state than the buoyant layer in the forced chamber.

Indeed, large area openings connecting an unoccupied atrium to a forced chamber lead inevitably to extensive contamination of the unoccupied atrium. Our models predict that this behaviour occurs even when the exterior openings are designed to be of an adequate size for the buoyant layer in the forced chamber to be shallow, and the atrium has a relatively large cross-sectional area. This counter-intuitive behaviour appears to be due to the fact that the stratified buoyant layer

in the unforced chamber is constituted of fluid from the buoyant layer in the forced chamber from different stages of the forced chamber's development. Subsequent use or occupation of the unforced chamber would then have to cope with this prior contamination by buoyant fluid from the forced chamber. For the buoyant fluid from the forced chamber to be flushed from the unforced chamber, it is essential for the openings to the exterior to be sufficiently large compared to the upper opening between the two chambers. This naturally involves a trade off, as such a design will inevitably lead to a deeper buoyant layer in the forced chamber. It thus appears sensible to avoid large disparity in the effective area $A_\star$ of the exterior openings and the upper interconnecting opening 't' to optimize the depth of each space which is not contaminated by buoyant fluid.

4.6 Laboratory experiments

To identify which of the numerical models we have discussed better predicts a real physical system, we have conducted a sequence of eight laboratory experiments. As is conventional, the experiments were conducted in an inverted geometry and used a descending saline plume. The experimental apparatus consisted of a perspex tank of internal dimensions 91.6 cm $\times$ 30.5 cm $\times$ 31.1 cm. A thin internal partition divided the tank such that $a_u = \frac{1}{2}$ or $a_u = 2$. This internal partition contained a series of 2.54 cm diameter openings along its top and bottom. The chambers could also communicate with the external reservoir fluid through openings drilled along the tank's upper and lower surfaces. For simplicity, we considered circumstances where the external and internal partition openings were equal in size.

We chose $A_\star$ to vary from 6.08 cm^2 to 18.3 cm^2. The applicable nondimensional parameters for the eight experiments are presented in table 1, where $a_t = a_b = a_p$. The chambers were suspended in a much larger reservoir (237.5 cm by 115.6 cm by 118.7 cm). This reservoir tank was filled to a depth of approxi-

Table 4.1: Experimental parameter values.

Experiment	h_l	a_p	a_u	h_v	$h_{f\infty}$	$h_{of\infty}$	$h_{su\infty}$	$h_{mu\infty}$	$h_{ou\infty}$
A	0.52	1	0.5	0.078	0.49	0.49	0.50	0.66	0.52
B	0.57	1	0.5	0.078	0.53	0.54	0.56	0.69	0.57
C	0.61	1	0.5	0.080	0.57	0.58	0.61	0.72	0.62
D	0.65	1	0.5	0.078	0.61	0.58	0.65	0.74	0.66
E	0.52	1	2	0.079	0.49	0.53	0.56	0.66	0.57
F	0.61	1	2	0.079	0.57	0.53	0.65	0.72	0.56
G	0.65	0.17	0.5	0.079	0.40	0.32	0.95	0.97	0.77
H	0.57	1.5	0.5	0.083	0.55	0.58	0.48	0.63	0.48

mately 110 cm and the experimental tank was positioned such that its top surface was approximately 11 cm below the free interface. This top surface was fitted with a nozzle through which a saline solution was injected. The solution was itself fed from a constant pressure head overhead tank. Flow rates were controlled via a quarter-turn valve and measured using a rotameter. Red food colouring was added to the saline solution for the purposes of flow visualization.

For the experiments reported upon here, the source volume flux, Q_s ranged from 1.8 to 1.9 cm^3/s and the source buoyancy flux, B_s, ranged from 80 $\mathrm{cm}^4/\mathrm{s}^3$ to 91 $\mathrm{cm}^4/\mathrm{s}^3$. The nozzle design (due to Dr. Paul Cooper, see Hunt & Linden [41] for a more detailed discussion of the design) minimized the vertical adjustment length over which the flow became fully turbulent. We corrected for the 'effective origin' h_v (see Caulfield & Woods [18]), defined as

$$h_v \equiv \left(\frac{Q_s^2}{\lambda^3 G_s' H^5} \right)^{1/5}. \tag{4.35}$$

The effective origin h_v (also listed in table 1) defines the distance below the source over which a point source plume, with the same buoyancy flux as the source would have to rise to have the same volume flux as the source volume flux. We have verified that, due to the small value of the source volume flux, more sophisticated corrections (e.g. the asymptotic "virtual origin" correction suggested by Hunt & Kaye [40]) or the results of a full calculation, considering the source volume flux

and momentum flux explicitly, (as discussed in Woods *et al.* [97] for the single chamber flow) lead to variations in predictions of interface height well within the range of experimental error.

Before a regular filling-box flow was established, a transient 'slumping' phase was encountered whereby the discharged plume fluid 'slosh[ed] up the side-walls of the box' (Kaye & Hunt [45]) then subsequently collapsed into a layer of approximately uniform thickness (Hunt *et al.* [39]). Ambient fluid was entrained directly into this contaminated layer. The initial density of this contaminated layer was smaller than that anticipated from the S-S model equations of section 4.4, which assume that a filling-box flow was established instantaneously. Whereas some fraction of this contaminated fluid was quickly re-entrained into the plume, the remaining portion was advected into the unforced chamber where it was either discharged through the external opening or accumulated in the expanding layer of dense fluid. Some non-trivial 'imprint' of this initial transient mixing was thus maintained in the unforced chamber, even in the long-time limit $t \to \infty$, which should lead to a divergence from the predictions of the stratified S-S model. Eventually a filling-box flow was observed, and the flow approached steady state on the expected time scale T_f.

We measured the steady state interface locations in each chamber, which we determine using the 'maximum gradient' method of Kaye & Hunt [45]. In table 1, we list both the measured and the predicted steady state locations for the interfaces in both the forced and unforced chamber for the eight different experiments. The predicted steady state of the interface in the forced chamber $h_{f\infty}$ can be compared with the equivalent value of h_l (defined in (4.8) for a single chamber flow) and the observed interface location (adjusted with the effective origin) $h_{of\infty}$.

As expected, the presence of the unforced chamber reduces the height of the interface above the source. This effect is most marked in the case of experiment 'G', when a_t is relatively small, and so the pressure loss through opening 't' is most

significant, as $a_\dagger$ is dominated by a_t. In general, the S-S model accurately predicts the interface location in the forced chamber. The rms error between the observed measurements and the predictions of the S-S model is approximately 30% of the rms error between the observed measurements and the predictions of the single chamber model, and so it appears possible to identify the effect of the unforced chamber quantitatively. (The well-mixed M-M model predicts the same interface location as the S-S model.)

In table 1, we also list the steady state interface height in the unforced chamber predicted by the stratified S-S model $h_{su\infty}$, the interface height predicted by the well-mixed M-M model $h_{mu\infty}$, and the observed interface height (adjusted with the effective origin) $h_{ou\infty}$. In general, the stratified S-S model predicts the ultimate interface height much more accurately than the well-mixed M-M model, although for experiment 'G', both models significantly under-estimate the observed depth of the buoyant layer in the unforced chamber. This mismatch occurs when the openings in the interconnecting partition are relatively small compared to the openings to the exterior, and the unforced chamber is relatively small compared to the forced chamber. The smaller interconnecting opening leads to a relatively high velocity through the opening 't' into the unforced chamber, and since the chamber has a small cross-sectional area, this relatively high velocity fluid is likely to lead to some overturning.

Nevertheless, the stratified S-S model is a much better predictor of the actual interface location, with the rms error between the experimental observations and the predictions of the S-S model being approximately 50% of the rms error between the experimental observations and the predictions of the well-mixed M-M model. The M-M model always predicts that the buoyant layer in the unforced chamber is shallower than the buoyant layer in the forced chamber, and the experimental evidence shows that this is an unjustified assumption. The evidence points strongly towards the requirement that, in general, the buoyant layer in the unforced chamber is stratified. For example, in experiment 'H', where the intercon-

necting openings were relatively large, the buoyant layer in the unforced chamber is both predicted by the S-S model and observed experimentally to be deeper than the buoyant layer in the forced chamber. Therefore, for the flow between interconnected chambers over a wide range of parameter values, the buoyant layer depth in the unforced chamber is well-predicted by the full transient S-S model.

4.7 Conclusions

We have considered both the transient and steady state flows which can develop in two interconnected chambers of the geometry shown in figure 4.1. The steady state flow in the 'forced' chamber (containing an isolated point source of buoyancy flux) depends not only on the single chamber effective area $A_\star$ (defined in (4.5)) combining the lower exterior inflow opening 'i' in the forced chamber (with area A_i) and the upper exterior outflow opening in the unforced chamber (with area A_o) but also the top opening 't' in the interconnecting partition (with area A_t). The effect of the pressure drop associated with the flow through opening 't' is to reduce the apparent effective area of the openings to $A_\dagger \leq A_\star$, (and thus to increase the depth of the steady state buoyant layer) compared to a single chamber flow with the same external openings, as considered in LLS90 (c.f. (4.15) and (4.5)). Convergence towards this steady state occurs on the filling box time scale T_f for the two chamber system as defined in (4.19).

Although the steady state in the forced chamber is well-mixed, and has no dependence on the previous time evolution of the flow, the steady state in the unforced chamber is typically stratified, and depends strongly on the time-dependent evolution of the flow towards its final steady state, as well as the areas of all the openings and the cross-sectional areas of the two chambers. This is a qualitatively different behaviour from that which is predicted by a model that assumes that the fluid in each chamber is always well-mixed. Such well-mixed models predict that the buoyant layer in the unforced chamber is always shallower

than the buoyant layer in the forced chamber. However, evidence from analogue laboratory experiments supports the assumption that it is essential to track the evolving stratification in the unforced chamber if the steady state layer depth is to be predicted correctly, capturing well a situation where the unforced chamber's buoyant layer depth is actually deeper than the forced chamber's buoyant layer depth, which is well-predicted by a stratified model.

Of course, the flow considered here is extremely idealized. For example, we make the strong simplifying assumptions that the forced plume is a source of buoyancy alone, that the flow through the various openings is unidirectional for all time, and that the two chambers are initially filled with ambient fluid. Also, we assume that the openings are of infinitesimal vertical depth, which is clearly impossible for the interior openings. Therefore, there will inevitably be a pressure variation across the opening, and it is more appropriate to consider the pressure at the midpoint of the opening (see Hunt & Linden 2001 for a more detailed discussion). Indeed, it is much more likely that either exchange flows (as considered in Phillips & Woods [68]) or reversing flows (due perhaps to source volume flux associated with forced air heating or air conditioning systems, as discussed by Woods *et al.* [97]) may occur at different stages of the flow evolution, and that there is at least some buoyant fluid in either or both chambers initially.

Such contamination at the start of the flow evolution and variation in source conditions qualitatively modifies the ultimate steady state in the unforced room, due to complex interactions between the associated draining flows, blocking flows and filling box flows associated with the plume in the forced chamber. In all probability, interactions of these kinds modify the paths connecting initial states to ultimate steady states and it is necessary to consider the dynamical effects of these interactions if we aim to develop a more complete understanding of real ventilation flows in multi-chamber buildings.

4.8 Appendix A: Flow through opening 'b' for the S-S model

Considering the flows into the unforced chamber, if the flow remains stratified in the unforced chamber,

$$\begin{aligned} \frac{\mathrm{d}}{\mathrm{d}t}I_u &= G'_f(H)(Q_t - Q_o) \text{ if } Q_t \geq Q_o, \\ &= -G'_u(H)(Q_o - Q_t) \text{ if } Q_t < Q_o, \end{aligned} \tag{4.36}$$

where $G'_f(H)$ and $G'_u(H)$ are the reduced gravities at the top of the forced and unforced chambers respectively. I_u increases if and only if $Q_b < 0$, and the depth of the buoyant layer in the unforced chamber increases. At least initially, $Q_t > Q_o$. Therefore, $Q_b < 0$, which implies that $P_u(0) > P_f(0)$, and so (4.16) applies. It is thus impossible for I_u to exceed $A_\dagger^2 I_f$, its steady state value, and so as claimed in section 4.4.2, I_u approaches its steady state value from below. If $I_u > A_\dagger^2 I_f$, $Q_t < Q_o$, and so I_u would have to decrease. This argument applies for all values of $I_u > A_\dagger^2 I_f$, thus implying that there is no possible time evolution by which I_u could grow transiently larger than $A_\dagger^2 I_f$ while still being required to approach this value at steady state.

4.9 Appendix B: Flow through opening 'b' for the M-M model

If the flow is assumed to be well-mixed in the unforced chamber, the appropriate equation for the evolution of the buoyancy integral I_u becomes

$$\frac{\mathrm{d}}{\mathrm{d}t}I_u = G'_f(H)Q_t - G'_u Q_o, \tag{4.37}$$

where $G'_f(H)$ is the reduced gravity at the top of the forced chamber, and G'_u is the (well-mixed) reduced gravity of the unforced chamber. Provided $G'_f(H)$ is sufficiently large compared to G'_u, it is entirely possible for I_u to increase when $Q_t < Q_o$, at least initially, and hence the argument presented in Appendix A does

not apply. Therefore, it is possible for the buoyancy integral I_u to be sufficiently large for the pressure $P_f(0)$ in the forced chamber at $Z = 0$ to be greater than the pressure $P_u(0)$ in the unforced chamber at $Z = 0$, and so the flow Q_b through opening 'b' is positive (i.e. from the forced to the unforced chamber) and is given by

$$Q_b = A_b \left(\frac{2}{\rho_e} [P_f(0) - P_u(0)] \right)^{1/2} = A_b \left[\frac{Q_t^2}{A_t^2} - 2(I_f - I_u) \right]^{1/2}, \tag{4.38}$$

using (4.10). Using this expression, rather than (4.16), the system is now closed, and using the same nondimensionalization and approach as in the main body of the text, the flow q_o must satisfy

$$\begin{aligned} q_o^2 &= \frac{i_u}{\mu^2} + \frac{[1 + 2(a_t^2 - a_b^2)][1 + 2a_t^2][{a_\dagger}^2 i_f - i_u] - 4a_b^2 i_u}{\mu^2[1 + 4(a_b^2 + a_t^2) + 4(a_b^2 - a_t^2)^2]} \\ &\quad + \frac{[16a_b^4 i_u^2 + 16a_b^2(1 + 2a_t^2)({a_\dagger}^2 i_f - i_u)(a_b^2 i_u - a_t^2 i_f)]^{1/2}}{\mu^2[1 + 4(a_b^2 + a_t^2) + 4(a_b^2 - a_t^2)^2]}. \end{aligned} \tag{4.39}$$

All the other volume fluxes can be determined from (4.22). Using (4.38), it is possible to establish that the requirement that $q_o > q_t$ implies that

$$i_u \geq \mu^2 q_o^2 \geq {a_\dagger}^2 i_f, \tag{4.40}$$

and so ${a_\dagger}^2 i_f - i_u \leq 0$ in this circumstance.

Material drawn from this chapter has been published by the *Journal of Fluid Mechanics*, 2006, Flynn, M. R. and C. P. Caulfield, **564**, pp. 139–158 (Cambridge University Press).

5

Multi-chamber ventilation (non-ideal source)

5.1 Abstract

Low-energy 'natural' ventilation offers an environmental benefit over building ventilation by high-consumption mechanical systems. However, multi-chamber design often requires a detailed understanding of the flow's time history, particularly when the thermal forcing is by a finite volume flux source. In this case, theoretical models show that two distinct steady states may be achieved: a ventilated flow regime with inflow of ambient fluid at low-levels/outflow of buoyant fluid at high-levels; and a blocked flow regime with outflow of buoyant fluid across the entire chamber height. Notwithstanding the distinction between these disparate final states, ventilation flows may also exhibit 'transient blocking' by which buoyant fluid is discharged at low-levels for finite time only. For multi-chamber geometries, such transient flows are shown to have a non-trivial impact on the properties of the eventual (ventilated) steady state.

5.2 Introduction

Indoor air quality is a critical component of maximizing occupant comfort in modern buildings. Although air exchange with the external environment may be forced using mechanical equipment, alternative low-energy systems are also available, which rely upon freely accessible resources (*e.g.* wind forcing, internal heat gains) to provide the motive force for fluid flow. 'Natural' ventilation is particularly advantageous in temperate climates where internal vertical variations of buoyancy may be exploited in waste heat disposal. Thus each chambers' working space is comprised of a layer of relatively cool ambient fluid supplied by inflow through low-level openings. By contrast, along the ceiling is a layer of hot fluid, which is supplied by internal thermal source(s) and flows out to the environment through high-level openings (Linden [53]).

Previous theoretical analyses of displacement ventilation have considered the flow behavior of both one- (Linden, Lane-Serff & Smeed [55], Gladstone & Woods [33], Kaye & Hunt [45]) and two-chamber (Flynn & Caulfield [27]) geometries. In the latter investigation, it is assumed that only one of the chambers is thermally-forced yet both chambers may communicate with the external environment. In general, the unforced chamber buoyant layer exhibits a continuous variation of density, the details of which cannot be determined from the source conditions alone. Rather, the transient approach towards steady state must be considered. Nonetheless, if the thermal source supplies heat but no mass to its surroundings, the system must evolve towards a ventilated terminal state in which there is outflow of buoyant fluid (inflow of ambient fluid) at high- (low-) level. Here, we explore the qualitatively disparate final steady states which may arise in inter-connected chambers when the plume origin is a source of both heat *and* mass. This builds on the work of Woods, Caulfield & Phillips [97] who showed that a single chamber forced by a finite volume flux source of buoyant fluid and containing low- and high-level openings exhibits two distinct steady states. If the source volume flux, Q_s, is sufficiently small, the

flow evolves to a generalization of the displacement-ventilated state, albeit with a thicker buoyant layer for a prescribed buoyancy flux, B_s. For Q_s sufficiently large, however,

$$Q_s^3 > 2A_U^2\, B_s\, H\,, \tag{5.1}$$

where H is the chamber height and A_U is the effective area of the upper opening. In this circumstance, the steady flow is 'blocked' because the buoyant layer completely fills the chamber, and there is outflow of buoyant fluid through upper and lower openings.

With reference to a generic two-chamber geometry, we examine how the presence of the unforced chamber may alter (5.1) and hence the selection of these qualitatively different steady states. More critically, a novel scenario is examined in which steady, displacement-ventilated conditions are accessed from a transient blocked regime whereby buoyant fluid is discharged at low-level for finite time only. This phenomenon is related to the time-dependent 'overshoot' of interface height that has been documented in the case of single chamber flow by Kaye & Hunt [45]. It arises due to a disparity of time scales over which the buoyant layer temperature and volume approach their respective steady values. Hence, a delicate distinction is drawn between transient and terminal blocking. The latter depends only on the geometry of the forced chamber and is realized when a simple relation similar to (5.1) is satisfied. Conversely, transient blocking depends upon the geometries of both chambers, and indeed its occurrence may only be predicted numerically. Once transient blocking occurs, however, the approach towards (and therefore, properties of) the terminal state is demonstrably altered.

5.3 Model description

Figure 5.1 shows the two-chamber system under investigation. The left-hand forced chamber contains a plume source at floor level ($z = 0$). Communication with the external ambient fluid is established through floor and ceiling-level

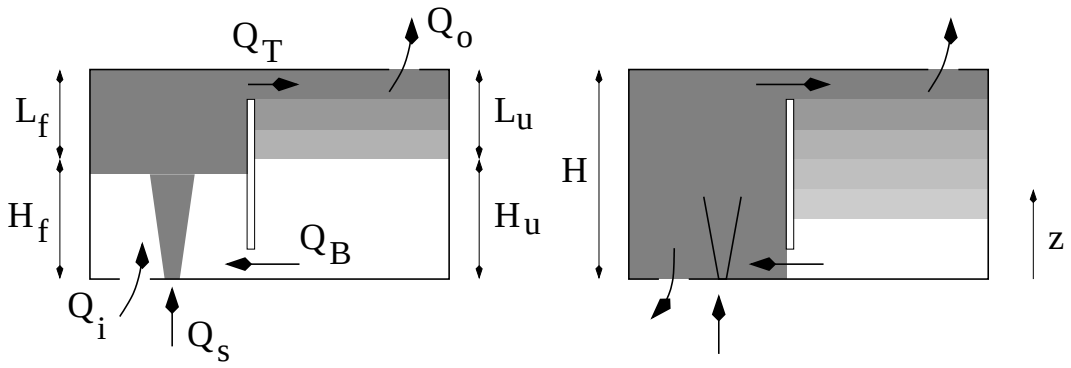

Figure 5.1: Illustration of the (a) displacement-ventilated and (b) blocked states. In both flow regimes, $Q_B \to 0$ as steady-state is approached. Thus, in the blocked terminal state, $H_f = H_u = 0$, *i.e.* both chambers are completely filled with contaminated source fluid.

openings in the forced and unforced chambers, respectively. For simplicity, the effective area of all openings including those along the interior wall common to both chambers we assume to be a constant, A. Furthermore, the interior openings are assumed to be of negligible height compared to the chamber height, H. The fluid is incompressible, inviscid and Boussinesq and the plume is sufficiently narrow in horizontal extent so that it may be considered isolated. Letting S_f and S_u denote, respectively, the plan areas of the forced and unforced chambers, it is assumed that $S_f \lesssim S_u$ while Q_s is sufficiently small such that the buoyant layer in the forced chamber can be approximated as well-mixed for all time (Flynn & Caulfield [27]). This temporally-varying fluid (of depth L_f) is supplied to the unforced chamber by flow through the upper internal opening. Therefore, $\rho_f(t, z > H_f) = \rho_u(t, H)$ where ρ_f and ρ_u denote, respectively, the densities of the buoyant layer in the forced and unforced chambers and H_f is the forced chamber interface height. The vertical density gradient of the unforced chamber is described by the downward advection of isopycnal surfaces as the buoyant, upper layer increases in thickness.

The volumetric flow rates Q_T, Q_B, Q_i and Q_o are as indicated in figure 5.1a. Although Q_T and Q_o are unidirectional, Q_B and Q_i may change sign during the

system's transient evolution. Moreover, both terminal states are characterized by the condition $Q_B = 0$.

5.4 Theory

For illustrative purposes, we assume that pure plume balance is satisfied over $0 < z < H$. Hence the plume volume flux, Q_p, varies with the vertical coordinate z according to

$$Q_p(z) = \lambda\, B_s^{1/3}\,(z + z_s)^{5/3}\,, \qquad \lambda = \frac{6\,\alpha}{5}\left(\frac{9\,\alpha}{10}\right)^{1/3}\pi^{2/3}\,. \tag{5.2}$$

Here, $\alpha \simeq 0.083$ is the entrainment constant appropriate for two-chamber ventilation flow (Lin & Linden [52]) whereas z_s is the effective origin correction defined by Caulfield & Woods [18]

$$z_s = \left(\frac{Q_s}{\lambda\, B_s^{1/3}}\right)^{3/5}\,. \tag{5.3}$$

Clearly, z_s depends upon the relative source strength, which can be evaluated by comparing Q_s against the characteristic ventilation flow rate Q_v, where

$$Q_v = A^{2/3}\, B_s^{1/3}\, H^{1/3}\,. \tag{5.4}$$

When $Q_s < Q_v$, the flow is buoyancy-dominated and a displacement ventilation regime must be realized in the long-time limit. Conversely, when $Q_s > Q_v$, the flow is principally governed by source effects and a (stable) blocked regime is anticipated with outflow through both exterior openings.

The total buoyancy of the forced and unforced chambers are defined, respectively, by

$$I_f = \frac{g}{\rho_a}\int_{H_f}^{H}[\rho_a - \rho_f(z)]\,\mathrm{d}z, \qquad I_u = \frac{g}{\rho_a}\int_{H_u}^{H}[\rho_a - \rho_u(z)]\,\mathrm{d}z\,, \tag{5.5}$$

in which g is gravitational acceleration and ρ_a is the density of the external ambient. Because the forced chamber buoyant layer can be approximated as being spatially-uniform for all time, t, (5.5)a shows that

$$I_f = g'_f\,(H - H_f) = g'_f\,L_f\,, \qquad\qquad g'_f = g\left(\frac{\rho_a - \rho_f}{\rho_a}\right)\,.$$

Conversely, because buoyant fluid from the unforced chamber cannot be entrained into the plume, the unforced chamber buoyant layer (of depth L_u) exhibits a continuous vertical variation of density for $t \to \infty$. Consistent with these observations, mass and buoyancy conservation may be expressed as

$$\frac{\mathrm{d}i_f}{\mathrm{d}\widehat{t}} = 1 - q_T \frac{i_f}{l_f}\,, \qquad \frac{\mathrm{d}i_u}{\mathrm{d}\widehat{t}} = -q_B \frac{S_f}{S_u}\frac{i_f}{l_f}\,, \tag{5.6}$$

$$\frac{\mathrm{d}l_f}{\mathrm{d}\widehat{t}} = \frac{q_s}{\zeta_s^{5/3}}\left(1 - l_f + \zeta_s\right)^{5/3} - q_T\,, \qquad \frac{\mathrm{d}l_u}{\mathrm{d}\widehat{t}} = -\frac{S_f}{S_u}\,q_B\,, \tag{5.7}$$

in which $\zeta_s \equiv z_s/H$, $l_f \equiv L_f/H$, $l_u \equiv L_u/H$ and $\widehat{t} \equiv t/t_D$ where the forced chamber draining time, t_D, is given by

$$t_D = \frac{S_f\,H}{Q_v} = \frac{S_f\,H^{2/3}}{A^{2/3}\,B_s^{1/3}}\,. \tag{5.8}$$

Furthermore, i_f and i_u are defined by

$$i_{f,\,u} \equiv I_{f,\,u}\left(\frac{A}{B_s\,H}\right)^{2/3}\,, \tag{5.9}$$

whereas $q_s \equiv Q_s/Q_v$, $q_T \equiv Q_T/Q_v$ and $q_B \equiv Q_B/Q_v$. These non-dimensional volume fluxes may be expressed in terms of $q_o \equiv Q_o/Q_v$ using volume balance and Bernoulli's equation, which indicate

$$q_T = q_o - q_B\,, \tag{5.10}$$

$$|q_B| = |2(i_f - i_u) - q_T^2|^{1/2}\,, \tag{5.11}$$

$$|q_i| = |q_T^2 + q_o^2 - 2i_f|^{1/2}\,, \tag{5.12}$$

where

$$q_i \equiv Q_i/Q_v = q_s - q_o\,. \tag{5.13}$$

Eliminating q_i, q_T and q_B from these expressions yields a quartic polynomial for q_o, which depends on the direction of flow through the lower internal and external openings (table 5.1).

To resolve the transient approach towards steady state, (5.6) and (5.7) are solved

using the characteristic polynomials of table 5.1 with the initial conditions $i_f = i_u = l_f = l_u = 0$. As $\widehat{t} \to \infty$, blocked conditions will be observed in the long time limit if $q_s > 1$. Conversely, the flow will be ventilated if $q_s < 1$ with the non-dimensional forced chamber interface height, $h_{f\infty} = 1 - l_{f\infty}$, given by

$$\frac{2\zeta_s^5}{q_s^3}(1 - h_{f\infty}) = (h_{f\infty} + \zeta_s)^{5/3}[3(h_{f\infty} + \zeta_s)^{10/3} - 2\zeta_s^{5/3}(h_{f\infty} + \zeta_s)^{5/3} + \zeta_s^{10/3}] \quad (5.14)$$

(c.f. (4.7) of Woods *et al.* [97]). Due to the 'overshoot' of interface height remarked upon earlier, $h_{f,min} < h_{f\infty}$. If $h_{f,min} = 0$ but $h_{f\infty} > 0$, transient blocking must occur during the approach towards steady state. Thus there are two typically distinct time scales of flow evolution. If transient blocking occurs, it will do so when $\widehat{t} \sim \mathcal{O}(\widehat{t_F})$, in which

$$\widehat{t_F} \equiv \frac{t_F}{t_D} = \left(\frac{A}{\lambda^{3/2} H^2}\right)^{2/3} = \frac{\zeta_s^{5/3}}{q_s} \quad (5.15)$$

is the non-dimensional filling-box time scale identified by Baines & Turner [5]. By contrast, for sufficiently large source volume fluxes, ultimate steady states are approached on time scales of the order of the non-dimensional replacement time for both chambers, $\widehat{t_R}$, where

$$\widehat{t_R} \equiv \frac{t_R}{t_D} = \frac{1}{q_s}\left(1 + \frac{S_u}{S_f}\right). \quad (5.16)$$

For many situations of practical relevance, $\widehat{t_F} \ll 1$ whereas $\widehat{t_R} \gg 1$.

5.5 Results

Model results for $\widehat{t} \to \infty$ and $S_f = S_u$ are summarized in figure 5.2, which delineates between blocked ($q_s > 1$) and displacement-ventilated ($q_s < 1$) terminal states. In the latter case, curves of constant $l_{f\infty}$ are shown by the thin solid lines, which indicate that for fixed ζ_s, $l_{f\infty}$ increases with q_s. The dash-dotted lines show the curves $l_{f\infty}/l_{u\infty} = 1.4$, 1.5 and 1.6 which give the relative depth of the buoyant layers at steady state.

Table 5.1: Characteristic polynomials for q_o. Here $q_b > 0$ indicates a flow from the forced chamber to the unforced chamber whereas $q_i > 0$ indicates an outflow through the lower external opening.

Flow regime	Characteristic polynomial
$q_B > 0,\ q_i > 0$	$0 = \frac{1}{4}\, q_o^4 + 2 q_s\, q_o^3 - q_o^2\, [q_s^2 + i_f] + i_f^2$
$q_B < 0,\ q_i > 0$	$0 = \frac{1}{4}\, q_o^4 + q_o^2\, [4 q_s^2 + i_u - i_f] - 4 q_s\, q_o\, [q_s^2 + i_f + i_u] + [q_s^2 + i_f + i_u]^2$
$q_B < 0,\ q_i < 0$	$0 = \frac{17}{4}\, q_o^4 - 8 q_s\, q_o^3 + q_o^2\, [8 q_s^2 - 5 i_f - 3 i_u] - 4 q_s\, q_o\, [q_s^2 - i_f - i_u] + [q_s^2 - i_f - i_u]^2$
$q_B > 0,\ q_i < 0$	$0 = \frac{9}{4}\, q_o^4 - 2 q_s\, q_o^3 + q_o^2\, [q_s^2 - i_f - i_u] + [i_f - i_u]^2$

Within the displacement-ventilated regime, transient blocking is predicted at all points to the left of the thick solid line. As expected, $l_{f\infty}$ is relatively large in this region of parameter space, and so little overshoot is required to cause transient outflow through the lower external opening. This transient flow does not alter the properties of the forced chamber at steady state, which may be determined directly from the source conditions – see *e.g.* (5.14). However, the impact of transient blocking with respect to the properties of *unforced* chamber is striking. Thus, from figure 5.2, the curve labeled '$l_{f\infty}/l_{u\infty} = 1.4$' displays a pair of pronounced 'kinks' where it intersects with the thick solid curve. Transient blocking results in an abrupt adjustment to the flow's temporal trajectory because buoyant fluid is now withdrawn from openings distributed across different heights. Once this occurs, a smaller fraction of buoyant fluid is available to collect along the ceiling of the unforced chamber and thus $l_{u\infty}$ is correspondingly reduced.

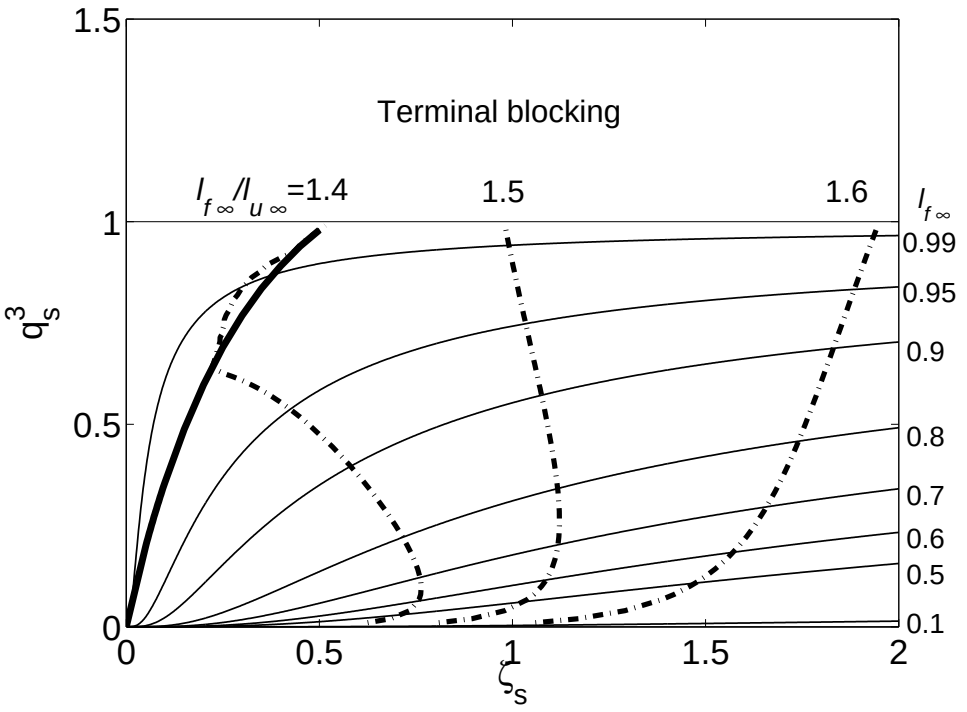

Figure 5.2: Ventilation flow regimes as a function of $q_s \equiv Q_s/Q_v$ and $\zeta_s \equiv z_s/H$.

5.6 Conclusions

To resolve fully the steady state properties of a multi-chamber ventilation flow, the system's time evolution must be examined with a particular focus on the number/size/vertical location of openings through which buoyant fluid may flow into the external environment. Because the forced chamber buoyant layer will always 'overshoot' its steady state depth, a transient outflow of buoyant fluid from the forced chamber must occur anytime an exterior opening is located between the minimum and terminal interface heights. The approach towards steady state is notably perturbed if such a transient outflow is realized. This is manifested by depressed values for the buoyant layer depth in the unforced chamber(s).

Material drawn from this chapter will be included as an extended abstract in the proceedings of the 6^{th} *International Symposium on Stratified Flows*, 2006, Flynn, M. R. and C. P. Caulfield (International Association of Hydraulic Engineering and Research).

6

Intrusive gravity currents – overview

Gravity currents may be defined as the horizontal, boundary flows that arise from density differences between immiscible or partially-miscible fluids. As documented by Simpson [82], many examples of gravity currents may be drawn from the natural environment. These include snow avalanches, which represent a particular danger to skiers and mountaineers, sea breeze fronts, which are responsible for transporting pollution far inland away from coastal areas and thunderstorm outflows, whose intense turbulence has resulted in numerous airplane crashes (Linden & Simpson [56]). Gravity currents also play an important role in estuarial exchange processes. Under appropriate conditions (i.e. small tidal stream velocities and large river output), a pronounced two-layer stratification may develop near river outflows, as illustrated schematically in figure 6.1. Thus, relatively fresh water may be transported along the surface of the ocean whereas a gravity current in the form of a "salt wedge" travels upstream along the river bed. The surface contact line, or front, between these disparate water masses is a zone of local convergence that may be demarcated by small marine biota or other floating debris (see for example figure 7.7 of Simpson [82]).

Analogous mechanisms apply to the ventilation of fjords, which are typi-

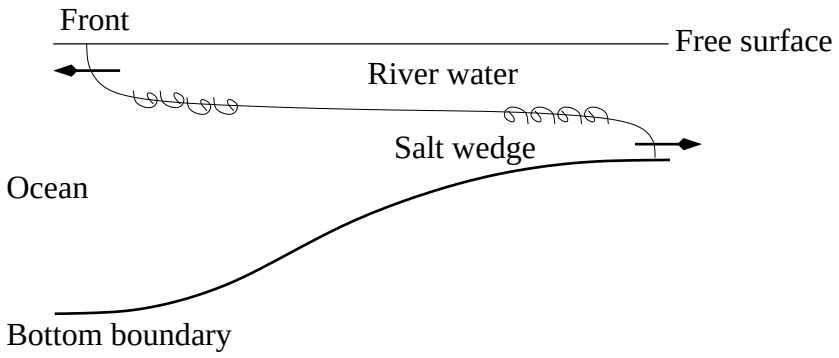

Figure 6.1: Estuarial transport by light and dense gravity currents. After figure 7.5 of Simpson [82]

cally connected to the ocean through shallow sills. However, as shown in figure 6.2 and described in detail by Simpson [82], a more gradual vertical density profile is often encountered in this particular marine environment. Thus, although the exchange flow immediately downstream (i.e. to the left) of the sill is similar to the free-surface gravity current depicted in figure 6.1, important differences appear upstream of this topographic extremum. In particular, as the gravity current of salty, ocean fluid descends down the slope, it vigorously entrains brackish water thereby reducing the density disparity between the gravity current and its surroundings. For slow flows with small inertia, the gravity current is expected to detach from the lower (solid) boundary once its density matches that of the local ambient. Thereafter, the gravity current propagates *inside* the fluid along a particular isopycnal surface. Flows of this type are commonly referred to as intrusive gravity currents or intrusions and may be noted in many other natural settings, as for example with *high-level* thunderstorm outflows, which are associated with the formation of anvil clouds. Moreover intrusions of polluted air are observed when the buoyant effluent from a tall smokestack encounters an atmospheric inversion, across which a rapid vertical variation of density is observed. Similar observations often apply in the study of volcanic eruptions, albeit with the added complication of particle/ash deposition (Huppert [43], [44]).

As the preceding examples illustrate, we may distinguish between two

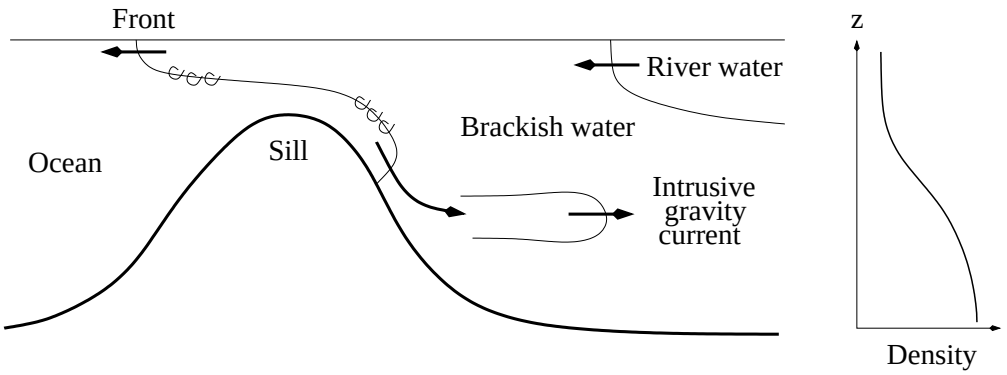

Figure 6.2: Exchange flows within fjords. A representative vertical density profile is shown at right. After figure 7.10 of Simpson [82]

different types of intrusions: those that propagate within a continuously stratified media (Schooley [79], Wu [99], Schooley & Hughes [80], Manins [63], Amen & Maxworthy [1], Rooij [23]), and those that travel along the interface between upper and lower layers of approximately uniform density (Holyer & Huppert [37], Britter & Simpson [16], Faust & Plate [26], D'Alessio *et al.* [22], Mehta, Sutherland & Kyba [65], Lowe, Linden & Rottman [60], Sutherland, Kyba & Flynn [88]). Of particular interest here are intrusions of the latter category, theoretical descriptions of which often stress a topological similarity to the gravity currents described by Benjamin [7] (see also von Kármán [95]). However, we hope to demonstrate that this association is not, in general, exact. Thus substantial modifications to Benjamin's analysis may be required, for example to account for upstream interfacial wave excitation (Chapter 7) or non-standard initial conditions (Chapter 8).

In both Chapters 7 and 8, model results are compared against analogue numerical simulations and laboratory experiments. Although the associated time and length scales are significantly smaller than those appropriate to most natural flows of interest, meaningful insights may nonetheless be drawn from simulations/experiments provided the Reynolds number is sufficiently large such that viscous effects do not exert a leading order influence. Indeed, this modeling approach has been successfully applied in many previous studies (Linden [54]).

7

Intrusive gravity currents (full-depth)

7.1 Abstract

The speed of a fluid intrusion propagating along a sharp density interface is predicted using conservation of mass, momentum and energy. For the special case in which the intrusion density equals the depth-weighted mean density of the upper and lower layers, the theory of Holyer & Huppert [37] predicts that the intrusion occupies one-half the total depth, its speed is one-half the interfacial long wave speed and the interface ahead of the intrusion remains undisturbed. For all other intrusion densities, the interface is deflected vertically by a wave that travels ahead of the intrusion and thereby changes the local upstream conditions. Unless the upper- or lower-layer depth is very shallow, the horizontal extent of the wave is much larger than its vertical extent. In these cases, the conservation equations can be matched to an exact solution of the two-layer shallow water equations, which describe the evolution of the (nonlinear) long wave. We obtain predictions for the intrusion speed that match closely to experiments and numerical simulations, and with a global energy balance analysis by Cheong, Keunen & Linden [20]. Since the latter does not explicitly include the energetics of the upstream wave, it is inferred

that the energy carried by the long wave is a small fraction of the intrusion energy. However, the new more detailed model also shows that the kinematic influence of the upstream wave in changing the level of the interface is a critical component of the flow that has previously been ignored.

7.2 Introduction

The oceans and atmosphere exhibit regions of rapid vertical density variation, such as the thermocline and tropopause. Consequently, horizontal, density-driven flow along a sharp interface arises in a variety of natural settings (Simpson [83]). Such flows are commonly referred to as interfacial gravity currents or intrusions and have been the subject of extensive experimental investigations (Britter & Simpson [16], Mehta, Sutherland & Kyba [65], Lowe, Linden & Rottman [60], Sutherland, Kyba & Flynn [88], Cheong, Kuenen & Linden [20]). Each of these studies examines high-Reynolds number intrusions generated by lock releases – fluid of density ρ_i intermediate to that of the two layers is initially separated by a vertical lock gate. The intrusion is initiated by removing the gate vertically. We are concerned with the case where the motion is independent of the lock length and hence the intrusion dynamics are not influenced by finite-volume effects. It is observed that, consistent with dimensional analysis, the propagation speed, U, is a constant which depends upon ρ_i and the layer depths and densities. Deceleration will be observed only when the flow becomes self-similar, which occurs once reflected disturbances from the end wall overtake the intrusion head (Rottman & Simpson [76], Bonnecaze, Huppert & Lister [15]).

A theoretical description of intrusions that satisfactorily predicts U over a broad range of parameter space remains incomplete. In particular, complications arise when describing *non-equilibrium* flow for which the intrusion density, ρ_i, differs from the depth-weighted mean density, ρ_E, of the upper and lower layers. Energy arguments in the spirit of Yih [100] suggest that the available potential

energy of an equilibrium intrusion is a global minimum and consequently $U > U_E$ when $\rho_i \neq \rho_E$. More specifically, a quadratic departure from the equilibrium solution is predicted, which shows favorable agreement with related experiments and (2D) direct numerical simulations (Cheong *et al.* [20]). However, this energy-conserving approach is based on the assumption that the leading-order behavior of non-equilibrium intrusions may be recovered by judicious interpolation of three well-known flows, namely heavy and light gravity currents and the equilibrium intrusion. Therefore, although the assumptions applied by Cheong *et al.* [20] provide a model in good agreement with experiments, they remain to be justified by a more rigorous examination of non-equilibrium flow that includes some quantitative description of the various forces at play.

The foundations of such an analysis were established in the earlier work of Holyer & Huppert [37] who extended the gravity-current study of Benjamin [7] by considering mass, momentum and energy conservation in a control volume moving with the intrusion head. In the equilibrium case, Holyer & Huppert's analysis accurately predicts the intrusion speed, U. However, when $\rho_i \neq \rho_E$, there are significant discrepancies between the predicted and observed speeds (Sutherland *et al.* [88]). These discrepancies are due to the observed upstream deflection of the interface that is caused by a wave propagating ahead of the intrusion. Although Holyer & Huppert [37] considered the possibility of downstream wave propagation (i.e. a stationary wave train behind the intrusion head), this upstream deflection is not properly accounted for in their theory. Consequently in many circumstances, the upstream conditions assumed in their calculations do not apply. Here we model this upstream deflection explicitly by assuming that the interfacial wave is long. From experimental images of the flow, this assumption is justified unless the interface is very close to either the upper or lower boundary. Estimates for the non-equilibrium intrusion speed are thereby determined, which apply over a broad range of parameter space. Whereas the outcome of this analysis produces results similar to those of Cheong *et al.* [20], these approaches are nonetheless

fundamentally distinct as the latter is a simple energy balance in the spirit of Yih's calculation for a gravity current produced by lock exchange i.e. entirely different balances are applied in deriving the respective governing equations.

The paper is organized as follows: we briefly review Holyer & Huppert's analysis in § 7.3 and equilibrium intrusions in § 7.4. Non-equilibrium intrusions including the effect of the nonlinear upstream wave are discussed in § 7.5 and the results are compared with experiments and two-dimensional numerical calculations in § 7.6. The conclusions are given in § 7.7.

7.3 Holyer & Huppert's theory

We consider an intrusion of density ρ_i propagating at constant speed U along an interface between upper and lower layers of respective depths H_U and H_L. Upstream and downstream of the intrusion front, the flow is assumed horizontal such that the pressure p is hydrostatic. Therefore, along the vertical segment BC

$$p = \begin{cases} p_Q - g\,\rho_U\,z, & 0 < z < H_U, \\ p_Q - g\,\rho_L\,z, & -H_L < z < 0, \end{cases} \tag{7.1}$$

where ρ_U and ρ_L are, respectively, the densities of the upper and lower layers, g denotes gravitational acceleration, $z = 0$ corresponds to the height of the interface and p_Q is the pressure along the interface far upstream from the intrusion (figure 7.1). Similarly, along AD

$$p = \begin{cases} p_R - g\,\rho_i\,h_U - g\,\rho_U\,(z - h_U), & h_U < z < H_U, \\ p_R - g\,\rho_i\,z, & 0 < z < h_U, \\ p_R - g\,\rho_i\,z, & -h_L < z < 0, \\ p_R + g\,\rho_i\,h_L - g\,\rho_L\,(z + h_L), & -H_L < z < -h_L, \end{cases} \tag{7.2}$$

where h_U and h_L represent the vertical distances shown in figure 7.1. In this frame, all the fluid inside the intrusion is at rest (cf. Lowe, Linden & Rottman [60]). Hence $p_R = p_O$, the pressure at the stagnation point.

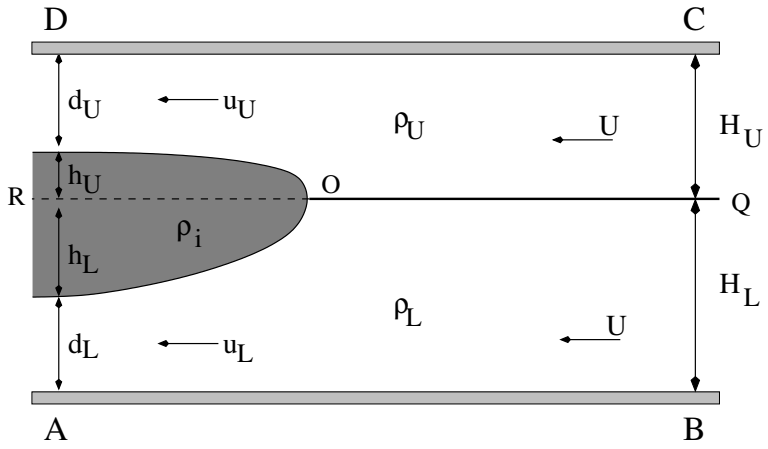

Figure 7.1: Definition sketch of an intrusion (shaded) and the control volume *ABCD*. The frame of reference is chosen so that the intrusion is at rest.

It is assumed that energy is conserved so that Bernoulli's equation may be applied along streamlines in the flow. Therefore, along the lower boundary of the intrusion downstream from the stagnation point[1], we find

$$u_L^2 = 2g'_{Li}\, h_L = 2g'_{Li}\,(H_L - d_L)\,, \tag{7.3}$$

where

$$g'_{Li} \equiv g\,\frac{\rho_L - \rho_i}{\rho_0},$$

is the reduced gravity of the intrusion and the lower layer and ρ_0 is a characteristic density whose precise value is immaterial if the Boussinesq approximation is applied. Similarly,

$$u_U^2 = 2g'_{iU}\, h_U = 2g'_{iU}\,(H_U - d_U)\,, \qquad \text{where} \qquad g'_{iU} \equiv g\,\frac{\rho_i - \rho_U}{\rho_0}\,. \tag{7.4}$$

Here d_U and d_L are the layer depths specified in figure 7.1. Since the layer volume fluxes are constant, these depths are given by

$$d_U = \frac{U\,H_U}{u_U}\,, \qquad d_L = \frac{U\,H_L}{u_L}\,. \tag{7.5}$$

[1]Strictly speaking, the stagnation point is deflected upwards by a distance $\zeta = \frac{U^2}{2g}$ relative to the interface (see (2.24) of Holyer & Huppert [37]). However, this elevation is negligible for most flows of practical interest. Consistent with the Boussinesq approximation and figure 7.1, therefore, we shall assume $\zeta \equiv 0$.

From (7.3), (7.4) and (7.5), conservation of mass therefore requires

$$g'_{iU}\,\frac{(H_U-d_U)\,d_U^2}{H_U^2}=g'_{Li}\,\frac{(H_L-d_L)\,d_L^2}{H_L^2}\,. \tag{7.6}$$

An independent relation for d_U and d_L is obtained via horizontal momentum conservation in the control volume $ABCD$. Because there are no externally-imposed forces,

$$\int_A^D (p+\rho\,u^2)\,\mathrm{d}z=\int_B^C (p+\rho\,u^2)\,\mathrm{d}z\,. \tag{7.7}$$

Using the hydrostatic pressure distributions (7.1) and (7.2) and the layer speeds given by (7.3) and (7.4), we find

$$\begin{aligned}\frac{p_O-p_Q}{\rho_0}\,H=g'_{iU}&\left\{\tfrac{1}{2}(H_U^2-d_U^2)-\frac{2d_U}{H_U}\,(H_U-d_U)^2\right\}\\&+g'_{Li}\left\{\tfrac{1}{2}(H_L^2-d_L^2)-\frac{2d_L}{H_L}\,(H_L-d_L)^2\right\}.\end{aligned} \tag{7.8}$$

Applying Bernoulli's equation upstream along the interface, a second expression for p_O-p_Q is obtained

$$\frac{p_O-p_Q}{\rho_0}\,H=g'_{iU}\frac{d_U^2}{H_U}(H_U-d_U)+g'_{Li}\frac{d_L^2}{H_L}(H_L-d_L)\,. \tag{7.9}$$

Equating (7.8) and (7.9) gives

$$g'_{iU}\frac{(H_U-d_U)^2\,(H_U-2d_U)}{H_U}+g'_{Li}\frac{(H_L-d_L)^2\,(H_L-2d_L)}{H_L}=0\,. \tag{7.10}$$

Equations (7.6) and (7.10) are, respectively, the Boussinesq limits of the mass and momentum conservation equations first derived for arbitrary density differences by Holyer & Huppert [37] and written in this fashion by Sutherland *et al.* [88]. Although both equations are nonlinear in the dependent variables d_U and d_L, substantial simplification is possible for certain special cases, as we demonstrate in the following section.

7.4 Equilibrium intrusions

The easiest circumstance to consider is that of a doubly-symmetric intrusion, for which $H_U=H_L$ and $\rho_i=\frac{1}{2}(\rho_L+\rho_U)$. This intrusion can be considered

as two gravity currents, one above and its mirror image below the interface, traveling at the same speed, U (e.g. figure 7(a) of Lowe *et al.* [60]). In this case, $g'_{Li} = g'_{iU}$ and (7.6) is satisfied by $d_U = d_L = D$, say. Substituting this result in (7.10), we find two solutions $D = \frac{H}{2}$ and $D = \frac{H}{4}$. The first solution corresponds to an intrusion with zero thickness $h \equiv h_U + h_L = 0$, which, as in the bottom-propagating gravity current case, is the energy-conserving intrusion for infinitely deep layers $H_U = H_L \to \infty$. The second solution corresponds to $h = \frac{H}{2}$, and is the energy-conserving half-depth solution described on p. 751 of Holyer and Huppert [37].

This special case can be generalized to other instances in which the intrusion consists of two gravity currents that are, in effect, mirror images of one another. This equilibrium condition is realized whenever the intrusion is neutrally-buoyant with respect to the undisturbed interface such that

$$g'_{iU}\, h_U = g'_{Li}\, h_L \,. \tag{7.11}$$

Equation (7.11) implies that the speeds u_L and u_U are equal. Thus

$$\frac{d_U}{H_U} = \frac{d_L}{H_L} \qquad \Longrightarrow \qquad d_L + d_U = \tfrac{1}{2}\, H \,, \tag{7.12}$$

where conservation of mass and momentum has been applied. Hence an equilibrium intrusion occupies half the channel depth. Further because (7.12) implies $\frac{h_U}{H_U} = \frac{h_L}{H_L}$, the neutral buoyancy condition (7.11) can be written as

$$\rho_i = \rho_E \equiv \frac{\rho_U\, H_U + \rho_L\, H_L}{H} \,. \tag{7.13}$$

Thus when the intrusion density is the depth-weighted mean density ρ_E given by (7.13), a consistent solution to the mass, momentum and energy equations is found in which the interface remains undisturbed ahead of the intrusion (Sutherland *et al.* [88]). Note that (7.13) specifies either the equilibrium intrusion density ρ_E if the layer depths and densities are given or, if the intrusion and both layer densities are given, the equilibrium interface height h_E defined by

$$\frac{h_E}{H} = \frac{g'_{iU}}{g'_{LU}}, \tag{7.14}$$

where $g'_{LU} = g'_{iU} + g'_{Li}$ is the reduced gravity of the interface. Moreover, since $h_L + h_U = \frac{H}{2}$, some simple manipulation shows that

$$h_L = \frac{h_E}{2}\,, \qquad h_U = \frac{H - h_E}{2}\,. \tag{7.15}$$

Finally, the intrusion speed can be determined from (7.3) and (7.5)

$$U_E = \tfrac{1}{2}\sqrt{g'_{LU}\,\frac{h_E\,(H - h_E)}{H}}\,. \tag{7.16}$$

This result is in good agreement with the equilibrium experiments and simulations reported in Cheong *et al.* [20] – see their figure 5. Nonetheless, (7.16) requires substantial modification for the case of non-equilibrium flow for which the stagnation point is deflected vertically by a wave that travels ahead of the intrusion. As we illustrate in § 7.5, this necessitates an explicit coupling of intrusion and wave dynamics.

7.5 Non-equilibrium intrusions

The flow domain is divided into two control volumes as illustrated in figure 7.2. Control volume *ABEF* encompasses the (steady) intrusion, which is assumed stationary relative to the oncoming flow. Conversely, control volume *BCDE* encompasses the nonlinear (long) wave of amplitude d, which propagates upstream at a velocity $c - U > 0$ (in the moving reference frame).

7.5.1 Intrusion

Due to wave-induced shear, the velocities of the upper and lower layers are different and are given, respectively, by $U + w_U$ and $U - w_L$ where w_U and w_L denote perturbations to the uniform upstream flow field considered in § 7.3. This disparity leads to an interfacial deflection $-\xi$ near the stagnation point *O'* where

$$\xi = \frac{(U + w_U)^2 - (U - w_L)^2}{2g'_{LU}}\,. \tag{7.17}$$

Although the flow is Boussinesq, this displacement will be appreciable if $\rho_i \not\approx \rho_E$. In general, therefore, $|\xi| \not\ll h_U$, h_L and by Bernoulli's equation

$$u_U = \sqrt{2g'_{iU}\,(D_U - d_U + \xi)}\,, \qquad u_L = \sqrt{2g'_{Li}\,(D_L - d_L - \xi)}\,, \tag{7.18}$$

where $D_U = H_U - d$ and $D_L = H_L + d$ denote, respectively, the perturbed upper and lower layer depths (figure 7.2). Applying these results in the mass conservation equations for the upper and lower layers yields

$$U + w_U = \frac{d_U}{D_U}\sqrt{2g'_{iU}\,(D_U - d_U + \xi)}\,, \tag{7.19}$$

and

$$U - w_L = \frac{d_L}{D_L}\sqrt{2g'_{Li}\,(D_L - d_L - \xi)}\,, \tag{7.20}$$

respectively. By combining these results with (7.17), ξ can be expressed entirely in terms of the distances d_U, d_L, D_U and D_L and the reduced gravities g'_{iU}, g'_{Li} and g'_{LU}

$$\xi = \frac{\frac{g'_{iU}}{g'_{LU}}\frac{d_U^2}{D_U^2}\,(D_U - d_U) - \frac{g'_{Li}}{g'_{LU}}\frac{d_L^2}{D_L^2}\,(D_L - d_L)}{1 - \frac{g'_{iU}}{g'_{LU}}\frac{d_U^2}{D_U^2} - \frac{g'_{Li}}{g'_{LU}}\frac{d_L^2}{D_L^2}}\,. \tag{7.21}$$

Furthermore, taking the difference between (7.19) and (7.20) and eliminating the wave-induced velocity w_L of the lower layer, yields

$$\frac{w_U\,H}{D_L} = \frac{d_U}{D_U}\sqrt{2g'_{iU}\,(D_U - d_U + \xi)} - \frac{d_L}{D_L}\sqrt{2g'_{Li}\,(D_L - d_L - \xi)}\,. \tag{7.22}$$

As expected from the previous discussion, horizontal momentum is conserved in the control volume $ABEF$ and following the same analysis given in § 7.3,

$$\begin{aligned}\frac{p_O - p_Q}{\rho_0}\,H \;=\;& g'_{iU}\left\{\tfrac{1}{2}\left(D_U^2 - d_U^2\right) - \frac{2d_U}{D_U}(D_U - d_U)^2\left[1 + \frac{\xi}{D_U - d_U}\right]\right\} + \\ & g'_{Li}\left\{\tfrac{1}{2}\left(D_L^2 - d_L^2\right) - \frac{2d_L}{D_L}(D_L - d_L)^2\left[1 - \frac{\xi}{D_L - d_L}\right]\right\}\end{aligned} \tag{7.23}$$

Moreover, the pressure difference $p_O - p_Q$ can again be determined by applying Bernoulli's equation upstream along the interface whereby

$$\frac{p_O - p_Q}{\rho_0} = \frac{g'_{iU}\,g'_{Li}}{g'_{LU}}\left[\frac{d_U^2}{D_U^2}\,(D_U - d_U + \xi) + \frac{d_L^2}{D_L^2}\,(D_L - d_L - \xi)\right] \tag{7.24}$$

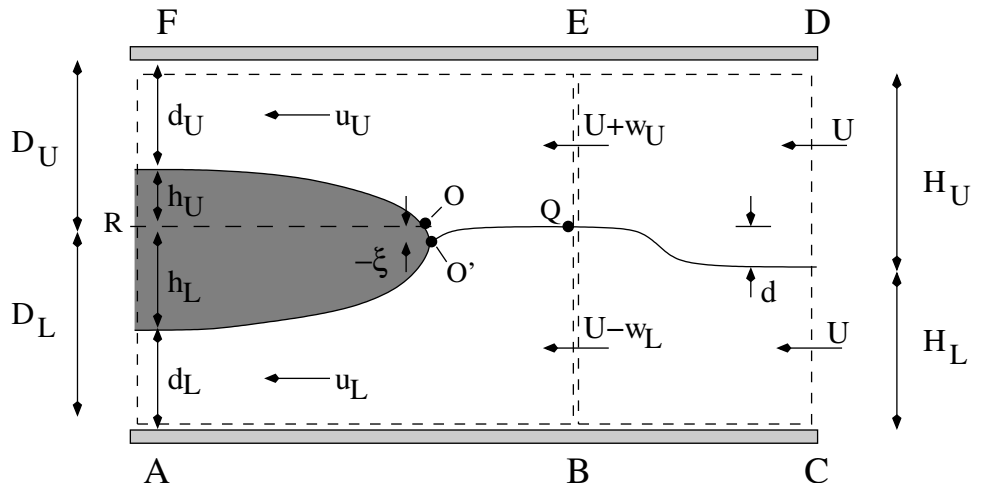

Figure 7.2: Propagation of a non-equilibrium intrusion in two-layer stratified media. For illustrative purposes, the intrusion depicted here has a density ρ_i that is larger than ρ_E, the depth-weighted mean density of the upper and lower layers. Thus the leading wave has positive amplitude, i.e. $d > 0$.

Combining (7.23) and (7.24) yields the momentum balance

$$\frac{H\, g'_{iU}\, g'_{Li}}{g'_{LU}} \left[\frac{d_U^2}{D_U^2} \left(D_U - d_U + \xi\right) + \frac{d_L^2}{D_L^2} \left(D_L - d_L - \xi\right) \right] = g'_{iU} \left\{ \tfrac{1}{2}(D_U^2 - d_U^2) - \frac{2d_U}{D_U} \left(D_U - d_U\right)^2 \left[1 + \frac{\xi}{D_U - d_U} \right] \right\} + g'_{Li} \left\{ \tfrac{1}{2}(D_L^2 - d_L^2) - \frac{2d_L}{D_L} \left(D_L - d_L\right)^2 \left[1 - \frac{\xi}{D_L - d_L} \right] \right\} . \quad (7.25)$$

If the reduced gravities g'_{iU} and g'_{Li} and unperturbed layer depths $H_U = D_U + d$ and $H_L = D_L - d$ are known, (7.21), (7.22) and (7.25) represent three equations in the five unknowns ξ, w_U, d_U, d_L and d. To close the system, we now consider the behaviour of the upstream wave.

7.5.2 Nonlinear wave

The photographs presented in Sutherland *et al.* [88] and Cheong *et al.* [20] suggest that the upstream wave is non-undular and typically has a broad horizontal length scale. Nonetheless, the wave amplitude may be a non-trivial fraction of

either the upper- or lower-layer depth. Motivated by these observations, we adopt a nonlinear dynamical description based on two-layer shallow water theory with a flat bottom boundary. As noted above, this description is appropriate provided H_U, $H_L \not\ll H$. If H_U, $H_L \ll H$, the upstream disturbance may take the form of either a solitary wave or a two-layer bore (see for example Lowe, Rottman & Linden [61] and figure 11 of Sutherland *et al.* [88]). Unfortunately, the energetics of two-layer bores are not fully understood (Baines [4]) and consequently there exists some controversy regarding their appropriate dynamical description. Seeking to avoid such tangential distractions, we will, consistent with figure 7.2, focus on those cases where the interface is neither adjacent to the upper or lower boundaries. Despite the obvious limitations of this approach, the corresponding model equations will be shown to predict the intrusion speed, U, with good accuracy for a broad choice of parameters. This suggests that a long wave description based on two-layer shallow water theory is appropriate to the problem at hand for all but a small range of interface heights.

Long waves are dispersive and travel upstream at roughly twice the intrusion speed. Consequently, long wave propagation is necessarily unsteady with respect to the reference frame of figure 7.2. However, if the intrusion issues from a lock-release apparatus, then the collapse of intermediate density fluid must occur over some finite time period, which depends upon the lock length and the speed of the backward-propagating disturbances. Because *upstream* wave excitation occurs in response to this non-instantaneous gravitational adjustment, it is observed from numerical simulations that the interface is continually deflected in front of the intrusion, so that, following some brief transient, the wave amplitude immediately upstream of the intrusion remains approximately constant in time. Finite volume effects become significant at some point because the center of mass of the intermediate density fluid cannot rise or fall indefinitely. Once the gravitational adjustment ceases, the long wave cannot continue to grow in horizontal extent, except through dispersive effects. Thus the amplitude of the upstream wave in the

immediate neighborhood of the intrusion head may begin to decrease.

Experiments and numerical simulations of intrusive gravity currents are often conducted in channels of restricted spatial dimensions. Often, this precludes a detailed examination of the flow dynamics following the initial collapse of the intermediate density fluid. Consistent with these earlier studies, we shall focus on the inceptive phase of motion where the wave amplitude, d, is approximately constant. Therefore, because the upstream wave is assumed to satisfy the Riemann invariant solution to the two-layer shallow water equations, the analyses of Baines [4] § 3.3 and Appendix D show that

$$\sin^{-1}\left(\frac{D_L - D_U}{H}\right) - \sin^{-1}\left(\frac{w_U\, H}{D_L\,\sqrt{g'_{LU}\, H}}\right) = \sin^{-1}\left(\frac{D_L - D_U - 2d}{H}\right). \quad (7.26)$$

This result relates the long wave amplitude, d, to the wave-induced velocity, w_U, of the upper layer and can be expressed in equivalent algebraic form as follows

$$\begin{aligned}\sqrt{g'_{LU}\, H}\, D_L\,(D_L - D_U - 2d) &= (D_L - D_U)\,\sqrt{g'_{LU}\, H\, D_L^2 - w_U^2\, H^2} \\ &\quad - w_U\, H\,\sqrt{H^2 - (D_L - D_U)^2}\,. \end{aligned} \quad (7.27)$$

In the experiments of Cheong *et al.* [20] the intrusion was generated by releasing intermediate density fluid from a lock by removing a vertical barrier. Consistent with the above discussion, the upstream wave results from the collapse of the intrusion and therefore the amplitude of the long wave can be estimated by considering the vertical adjustment of the intermediate density fluid as it is released from the lock. When ρ_i exceeds the depth-weighted mean density ρ_E, the intrusion will sink relative to the upstream interface and consequently over the time interval Δt, a volume of fluid

$$V = \Lambda\,(h_E - H_L)\,U\,\Delta t \quad (7.28)$$

is added to the lower layer. Here h_E is the equilibrium height defined by (7.14) and Λ is an unknown factor that characterizes the collapse of the intrusion fluid towards its level of neutral buoyancy. If this adjustment is static, $\Lambda = 1$, but we

expect a smaller value because dynamical effects are important. The addition of volume to the lower layer requires the dense fluid ahead of the intrusion to rise by an amount

$$d = \frac{V}{(c-U)\,\Delta t} = \Lambda\,(h_E - H_L)\,\frac{U}{c-U}\,. \tag{7.29}$$

For small d, c is approximately the linear long wave speed and by (7.16), $c \sim 2U$, whereby

$$d \sim \Lambda\,(h_E - H_L) = \Lambda\left(H\,\frac{g'_{iU}}{g'_{LU}} - H_L\right). \tag{7.30}$$

Experiments conducted by Cheong *et al.* [20] confirm the validity of this leading order approximation and give $\Lambda \simeq 0.3$. For this numerical value of Λ, we find an expected symmetry in H_L about $\frac{H_L}{H} = \frac{1}{2}$ when $g'_{iU} = g'_{Li}$, i.e. $\frac{h_E}{H} = \frac{1}{2}$ (see § 7.6). This symmetry is not necessarily reproduced for $\Lambda \not\simeq 0.3$, e.g. $\Lambda = 0.15$ or $\Lambda = 0.5$.

The balances quantified by (7.21), (7.22), (7.25), (7.27) and (7.30) represent a closed system of equations for the unknowns ξ, w_U, d_U, d_L and d. By solving this system of equations, the intrusion speed U may be determined from (7.19).

7.6 Results

The governing equations are nonlinear and therefore multiple solutions are predicted for prescribed conditions. Here, attention is restricted to the solution for which the intrusion volume flux is maximized (Holyer & Huppert [37], Faust & Plate [26]). As with the analysis of Holyer & Huppert [37], this physical solution does not exist in all regions of parameter space. More specifically, model breakdown is likely to be encountered if the leading order balance suggested by (7.30) proves inadequate, i.e. higher order terms in $h_E - H_L$ become significant, or the upstream disturbance takes the form of a solitary wave or bore rather than a long wave. In contrast to earlier studies, however, the system of equations considered here yields a physically-meaningful solution in a relatively broad neighborhood about the equilibrium point $h_E = H_L$. For example, with $\frac{h_E}{H} = 0.5$, (7.21), (7.22), (7.25),

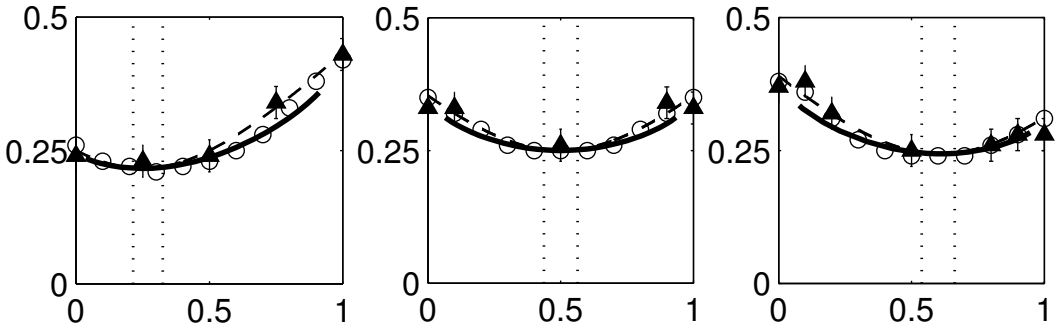

Figure 7.3: Axes: $U/\sqrt{g'_{LU}\,H}$ (vertical), H_L/H (horizontal). Intrusion speed as a function of the interface height for (a) $\frac{h_E}{H} = 0.25$, (b) $\frac{h_E}{H} = 0.50$ and (c) $\frac{h_E}{H} = 0.61$. Data points are taken from Cheong *et al.* [20] and show the results of both experiments (triangles) and numerical simulations (circles). Solid and dashed curves are as indicated in the text. The vertical dotted lines show the range of validity of the model equations with $d \equiv 0$, i.e. a flat upstream interface.

(7.27) and (7.30) admit a physical solution for $\frac{H_L}{H} \simeq 0.0663$ to 0.934. By contrast if the displacement of the upstream interface, d, (and hence the velocities w_U and w_L) are set identically to 0, intrusion properties may be determined only over the restricted range $0.437 \lesssim \frac{H_L}{H} \lesssim 0.564$.

Figure 7.3 shows the intrusion speed (normalized by $\sqrt{g'_{LU}\,H}$) as a function of the non-dimensional interface height, $\frac{H_L}{H}$, for three choices of $\frac{h_E}{H}$. Solutions predicted by the equations of § 7.5 are indicated by the thick solid line. The dashed lines indicate the speeds obtained from the global energy-conserving model described in § 4 of Cheong *et al.* [20], which proposes the following relationship between U, H_L and h_E

$$\frac{U}{\sqrt{g'_{LU}\,H}} = \tfrac{1}{2}\sqrt{\left(\frac{H_L}{H}\right)^2 - \frac{2H_L\,h_E}{H^2} + \frac{h_E}{H}}\,. \tag{7.31}$$

Although this result neglects the kinematic influence of the leading interfacial waves, strong qualitative agreement is observed between (7.31) and the detailed

equations of § 7.5. In particular, both models predict a global minimum of $U = U_E$ when $H_L = h_E$ in which case there is no mass transport across the vertical level $z = H_L$ during the intrusion's gravitational adjustment. By contrast, when $H_L \neq h_E$ (i.e. $\rho_i \neq \rho_E$), intrusion fluid steadily rises or falls behind the intrusion front, which provides an additional source of energy to drive the flow (Cheong *et al.* [20]).

Quantitative differences between the solid and dashed lines of figure 7.3 elucidate the dynamic influence of the interfacial waves, which play a secondary and purely parasitic role. As is clear from figure 7.3a in particular, the lower estimates of the intrusion speed predicted by (7.21), (7.22), (7.25), (7.27) and (7.30) provide a closer fit with the results of the two-dimensional DNS algorithm described in Cheong *et al.* [20]. Consistent with expectations, agreement is particularly strong as $H_L \to h_E$, where the leading order approximation (7.30) is most appropriate.

7.7 Conclusions

A fluid intrusion necessarily excites an upstream interfacial wave when the intrusion density, ρ_i, differs from the depth-weighted mean density, ρ_E, of the upper and lower layers. In general, this disturbance will be nonlinear and will exert some non-trivial dynamical influence in that the wave *(i)* deflects the interface ahead of the intrusion and thereby alters the vertical position of the stagnation point, and, *(ii)* causes a shear so that the local horizontal velocities of the upper and lower layers are non-equal. These effects may be incorporated into existing models by combining exact solutions of the two-layer shallow water equations with mass, momentum and energy conservation applied to a control volume surrounding the intrusion head. The coupled equations, which are given by (7.21), (7.22), (7.25), (7.27) and (7.30), provide good agreement with the results of analogue experiments and numerical simulations for a broad combination of layer depths and densities.

The analytical model developed herein also shows relatively strong agree-

ment with the results of Cheong *et al.* [20]. In contrast to the present discussion, their formulation omits a detailed consideration of the force balance that provides the impetus for motion. Rather, using a Yih-type energy argument, non-equilibrium intrusions are described in terms of related equilibrium flows. The fact that these completely different approaches yield comparable results is encouraging and suggests that the upstream long wave extracts only a small fraction[2] of the intrusion kinetic energy, as has been observed in the case of vertically-propagating internal waves by Ungarish & Huppert [93] and Flynn & Sutherland [29]. This is different, however, from arguing that the interfacial wave has negligible impact. Indeed, as is suggested by figure 7.3, Benjamin-type models that fail to account for the upstream wave-induced effects summarized in the previous paragraph yield physically-relevant solutions only over a limited region of parameter space.

A possible limitation of the above model is its dependence on the empirical parameter Λ, which relates the amplitude of the long wave to the density anomaly of the intrusion through (7.30). Notwithstanding this direct dependence on the flow variables, it appears very difficult to estimate the numerical value of Λ from a first-principles approach. In particular, one cannot simply apply an energy balance in the control volume $BCDE$ because the long wave speed, and hence the upstream energy flux, are not known *a-priori*. This approach is perhaps misguided in any event, because wave forcing is due to the vertical collapse of the intermediate density fluid rather than far-field effects occuring much further upstream.

Nonetheless, it is encouraging that with a single value of Λ, which is independent of the interface height, good agreement between the predicted and measured intrusion speeds may be obtained for a wide class of initial conditions (figure 7.3). Moreover, although the theoretical model shown above applies most directly for full-depth planar intrusions generated by lock-exchange, it may be

[2]For example, based on the maximum difference of intrusion speeds predicted by the solid and dashed curves of figure 7.3, one might estimate a decrease of intrusion kinetic energy of the order of 20%. It should be emphasized, however, that the experimental and numerical data of figure 7.3 typically fall between the solid and dashed curves, and therefore the dynamic impact of the upstream waves is probably a good deal less.

possible to extend this analysis to other closely related flows by simply altering the empirical relationship quantified by (7.30)[3]. Further study is needed to assess the universality of the present approach.

Material drawn from this chapter has been accepted for publication by the *Journal of Fluid Mechanics*, 2006, Flynn, M. R. and P. F. Linden (Cambridge University Press).

[3]Clearly, the discussion of § 7.5 assumes that the intrusion speed, U, is constant. Therefore, it is not immediately obvious whether this methodology can accurate describe axisymmetric intrusions for which the front speed may be a continually-decreasing function of time.

8

Intrusive gravity currents (partial-depth)

8.1 Abstract

Laboratory experiments of intrusive gravity currents generated by lock exchange offer insights into atmospheric and oceanic flows. However, whereas many previous investigations have considered the "full-depth" lock exchange problem, in which the intermediate density fluid initially spans the entire channel depth, less is known about "partial-depth" releases, which represent a more appropriate analogue to environmental flows wherein the inceptive, localized interfacial mixing is relatively weak. Here, we consider this circumstance using a combination of experimental and numerical techniques. Emphasis is placed on the special case where the intrusive gravity current is approximately neutrally-buoyant with respect to the upstream interface. A complementary theoretical model is presented, which predicts the initial speed of propagation of the intrusive gravity current. As with the related analysis of Shin, Dalziel & Linden [81], this model *(i)* allows for communication of momentum and energy between the forward- and backward-propagating disturbances, and, *(ii)* neglects dissipation from viscous effects. Good agreement is observed between the model predictions and the results of experi-

ments and numerical simulations.

8.2 Introduction

A Boussinesq gravity current is defined as a horizontal flow, driven by small density differences, that occurs along a rigid boundary. Just as a gravity current is due to a local concentration or dilution of heat, salt or some other active scalar, an *intrusive* gravity current, or intrusion, may arise from compact mixing across a stable interface, or, in continuously-stratified environments, mixing over some finite depth. Because of the preponderance of convection in the natural environment, intrusions are observed over a range of time and length scales, as summarized by Simpson [83].

Of interest to the present discussion are intrusions that propagate along a sharp interface where the upper and lower layers are of uniform density. A rectilinear geometry of moderate characteristic length is selected (e.g. 10 m to 1 km) so that surface tension and Coriolis effects can be assumed to be small. Most previous studies of intrusions have considered the "full-depth" lock-exchange problem in which the localized mixing is rather severe and, consequently, the intermediate density fluid initially spans the entire vertical extent of the channel, H (Faust & Plate [26]; Lowe, Linden & Rottman [60]; Mehta, Sutherland & Kyba [65]; Sutherland, Kyba & Flynn [88]; Cheong, Kuenen & Linden [20]; Flynn & Linden [28]). Although these analyses examine a useful limiting case, they ignore a wide category of flows for which the initial mixing is relatively weak and/or the layers are relatively deep such that the intermediate density fluid occupies only a fraction of the depth at $t = 0$. We demonstrate that a modified theoretical analysis that considers both sides of the lock release may be applied to this, more general, circumstance. The motivation for this approach comes from the related theoretical and experimental work of Shin, Dalziel & Linden [81], who considered "partial-depth" gravity currents and argued that communication of momentum and energy

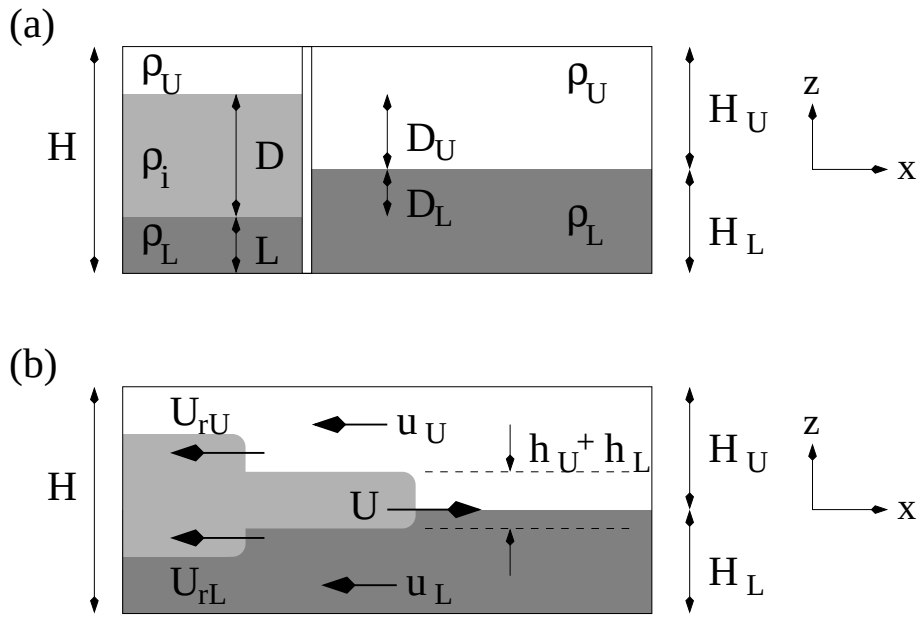

Figure 8.1: Definition sketch of a partial-depth intrusive gravity current at (a) $t = 0$, and, (b) $t > 0$.

between the forward- and backward-propagating disturbances via long waves on the downstream interface must occur whenever the initial depth of heavy fluid is less than $0.76H$. As suggested by figures 16 and 17 of their paper, theoretical models that neglect such an exchange yield predictions that do not always agree with experimental data.

Figure 8.1 shows a schematic illustration of a partial-depth intrusion generated by lock exchange. At the initial instant, $t = 0$, the fluid is stationary. A vertical barrier divides the domain such that there is a two- and three-layer stratification to the right and left of the lock gate, respectively. Once the barrier is removed, fluid of intermediate density ρ_i accelerates from rest and forms an intrusion that propagates to the right along the interface between the upper and lower layers of respective densities ρ_U and ρ_L. As indicated in figure 8.1 b, corresponding backward-propagating disturbances occur on both downstream interfaces. These disturbances take the form of a bore or long wave and ultimately reflect off the left

end wall of the domain. The intrusion speed, U, is expected to remain constant until these reflected disturbances overtake the intrusion front (Rottman & Simpson [76]; Shin *et al.* [81]).

The goal of this analysis is to develop an analytical model that predicts the initial, steady propagation speed for the special case where the intrusion fluid is generated by simple mixing of the upper and lower layers without further dilution or concentration of the active scalar. As suggested by figure 8.1 a, mixing is assumed to occur over a vertical expanse D such that the intermediate density fluid is comprised of upper and lower layer fluid in the ratio $D_U : D_L$. In general, these depths are not equal, i.e. $D_U \neq D_L$. Consistent with the nomenclature applied by Cheong *et al.* [20], the forward-propagating disturbance is referred to as an *equilibrium* intrusion. By contrast, *non-equilibrium* flow is much more difficult to characterize because the center of mass of the intrusion must rise or fall some non-trivial distance once the vertical barrier of figure 8.1 a is removed. This has ramifications for the flow energetics, which, though important, cannot be easily resolved because any gravitational adjustment on the part of the intrusion must excite an interfacial wave that propagates upstream relative to the intrusion front at speed $c > U$. Although the upstream energy flux and hence the wave-induced deceleration are small, the wave deflects the interface vertically and thereby alters the local upstream conditions encountered by the intrusion. As demonstrated by Flynn & Linden [28] for the case full-depth intrusions, this necessitates substantial modifications to the governing equations.

The paper is organized as follows: § 8.3 describes the experimental apparatus used to produce flows of the type illustrated schematically in figure 8.1. Complementary numerical simulations using a spectral-finite difference algorithm were also performed and these are described in § 8.4. Simulation output is shown to reproduce the qualitative and quantitative features of the experimental images in § 8.5. The analytical model is developed in § 8.6 and corresponding results are shown in § 8.7 where a comparison between theory, experiment and numer-

ics is made. Non-equilibrium intrusions are also discussed. Finally, a series of conclusions is presented in § 8.8.

8.3 Experiments

The experimental apparatus and methodology are very similar to those applied in many earlier studies (Faust & Plate [26]; Lowe *et al.* [60]; Mehta *et al.* [65]; Sutherland *et al.* [88]; Cheong *et al.* [20]). Only the essential features will be summarized here.

Experiments were conducted in a tank of size $183\,\mathrm{cm}\times30\,\mathrm{cm}\times23\,\mathrm{cm}$. A vertical barrier was placed 62 cm from the left end wall. To achieve the two- and three-layer stratifications shown schematically in figure 8.1 a, the lock and ambient sides were slowly filled with salt/fresh water to a total depth of $H = 20\,\mathrm{cm}$. As summarized in further detail in § 8.7, experiments applied different combinations of D, L, H_U and H_L, which are defined in figure 8.1 a. Moreover, for a typical experiment, $\rho_L \simeq 1.050\,\mathrm{g/cm^3}$, $\rho_U = 0.998\,\mathrm{g/cm^3}$ and $\rho_L < \rho_i < \rho_U$. Food coloring was added to the intermediate density fluid for the purposes of visualization.

Each experiment began by removing the lock gate vertically. After a brief acceleration phase, steady flows of the type illustrated in figure 8.1 b were observed. Experimental images were recorded using a CCD camera and subsequently analyzed using the image processing software Digiflow (http://www.damtp.cam.ac.uk/lab/digiflow). Horizontal timeseries images were constructed in the manner of Mehta *et al.* [65] from which the front velocity, U, was estimated.

Experimental errors are due primarily to uncertainties in the measured values of D and L, which represent, respectively, the depth of intermediate and large density fluid inside the lock. Although sponge floats were used to minimize interfacial mixing as the tank was filled, interface thicknesses of approximately $0.5-1.0\,\mathrm{cm}$ were nonetheless noted. Furthermore, because the lock gate was pulled up, a small but systematic asymmetry was introduced into the initial conditions.

Specifically, interfaces were deflected upwards slightly at the beginning of each experiment. Although the qualitative impact of this asymmetry was negligible for $D \to H$, it became somewhat more pronounced for $D \lesssim H/2$.

8.4 Numerical simulations

Turbulent gravity currents, whether planar or axisymmetric, intrusive or bottom-propagating, exhibit an irregular topology due to Kelvin-Helmholtz and/or span-wise flow instabilities (see, for example, the photographs presented in Simpson [83] and Neufeld [67]). During the initial slumping phase, however, the speed of propagation is relatively insensitive to the resulting local mixing that occurs behind the gravity current head (Härtel *et al.* [34]; Härtel, Meiburg & Necker [35]). Indeed, because we shall not consider the quantitative details of this mixing, the flow field is resolved using a two-dimensional analysis. Accordingly, for a Boussinesq fluid of uniform viscosity, ν, the governing equations are given by (Kundu [49])

$$\nabla \cdot \mathbf{u} = 0\,, \tag{8.1}$$

$$\frac{\mathrm{D}u}{\mathrm{D}t} = -\frac{1}{\rho_0}\frac{\partial \mathcal{P}}{\partial x} + \nu\,\nabla^2 u\,, \tag{8.2}$$

$$\frac{\mathrm{D}w}{\mathrm{D}t} = -\frac{1}{\rho_0}\frac{\partial \mathcal{P}}{\partial z} - \frac{\rho'\,g}{\rho_0} + \nu\,\nabla^2 w\,, \tag{8.3}$$

$$\frac{\mathrm{D}\rho}{\mathrm{D}t} = \frac{\nu}{\mathrm{Sc}}\,\nabla^2 \rho\,, \tag{8.4}$$

where g is gravitational acceleration, $\mathbf{u} = (u,\, w)$ is the velocity, $\mathcal{P}$ is the hydrostatically adjusted pressure, ρ_0 is a characteristic reference density, Sc is the Schmidt number and $\mathrm{D}(\cdot)/\mathrm{D}t$ denotes a material derivative. Furthermore, $\rho(x,\, z,\, t) = \bar{\rho}(z,\, t) + \rho'(x,\, z,\, t)$ is the fluid density in which $\bar{\rho}$ and ρ' represent, respectively, the background and perturbation components. For the simulations reported here, $\nu = 0.01\,\mathrm{cm}^2/\mathrm{s}$ and $\mathrm{Sc} = 1$. Although the latter choice significantly overestimates the diffusivity of salt water, this selection is necessary for the purposes of numerical

Table 8.1: Numerical simulation parameters.

Simulation type	l (cm)	Λ (cm)	H (cm)	N_x	N_z	τ (s)
Validation	183	62	20	1024	128	16
Flat upstream interface	75 or 150	30	20	512 or 1024	128	10
Perturbed upstream interface	150	30	20	1024	128	10

stability (Maxworthy *et al.* [64]; Ungarish & Huppert [93]). As noted by Sutherland, Flynn & Dohan [87], the magnitude of Sc does not substantially alter the dynamical behavior of the flow.

The above dimensional, primitive variable equations are solved with no-slip boundary conditions using the open-source DNS algorithm Diablo. Consistent with previous analyses such as Sutherland *et al.* [87], a computational domain of size $2l \times H$ is selected where l denotes the horizontal extent of the flow domain shown in figure 8.1. Therefore, by specifying a condition of reflection symmetry about the mid-plane ($x = 0$) in the initial condition, a Fourier decomposition of the flow variables $\mathbf{u}$, ρ and $\mathcal{P}$ may be applied in the streamwise direction (Canuto *et al.* [17]). Conversely, in the wall-normal direction, ρ and $\partial\mathbf{u}/\partial z$ do not satisfy periodic boundary conditions. Thus derivatives with respect to z are evaluated using second-order, centered finite-differences.

A combination of a third-order, low-storage Runge-Kutta-Wray (RKW3) scheme and a Crank-Nicholson (CN) scheme is used to advance the flow in time with $\Delta t = 0.001\,\mathrm{s}$ (Bewley [8]; Bewley, Moin & Temam [9]). Diffusive terms in the wall-normal direction are treated implicitly; all other terms are treated explicitly. Moreover, uniform non-staggered and staggered grids are selected, respectively, in the streamwise and wall-normal directions. Three types of numerical simulations are performed as summarized in table 8.1. First, validation tests are conducted

for comparison against laboratory experiments (§ 8.5). Then investigative simulations are run where the upstream interface remains approximately flat (§ 8.7.1), and, conversely, where the upstream interface is deformed by a propagating wave (§ 8.7.2). Consistent with the above discussion, the flow is in each case resolved over a numerical domain of size

$$\{-l \leq x \leq l\} \bigcup \{-H_L \leq z \leq H_U\}\,,$$

where the intermediate density fluid initially spans

$$\{-\Lambda \leq x \leq \Lambda\} \bigcup \{-D_L \leq z \leq D_U\}\,.$$

Here $z = 0$ corresponds to the level of the upstream interface (figure 8.1), $D_L = H_L - L$, $D_U = D + L - H_L$ and Λ denotes the lock length. Characteristic values for l, Λ and H are provided in table 8.1, which also shows the time interval of integration, τ, and the number of grid points used in the streamwise (x) and wall-normal (z) directions.

As with the analogue laboratory experiments of § 8.3, the flow is stationary at $t = 0$. To ensure that the initial collapse of the intermediate density fluid occurs in a regular and timely fashion, a small, random density perturbation is added to ρ_i. Furthermore, because a Fourier decomposition is applied in the streamwise direction, the vertical interfaces that define the lateral boundaries of the lock are smoothed using a hyperbolic tangent profile. Finally, layer densities are chosen such that

$$\mathrm{Re} \equiv \frac{D(g'_{LU}\, D)^{1/2}}{\nu} \gtrsim 10^4\,, \tag{8.5}$$

in which Re is the Reynolds number and

$$g'_{LU} = g\left(\frac{\rho_L - \rho_U}{\rho_0}\right)$$

is the reduced gravity between the upper and lower layers. With Re so selected, the flow exhibits the characteristic features of two-dimensional turbulent gravity currents such as the roll up of Kelvin-Helmholtz billows behind the gravity current

head (see, for example, figures 3 and 11 of Härtel *et al.* [35], figure 7 of Sutherland *et al.* [87] and figure 2 of Cheong *et al.* [20]).

8.5 Comparison between experiments and numerical simulations

Figure 8.2 shows an example of simulation output in which the initial collapse and subsequent propagation of a volume of intermediate density fluid is illustrated at three instants in time. We find that the initial acceleration phase occurs over a small time interval and that the intrusion speed rapidly approaches the time-independent value U. Corresponding experimental images are presented (in false color) in figure 8.3. Consistent with the discussion of § 8.4 which contrasts two- and three-dimensional flow, the series of coherent, semi-stable Kelvin-Helmholtz billows observed in figure 8.2 are not evident in the laboratory images. Apart from these billows, strong qualitative and quantitative agreement is observed between figures 8.2 and 8.3, suggesting that the numerical algorithm satisfactorily captures the principal components of the intrusion and corresponding return flows.

8.6 Theory

As with their full depth counterparts, partial-depth intrusive gravity currents may be divided into two categories depending upon the relationship between the layer depths and densities in the initial state. An equilibrium flow satisfies

$$\epsilon \equiv \frac{g'_{iU}\, D_U - g'_{Li}\, D_L}{g'_{LU}\, D} = 0\,, \tag{8.6}$$

where $D = D_U + D_L$ and

$$g'_{iU} = g\left(\frac{\rho_i - \rho_U}{\rho_0}\right), \qquad g'_{Li} = g\left(\frac{\rho_L - \rho_i}{\rho_0}\right),$$

are the reduced gravities of the intrusion with respect to the upper and lower layers, respectively.

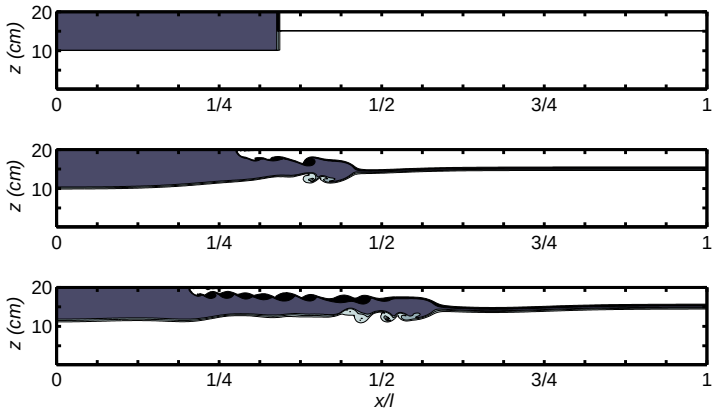

Figure 8.2: Snapshots of the density field for a particular numerical simulation with $(\rho_i - \rho_U)/(\rho_L - \rho_U) = \frac{1}{2}$, $H_U = H/4$, $H_L = 3H/4$, $D = L = H/2$ at (a) $\widehat{t} = 0$, (b) $\widehat{t} = 7.4$, and, (c) $\widehat{t} = 14.8$. The non-dimensional time, $\widehat{t}$, is defined by $\widehat{t} = t\,(g'_{LU}\,D)^{1/2}/D$. Consistent with the data of table 8.1, $l = 183\,\mathrm{cm}$.

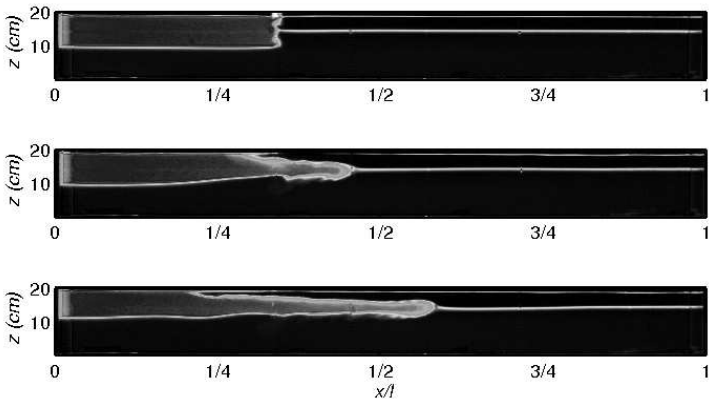

Figure 8.3: Snapshots of the density field from the analogue laboratory experiment. Parameters are the same as in figure 8.2.

Heuristically-speaking, for equilibrium flow, fluid of intermediate density ρ_i is produced simply by localized mixing of the upper and lower layers over the respective depths D_U and D_L, where $D_U \neq D_L$ in general. Conversely, non-equilibrium flow, for which $\epsilon \neq 0$, is associated both with localized mixing *and* dilution ($\epsilon < 0$) or concentration ($\epsilon > 0$) of the intermediate density fluid.[1] The discussion of the present section is restricted to equilibrium flow such that the interface ahead of the intrusion remains approximately flat. To leading order, therefore, the intrusion may be considered to consist of upper and lower gravity currents each of which travels at speed U (cf. Holyer & Huppert [37]). It is assumed that a hydraulic description is appropriate such that the flow in each layer is independent of the vertical coordinate, z. We further assume that the intrusion moves as a plug, i.e. there is no relative motion of intermediate density fluid between the forward- and backward-propagating disturbances (Lowe *et al.* [60]). Moreover, these advancing fronts are assumed to *(i)* travel at constant speed, and, *(ii)* be connected by a horizontal interface. Further upstream and downstream, the flow is assumed quiescent with a hydrostatic vertical pressure gradient. Finally, everywhere within the flow domain, the fluids are assumed to be inviscid, irrotational and immiscible with $\gamma = 0$ where γ is the surface tension.

The above assumptions are consistent with those applied by Shin *et al.* [81] who examined the related problem of partial-depth gravity currents. Therefore, from (5.14) of their work, mass and momentum conservation applied, respectively, to the upper and lower layers require

$$U^2 = \frac{g'_{iU}\, D_U\, (D_U - h_U)\, (H_U - h_U)}{2 h_U\, H_U}\,, \tag{8.7}$$

and

$$U^2 = \frac{g'_{Li}\, D_L\, (D_L - h_L)\, (H_L - h_L)}{2 h_L\, H_L}\,, \tag{8.8}$$

where h_U and h_L are defined in figure 8.1 b. For equilibrium intrusions, however,

[1] A geophysical example of a non-equilibrium intrusion is the high-level outflow from a convective thunderstorm whose buoyancy is determined both by mixing and latent heat effects.

(8.6) shows that $g'_{iU}\, D_U = g'_{Li}\, D_L$ and hence

$$\frac{(D_U - h_U)\,(H_U - h_U)}{h_U\, H_U} = \frac{(D_L - h_L)\,(H_L - h_L)}{h_L\, H_L}\,. \tag{8.9}$$

As demonstrated by Shin *et al.* [81], equations (8.7) and (8.8) are derived by performing an integrated horizontal momentum balance in a control volume that encompasses both the forward- and backward-propagating disturbances. Energy dissipation is neglected in the upper and lower layers. In principle, momentum and energy may be transfered between the forward- and backward-propagating disturbances via waves along the downstream interfaces. As with Yih [100], the present model therefore takes a "global" perspective, which considers both sides of the lock exchange flow. This methodology differs from the classical treatment of Benjamin [7] in which only the forward-propagating disturbance is considered.

Unfortunately, non-local models of the type considered here suffer from two principal shortcomings, as identified by Ungarish [92]. Firstly, backward-propagating disturbance(s) are assumed to take the form of a bore rather than a long wave of expansion. In the case of gravity currents, for example, the laboratory experiments of Rottman & Simpson [76] show that this assumption is strictly valid only for $D/H \gtrsim 0.7$. Also, the derivation of (8.7) and (8.8) assumes that the backward-propagating disturbances have not yet encountered the left end wall of the control volume (figure 8.1 b). As such, these expressions apply only for the period after the removal of the lock gate during which the intrusion travels a horizontal distance of approximately one lock-length. Despite the above limitations, the gravity current model developed by Shin *et al.* [81] shows favorable agreement with experimental data over a broad range of D/H. In addition, it is observed that U is unaltered by the reflection of the backward-propagating disturbance. Therefore, in spite of their possible drawbacks, global models may nonetheless represent a useful predictive tool in describing bulk features of gravity current/intrusion flow.

To close the system of equations developed above, some further statements concerning the flow energetics are required. For intrusions that travel along a free-slip interface, Ermanyuk & Gavrilov [25] note that "... energy losses due to

vorticity generation and mixing at the interface between the [intrusion] and the ambient fluid are far less important than the losses due to bottom friction [associated with gravity current flow]." Moreover, because wave forcing is assumed to be negligible when $\epsilon = 0$, we conclude that energy dissipation may be neglected to leading order. One might therefore expect that the upper and lower flows conserve energy independent of one another such that $h_U = D_U/2$ and $h_L = D_L/2$, i.e. the upstream interface acts as a true solid boundary (Benjamin [7]; Holyer & Huppert [37]). Interestingly, (8.7) and (8.8) then yield consistent results if and only if

$$\frac{D_U}{H_U} = \frac{D_L}{H_L} \iff L = \frac{H_L\,(H - D)}{H}\,, \tag{8.10}$$

where the geometric identity $D_L = H_L - L$ has been employed in deriving the latter expression (figure 8.1 a). Although (8.10) is trivially respected for full depth lock release flows, it is not, in general, valid when $D_U < H_U$ and $D_L < H_L$. We therefore propose that the depths h_U and h_L are determined such that energy is conserved for the *total* flow including the forward- and backward-propagating disturbances in both the upper and lower layers. As summarized by Shin *et al.* [81], changes of kinetic energy are associated with accelerating fluid from rest on either side of the lock. The requisite energy comes from a loss of potential energy due to a reduction in depth of intermediate density fluid from $D = D_U + D_L$ to $h_U + h_L$. Taking these various factors into account and letting Δ_U and Δ_L denote, respectively, the time rate of change of energy of the upper and lower flows, it can be shown that

$$\begin{aligned} \Delta_j \;\; = \;\; & \tfrac{1}{2}\rho_i\,U^2\,(U + U_{rj})\,h_j + \tfrac{1}{2}\rho_j\,u_j^2\,(U + U_{rj})\,(H_j - h_j) \\ & + \tfrac{1}{2}g\,\delta\rho_j\,U\,h_j^2 - \tfrac{1}{2}g\,\delta\rho_j\,U_{rj}\,(D_j^2 - h_j^2)\,, \end{aligned} \tag{8.11}$$

where $j = U$ or L, U_{rj} and u_j denote, respectively, the velocity of the backward-propagating disturbance and ambient layer (figure 8.1 b), and

$$\delta\rho_j = \begin{cases} \rho_i - \rho_U & \text{if } j = U\,, \\ \rho_L - \rho_i & \text{if } j = L\,. \end{cases}$$

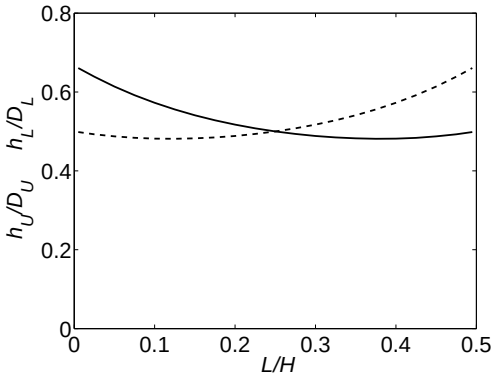

Figure 8.4: Relative depth of penetration into the upper and lower layers as predicted from (8.7), (8.8), (8.9) and (8.13) with $H_U = H_L = D = H/2$. Line types are indicated in the text. Here $L = H_L\,(H - D)/H$ corresponds to $L/H = \frac{1}{4}$.

Thus if

$$0 = \Delta_U + \Delta_L\,,$$

we find

$$\begin{aligned} 0 \;\; = \;\; & \frac{h_U\,D_U}{D_U - h_U}\left[\frac{U^2\,H_U}{H_U - h_U} - g'_{iU}\,(D_U - h_U)\right] \\ & + \frac{h_L\,D_L}{D_L - h_L}\left[\frac{U^2\,H_L}{H_L - h_L} - g'_{Li}\,(D_L - h_L)\right]\,, \end{aligned} \tag{8.12}$$

where mass continuity has been applied in eliminating U_{rU}, U_{rL}, u_U and u_L. Finally, combining this result with (8.7), (8.8) and (8.9) yields

$$h_U + h_L = \frac{D}{2}\,. \tag{8.13}$$

Hence an energy-conserving intrusion occupies one-half the initial depth of the intermediate density fluid, $D = D_U + D_L$.

Assuming the initial state to be well-defined, (8.7), (8.8), (8.9) and (8.13) represent three independent equations in the three unknowns U, h_U and h_L. These governing equations show the appropriate limiting behavior as D_U/H_U, $D_L/H_L \rightarrow$

1 in which case a consistent solution to (8.9) and (8.13) is given by

$$h_U = \tfrac{1}{2} H_U \,, \qquad h_L = \tfrac{1}{2} H_L \,.$$

Therefore, from (8.7) and (8.8),

$$U = \tfrac{1}{2} (g'_{iU}\, H_U)^{1/2} = \tfrac{1}{2} (g'_{Li}\, H_L)^{1/2} \,,$$

which reproduces the (equilibrium) results of Holyer & Huppert [37] who provide a theoretical description of intrusion flow based on the gravity current analysis of Benjamin [7]. For the more general circumstance where $D_U/H_U,\ D_L/H_L \not\to 1$, (8.7), (8.8), (8.9) and (8.13) predict that

$$\frac{h_U}{D_U} > \frac{1}{2} > \frac{h_L}{D_L} \qquad \text{when} \qquad L < \frac{H_L\,(H-D)}{H} \ \text{ i.e. } \ \frac{D_U}{H_U} < \frac{D_L}{H_L} \,, \tag{8.14}$$

$$\frac{h_U}{D_U} < \frac{1}{2} < \frac{h_L}{D_L} \qquad \text{when} \qquad L > \frac{H_L\,(H-D)}{H} \ \text{ i.e. } \ \frac{D_U}{H_U} > \frac{D_L}{H_L} \,. \tag{8.15}$$

This behavior is demonstrated in figure 8.4, which shows h_U/D_U (solid line) and h_L/D_L (dashed line) as functions of L/H for the particular combination $H_U = H_L = D = H/2$.

Equations (8.14) and (8.15) have the following interesting consequence: whereas an intrusion that is exactly neutrally-buoyant with respect to the interface is expected to satisfy $g'_{iU}\, h_U = g'_{Li}\, h_L$, here we find that

$$g'_{iU}\, h_U > g'_{Li}\, h_L \qquad \text{when} \qquad L < \frac{H_L\,(H-D)}{H} \ \text{ i.e. } \ \frac{D_U}{H_U} < \frac{D_L}{H_L} \,, \tag{8.16}$$

$$g'_{iU}\, h_U < g'_{Li}\, h_L \qquad \text{when} \qquad L > \frac{H_L\,(H-D)}{H} \ \text{ i.e. } \ \frac{D_U}{H_U} > \frac{D_L}{H_L} \,. \tag{8.17}$$

In contrast to the full-depth case, therefore, the center of mass of an intrusion issuing from a partial-depth lock release apparatus may rise or fall even though $\epsilon = 0$, where ϵ is the non-dimensional density parameter defined by (8.6). As discussed in § 8.2, this gravitational adjustment necessarily excites an upstream interfacial wave. Although neither of these effects are properly accounted for in the present theory, the magnitude of the vertical adjustment is typically small such

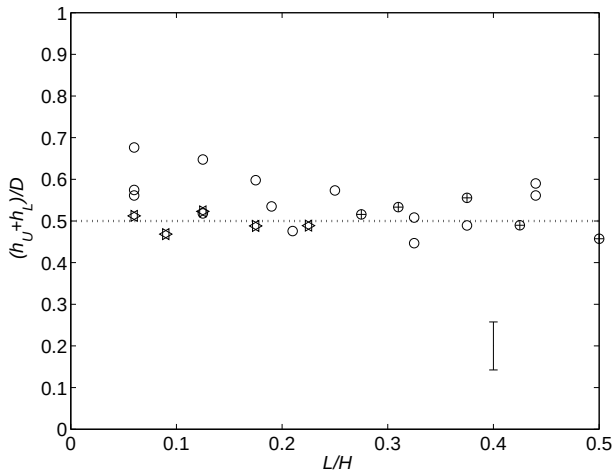

Figure 8.5: Relative intrusion depth, $(h_U + h_L)/D$, as a function of L/H where h_U, h_L, L, H and D are defined in figure 8.1. The dashed line shows the result predicted by (8.13). Data points are derived from laboratory observations with $H_U = H_L = D = H/2$ (open circles), $H_U = H_L = H/2$, $D = 3H/4$ (stars) and $H_U = H/4$, $H_L = 3H/4$, $D = H/2$ (cross-hairs). In each case, $\epsilon = 0$ where ϵ is the non-dimensional density parameter defined by (8.6). A representative error bar is shown in the lower right hand corner.

that the wave amplitude is observed to be no greater than the interfacial thickness (see, for example, figures 8.2 and 8.3). Thus, with $\epsilon = 0$ any deviations from the condition of neutral-buoyancy will not significantly impact the potential energy of the flow. Indeed, as we illustrate in quantitative detail in § 8.7.1, good agreement between theory, experiment and numerics may be obtained even when $g'_{iU}\, h_U$ and $g'_{Li}\, h_L$ are not exactly equal.

8.7 Results

8.7.1 Equilibrium flow

A central feature of the above energy-conserving model is quantified by (8.13), which shows that the intrusion should occupy one-half the initial depth of

the intermediate density fluid. This prediction is tested in figure 8.5, which compares measured values of $h_U + h_L$ against $D = D_U + D_L$ for a variety of laboratory experiments. The relative error of repeated measurements is large in some cases, particularly when $D = H/2$ and $L/H \to 0$. In addition to the random and systematic experimental errors discussed in § 8.3, these deviations may also be due to interfacial mixing, which obscures the exact boundary between adjacent fluid layers. Nonetheless, within the range of the indicated error bar, (8.13) provides an accurate description of the flow in most instances. Similar agreement is noted by Shin *et al.* [81] for the case of gravity currents (see, for example, figure 13 of their paper).

Figure 8.6 shows the measured and predicted speeds of propagation as a function of the non-dimensional vertical location of the intrusion, L/H. Note that the permissible range of L/H differs for different choices of H_U, H_L and D (figure 8.1 a). Theoretical results based on the equations of § 8.6 are given by the thick solid curves, and experimental and numerical results are given, respectively, by the crosses and open circles. Here, U has been non-dimensionalized according to the Froude number, Fr

$$\mathrm{Fr} = \frac{U}{(g'_{LU}\, H)^{1/2}}\,, \tag{8.18}$$

based on the total depth, $H = H_U + H_L$, and interfacial reduced gravity, g'_{LU}. The vertical dotted and dashed lines of figure 8.6 show, respectively, the critical values of L/H

$$L = \frac{H_L\,(H - D)}{H} \qquad \Longrightarrow \qquad \frac{D_U}{H_U} = \frac{D_L}{H_L}\,, \tag{8.19}$$

in which case the interface behaves like a true solid boundary, and

$$L = H_L - \tfrac{1}{2}\,D \qquad \Longrightarrow \qquad D_U = D_L\,, \tag{8.20}$$

in which case the interface will, in general, be deflected vertically by a small amplitude wave (see, for example, figures 8.2 and 8.3). Because $H_U = H_L$ in figures 8.6 a,b, these two lines overlap. Conversely, in figure 8.6 c where $H_U \neq H_L$,

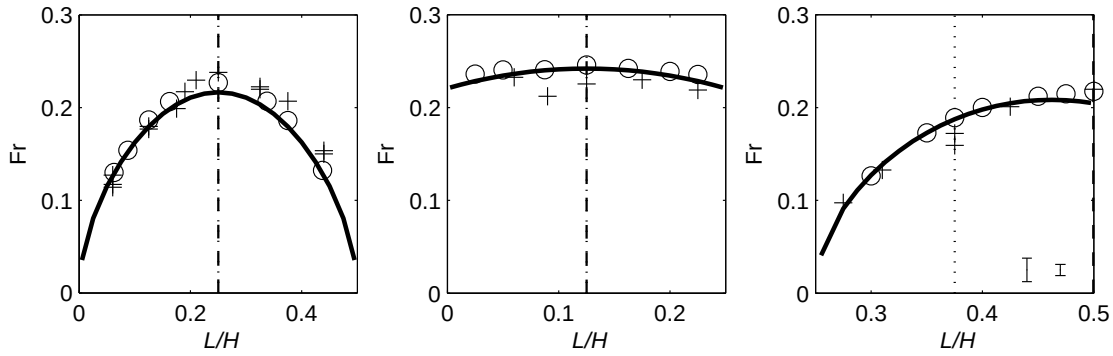

Figure 8.6: Fr versus L/H for $\epsilon = 0$ and three different model geometries: (a) $H_U = H_L = D = H/2$, (b) $H_U = H_L = H/2$, $D = 3H/4$, and, (c) $H_U = H/4$, $H_L = 3H/4$, $D = H/2$. Representative error bars for the experimental (crosses) and numerical (open circles) data are shown, respectively, in the lower right hand corner of (c). Dotted and dashed lines are described in the text.

$D_U = D_L$ when $L/H = 0.5$ and the dashed line coincides with the right hand edge of the domain.

The model equations of § 8.6 predict that Fr (and hence the propagation speed, U) achieves its maximum value when $D_U \simeq D_L$ and therefore, from the definition of ϵ, $\rho_i \simeq \frac{1}{2}(\rho_U + \rho_L)$ (cf. (3.6) of Flynn & Linden [28]). This deduction is supported by the experimental and numerical data of figures 8.6 a,c, which show good agreement with the theoretical curve over a broad range of L/H. Comparable agreement is noted in figure 8.6 b. Here, however, the vertical variation of Fr is small relative to the error bars and thus we cannot estimate with good certainty the measured values of L/H that maximize Fr.

Taken together, figures 8.5 and 8.6 suggest that a global, energy conserving model provides accurate estimates of the leading order behavior exhibited by equilibrium partial-depth intrusions. For reasons described above, however, this analysis cannot be straightforwardly adapted for non-equilibrium flow for which $\epsilon \neq 0$ and the intrusion is not approximately neutrally-buoyant with respect to the upstream interface. As we illustrate in § 8.7.2, this complication greatly restricts

our ability to describe the flow dynamics.

8.7.2 Non-equilibrium flow

Consistent with Yih's study of gravity currents, helpful insights into the speed of non-equilibrium intrusions may be ascertained from rudimentary energy arguments. Consider, for example, the three initial conditions depicted schematically in figure 8.7. Those of figure 8.7 a satisfy $\epsilon = 0$ and therefore, by suitable manipulation of (8.6),

$$H_L(\epsilon = 0) \equiv H_L^\star = L + D\left(\frac{\rho_i - \rho_U}{\rho_L - \rho_U}\right).$$

(It is assumed that $\rho_L < \rho_i < \rho_U$. Hence an equilibrium flow must satisfy $L < H_L < D + L$). By contrast $H_L = L$ and $H_L = D + L$, respectively, in figures 8.7 b,c whence $\epsilon \neq 0$. For these latter two cases, the available potential energy, $\mathcal{E}$, of the initial state may be determined from

$$\frac{2\mathcal{E}_b}{\rho_0} = g'_{iU}\, D^2\,, \qquad \frac{2\mathcal{E}_c}{\rho_0} = g'_{Li}\, D^2\,, \tag{8.21}$$

respectively, where subscripts refer to the appropriate panel of figure 8.7 (see, for example, § 4 of Cheong *et al.* [20]). Conversely, for the equilibrium case shown in figure 8.7 a,

$$\frac{2\mathcal{E}_a}{\rho_0} = \frac{g'_{iU}\, g'_{Li}}{g'_{LU}}\, D^2\,. \tag{8.22}$$

With $\rho_L < \rho_i < \rho_U$, it may be easily verified that $\mathcal{E}_a < \mathcal{E}_b$, $\mathcal{E}_c$.

Extending the above results, we find that for arbitrary H_L with $L \leq H_L \leq D + L$ and H fixed (i.e. variable interface height), the available potential energy is given by

$$\frac{2\mathcal{E}}{\rho_0} = g'_{iU}\, D^2 \left(\frac{g'_{Li}}{g'_{LU}} + \epsilon\right)^2 + g'_{Li}\, D^2 \left(\frac{g'_{iU}}{g'_{LU}} - \epsilon\right)^2. \tag{8.23}$$

This result shows the proper limiting behavior with (8.22) as $\epsilon \to 0$. Furthermore, with ϵ defined by (8.6), (8.23) reduces to (8.21) a,b in the respective limits $D_L \to 0$ ($\epsilon \to g'_{iU}/g'_{LU}$) and $D_U \to 0$ ($\epsilon \to -g'_{Li}/g'_{LU}$). Differentiation of (8.23) holding ρ_U,

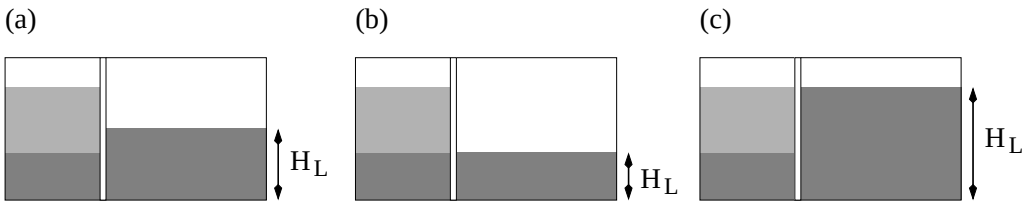

Figure 8.7: Three different initial conditions corresponding to (a) $\epsilon = 0$ with $L < (H_L = H_L^\star) < D + L$ (b) $\epsilon > 0$ with $H_L = L$, and, (c) $\epsilon < 0$ with $H_L = D + L$. Layer densities are assumed to be the same in each case.

ρ_L and ρ_i constant shows that $\mathcal{E}$ is a global minimum when $\epsilon = 0$. Therefore the available potential energy of an equilibrium intrusion is strictly less than that of any corresponding non-equilibrium flow with $H_L \neq H_L^\star \equiv H_L(\epsilon = 0)$. In the spirit of energy conservation, it is reasonable to expect that $U(H_L = H_L^\star) < U(H_L \neq H_L^\star)$ as has been verified for full-depth intrusions by Cheong *et al.* [20].

Notwithstanding the simplicity of the above arguments, which neglect energy losses due to interfacial mixing, upstream wave propagation and other dissipative effects, the results of figure 8.8 suggest that the preceding conclusion is approximately correct. Here, snapshots of the density field are presented at $t = 8\,\mathrm{s}$ ($\widehat{t} \equiv t\,(g'_{LU}\,D)^{1/2}/D = 7.9$) for a particular set of numerical simulations. In all four images $(\rho_i - \rho_U)/(\rho_L - \rho_U) = \frac{1}{4}$, $D = H/2$ and $L = 3H/8$, however, the vertical location of the interface (and consequently H_U and H_L) are different in each case. Thus in figure 8.8 a, $\epsilon > 0$, in figures 8.8 c,d, $\epsilon < 0$ and figure 8.8 b shows the equilibrium intrusion ($\epsilon = 0$). In particular, figures 8.8 a and d correspond, respectively, to the extreme configurations $H_L = L$ (figure 8.7 b) and $H_L = D + L$ (figure 8.7 c). Because $(\rho_i - \rho_U)/(\rho_L - \rho_U) < \frac{1}{2}$, the initial conditions considered here are asymmetric, and consequently we observe little difference between $U(H_L = L)$ and $U(H_L = H_L^\star)$ (figures 8.8 a,b). However, when $H_L > H_L^\star$, observed intrusion speeds are notably larger than $U(H_L = H_L^\star)$. In particular, the intrusion of figure 8.8 d travels more than twice as fast as the equilibrium flow of figure 8.8 b. These findings are consistent with (8.23). For the intrusions depicted,

respectively, in figures 8.8 a,b,c,d, it can be shown that the available potential energy of the initial state scales as $1.\bar{3} : 1 : 1.75 : 4$.

Unfortunately, it is difficult to make more detailed predictions of non-equilibrium flow behavior without developing a comprehensive analytical model that quantifies the gravitational adjustment of the intrusion and the commensurate vertical deflection of the upstream interface. Such a deflection is a prominent feature of the non-equilibrium intrusions illustrated in figures 8.8 a,c, and most especially, d. In general therefore, one must consider both communication between the forward- and backward-propagating disturbances as well as between the forward-propagating disturbance and an upstream interfacial wave. Such possibilities greatly expand the complexity of the balance equations (for example (8.7) and (8.8)) and necessitate substantial modifications to existing analyses which omit one or the other form of communication. Beyond the usual non-trivial algebraic obstacles, this also demands a reconciliation of the different frames of reference which are typically applied in studying either of the constituent problems. In particular, when momentum and energy cannot be transfered between the forward- and backward-propagating disturbances, it is conventional to consider a reference frame moving with the speed of the intrusion, as is done for example in Chapter 7. By contrast, when such exchanges are possible and hence the influence of downstream waves cannot be neglected, it is preferable to work in a stationary reference frame as is done in the present chapter. Further study is needed to determine whether the upstream and downstream problems may be considered separately, or, conversely, whether the entire flow must be examined all at once, most likely within a stationary reference frame.

8.8 Conclusions

We have considered, via experiments and related two-dimensional numerical simulations, the dynamics of "partial-depth" intrusions whose initial non-

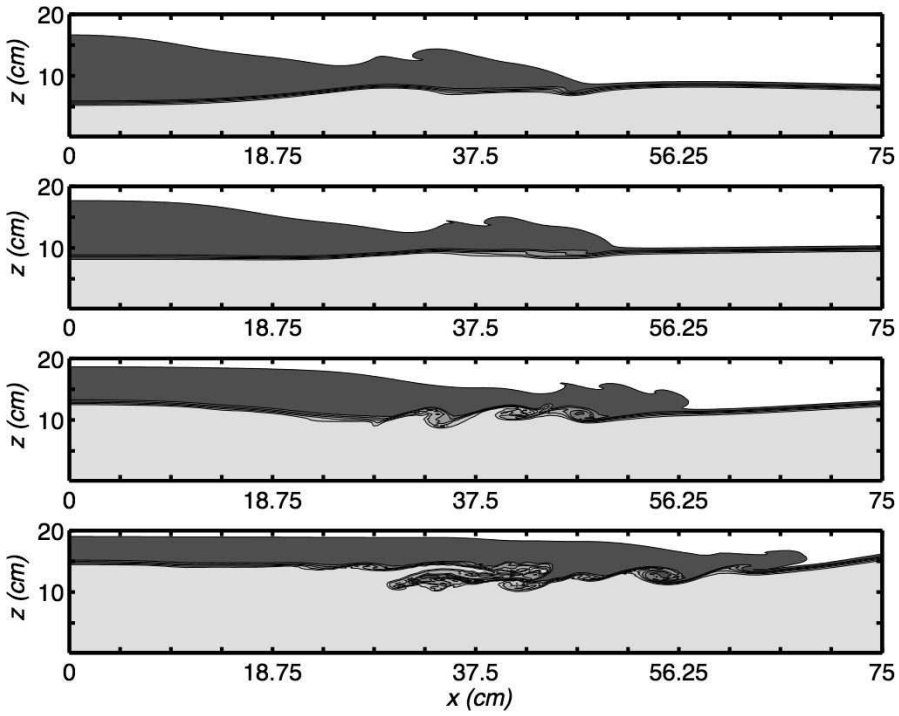

Figure 8.8: Snapshots of the density field for $(\rho_i - \rho_U)/(\rho_L - \rho_U) = \frac{1}{4}$, $D = H/2$, $L = 3H/8$ and (a) $H_L = 3H/8$, $H_U = 5H/8$, $\epsilon = 0.25$, (b) $H_L = H_U = H/2$, $\epsilon = 0$, (c) $H_L = 11H/16$, $H_U = 5H/16$, $\epsilon = -0.375$, (d) $H_L = 7H/8$, $H_U = H/8$, $\epsilon = -0.75$. A reflection symmetry about the interface is not observed for the equilibrium intrusion (b) because $(\rho_i - \rho_U)/(\rho_L - \rho_U) \neq 0.5$. Consistent with the remarks of § 8.4, a (one-sided) lock length of 30 cm is selected in each case. Furthermore, $l = 150$ cm and thus only one quarter of the total (two-sided) horizontal extent is shown.

dimensional depths of penetration into the upper and lower layers are strictly less than unity. An analytical model is also developed, which predicts the time-independent intrusion height, $h_U + h_L$, and speed, U, for the special case of equilibrium flow where $\epsilon = 0$ in which ϵ is the non-dimensional density parameter defined by (8.6). As with the related analysis of Shin *et al.* [81], this model considers both sides of the lock release and, in general, allows momentum and energy to be transfered between the forward- and backward-propagating disturbances. The model further assumes that energy is conserved overall, i.e. dissipative effects due to viscosity are ignored. Good agreement is observed between the theoretical predictions and corresponding experimental and numerical data. Moreover, the data of figure 8.6 suggest that U is maximized when $D_U \simeq D_L$ such that the intrusion density is roughly the arithmetic average density of the upper and lower layers.

For non-equilibrium flow, the center of mass of the intrusion may rise or fall some appreciable vertical distance, which inevitably leads to wave excitation along the upstream interface. As suggested by the related analysis of Flynn & Linden [28], the corresponding flow dynamics are complex and cannot be recovered by a simple extension of the preceding analytical model. Here, we estimate the lower bound of U for non-equilibrium intrusions using rudimentary energy arguments. Deriving more robust quantitative predictions awaits further theoretical developments.

Material drawn from this chapter has been submitted for publication to *Physics of Fluids*, 2006, Flynn, M. R., Boubarne, T. and P. F. Linden (American Physical Society).

9

Conclusions and summary of present contribution

9.1 Natural ventilation

Whereas conventional HVAC systems provide a comfortable indoor climate at a considerable energy expense, "naturally-ventilated" buildings apply freely-available resources such as wind forcing and internal heat gains in place of mechanical equipment such as fans and blowers. In particular, because naturally-ventilated buildings provide cooling only for those regions occupied by people or temperature-sensitive equipment, natural ventilation represents a particularly advantageous strategy with respect to waste heat disposal. Unfortunately, designs that maximize thermodynamic efficiency during summer months often yield inadequate interior conditions during winter months when *(i)* deliberate heat input may be required to supplement that produced by electrical equipment or other machinery, and, *(ii)* infiltration of cold external air is typically undesirable. "Hybrid" buildings are designed specifically for multi-season use and must therefore achieve some reasonable compromise between the disparate demands of passive summer-time cooling and active winter-time heating. The analysis of Chapter 3 explores this topic in detail and shows (at least for simple geometries) how an external wind

forcing that exerts a pressure difference across a building's external shell may be fruitfully harnessed in either circumstance.

An important conclusion from this theoretical development is that hysteresis effects in ventilation flows may be significantly curtailed or eliminated altogether provided the interior thermal source supplies both heat *and* mass to its surroundings. Thus for prescribed source conditions and external forcing, one may identify whether multiple steady flow states will occur, or, conversely whether the ventilated, blocked and well-mixed flow regimes described in Chapter 3 represent unique solutions to the governing equations. Because all possibility of cold air infiltration is arrested only for sufficiently large source volume fluxes, drawing this distinction is a crucial first step in optimizing the cold weather performance of hybrid buildings.

A possible restriction of the preceding analysis is that it considers an idealized geometry, i.e. a single chamber connected to the exterior through floor- and ceiling-level openings (Linden, Lane-Serff & Smeed [55], Rooney & Linden [75], Linden [53], Li & Delsante [50], Hunt & Linden [41], [42], Woods, Caulfield & Phillips [97], Kaye & Hunt [45], Heiselberg *et al.* [36]). Although limited by its simplicity, this configuration offers a number of computational advantages, not the least of which is that a comprehensive description of the steady state may be derived directly from the source conditions and building geometry. No independent consideration of the transient approach towards steady state is required.

The theoretical and experimental discussion of Chapters 4 and 5 shows that this mode of analysis may be inadequate when studying the ventilation characteristics of more intricate (i.e. multi-chamber) geometries. Specifically, areas devoid of direct thermal forcing lack the convective motions necessary to homogenize layers of contaminated source fluid. Thus a continuous vertical stratification of temperature (i.e. density) may be maintained, even in the longtime limit, $t \to \infty$. Consequently, some non-decaying and non-trivial "imprint" of the system's transient evolution is preserved, which depends sensitively upon a number of factors

including the relative size(s) of adjacent chamber(s), the number and position of interior/exterior openings and the possibility that contaminated source fluid might be discharged to the environment from multiple openings for a finite period of time.

The above discussion poses a particular challenge for the design engineer. To wit, although reduced models that universally neglect the internal stratification of contaminated layers are relatively straightforward to implement, they may predict qualitatively incorrect flow behavior. For example, for the geometry illustrated schematically in figure 4.1, the doubly well-mixed model described in Chapter 4 predicts that the forced chamber buoyant layer depth must always exceed the unforced chamber buoyant layer depth. This conjecture is contrary to both the results of a more exhaustive analytical model, and, more importantly, observations derived from complementary laboratory experiments. Therefore, for non-simple building geometries, a detailed analysis of natural ventilation design/performance, particularly with reference to possible steady states, should proceed from a careful examination of the transient flow behavior. Temporal *and* spatial variations of density in the interior environment must be appropriately modeled, for example using the numerical algorithm suggested by Germeles [30].

Similar considerations must also apply to the ventilation of a multi-chamber enclosure in the presence of an external wind shear. However, because the vertical stratification of the unforced chamber is destroyed once wind-dominated, well-mixed conditions are achieved, the system's initial temporal evolution may be of secondary importance in special limiting cases. Needless to say, such considerations are somewhat academic vis-a-vis summer-time design, where waste heat disposal is of central concern such that well-mixed conditions are highly undesirable in any event. As is observed for simple geometries, hysteretic behavior of the type described in Chapter 3 should again be possible provided the source volume flux is sufficiently small. It appears unlikely, however, that a slowly-varying oscillatory wind will result in a chaotic internal response. Rather the multi-chamber system is expected to alternate between well-defined quasi-steady states. Further

study is required to characterize exhaustively these (geometry-dependent) temporal fluctuations.

Even in the absence of an external wind, additional analysis is also needed to properly assess the influence of the initial conditions on the properties of the eventual steady state for multi-chamber flow. Consistent with previous studies (e.g. Lin & Linden [52]), the ventilation models of Chapters 4 and 5 assume that the building is filled entirely with ambient fluid of uniform temperature at $t = 0$. More realistically, the chambers might possess an initial, non-trivial density stratification due, for example, to prior occupation or solar radiation. Although contamination of this type will not alter the system's long time behavior for sufficiently simple (i.e. one chamber) geometries, it remains to identify how a pre-existing density stratification will perturb the selection of, and corresponding approach to, the final steady state in non-trivial flow domains.

Furthermore, there is a poor understanding of the ventilation performance of buildings forced by an oscillatory thermal source, mimicking, for example, a diurnal variation of solar radiation, an electrical appliance such as a refrigerator that cycles on and off, or a lecture theater or meeting room that is used at regular intervals, but not continuously, throughout the day. Thus the period of oscillation represents an additional time scale, whose magnitude relative to the filling, draining and replacement time scales defined in Chapters 4 and 5 should influence the system's transient adjustments. Also, once the thermal forcing is reduced, the plumes generated by isolated heat sources may contain insufficient buoyancy to rise all the way to the top of the chamber. As a result, the plumes will act as fountains once their (height-dependent) density matches that of the external ambient. It has been shown by D. T. Bolster (personal communication) that incorporating into conventional ventilation models the equations of Bloomfield & Kerr [13], [14], which describe the entrainment of buoyant ambient fluid by the fountain is a non-trivial task.

Finally, all of the strategies for natural ventilation described thus far focus

on heat transfer via convection. It may be possible, however, to significantly expand thermodynamic performance by also taking advantage of conductive and/or radiative effects. For example, thermal mass floors and walls trap heat within the building fabric and thereby "phase shift" daytime solar gains. Accordingly, temperatures within the building's interior are respectively lowered and raised during midday and evening. By judiciously integrating this technology with that described in quantitative detail above, it may be possible to extend both the seasonal and geographic ranges over which low-energy building ventilation may be applied.

9.2 Intrusive gravity currents

Diapycnal mixing across a density-stratified interface often results in an intrusive gravity current, which represents an important category of environmental flow. More specifically, whereas interfacial waves transport no mass to leading order, intrusive gravity currents may carry discrete fluid parcels and/or nutrients, sediment, insects, etc. over great distances in nature (see for example Armi [3] and Simpson [83]). Although existing descriptions of intrusive gravity currents, or intrusions, have focused on their similarity to the boundary gravity currents studied by Benjamin [7], we demonstrate herein that a straightforward extension of Benjamin's analysis (i.e. that provided by Holyer & Huppert [37]) is insufficient to provide a satisfactory dynamical description under many instances of practical relevance.

Chapter 7 explores *non-equilibrium* flow for which the intrusion density is different from the depth-weighted mean density of the upper and lower layers. It is well known from the analyses of Sutherland, Kyba & Flynn [88] and Cheong, Kuenen & Linden [20], that upstream interfacial waves must be generated in this circumstance. However, these previous studies do not suggest a theoretical methodology for resolving the waves' quantitative influence. Here, we apply shallow water theory to provide the necessary analytical framework. More specifically, it is as-

sumed that the upstream waves are non-linear and satisfy the Riemann invariant solutions to the two-layer shallow water equations given by Baines [4] (see also Appendix D). Consequently we may relate the wave-induced velocity of the upper and lower layers to the wave amplitude, which is itself dependent on the intrusion's gravitational adjustment with respect to the upstream interface. Application of mass, momentum and energy conservation in a control volume surrounding the intrusion head closes the 5×5 system of non-linear algebraic equations. Of particular interest here is the predicted front speed, U, which is expected to remain constant during the slumping phase of motion (Rottman & Simpson [76]).

The theoretical model described above shows good agreement with complementary experimental and numerical data as reported in Cheong *et al.* [20]. Moreover, model results compare favorably with Cheong *et al.*'s energy-conserving model, which neglects the dynamical effect of upstream propagating interfacial waves. This suggests that the wave energy flux is relatively small compared to the kinetic energy of the bulk flow. Nonetheless, the waves' impact should not be considered irrelevant because they deflect the upstream interface vertically and thereby change the local upstream conditions encountered by the intrusion. Dynamical models that overlook this important fact (for example that of Holyer & Huppert [37]) predict physical solutions of restricted parametric scope.

Chapter 8 considers via experiments and two-dimensional numerics a modified lock-release geometry in which the fluid of intermediate density does not initially span the entire channel depth, H. For mixed layers whose initial depth is small, it is expected from the related analysis of Shin, Dalziel & Linden [81] that momentum and energy may be exchanged between the forward- and backward-propagating disturbances by long waves on the downstream interfaces. Communication of this sort is neglected in the studies of Benjamin [7] and Holyer & Huppert [37], who consider only the forward-propagating flow.

A hydraulic, energy-conserving model is developed for the special circumstance in which the intrusion density matches the system's depth-weighted mean

density. For this particular case, it is helpful to approximate the upstream interface as being exactly horizontal. It must be emphasized, however, that the gravity currents above and below the interface are not independent of one another as they are observed to travel with the same speed, U. This restriction places particular constraints on the relative height of the intrusion with respect to the upper and lower layers. Although the intrusion is predicted to occupy one-half the initial depth of the intermediate density fluid, we find that, in general, $h_U/D_U \neq 1/2$ and $h_L/D_L \neq 1/2$ where h_U, h_L, D_U and D_L are the distances specified in figure 8.1.

Model results show good quantitative agreement with the output from the numerical simulations, which apply a spectral and finite difference decomposition in the streamwise and wall-normal directions, respectively. Agreement with experimental data, though positive, is slightly less robust due to certain systematic asymmetries introduced by the equipment design.

It is much more difficult to describe theoretically non-equilibrium intrusions issuing from a partial-depth lock release apparatus for in this case the intrusions must be matched to wave-perturbed upstream *and* downstream conditions. Whereas a detailed investigation of the corresponding equations is beyond the scope of the present inquiry, helpful information may nonetheless be drawn from rudimentary energy arguments. Though limited in scope, this analysis may provide insights into the development of a more comprehensive theory.

A possible limitation of the analyses of Chapters 7 and 8 is that the lower (rigid) boundary is assumed flat and thus the flow is not influenced by topographic effects. Indeed, it is well-known from the theoretical, numerical and experimental work of Birman *et al.* [10] and others that topography plays an important role in the dynamics of gravity currents that travel along a rigid yet non-uniform boundary. In a similar fashion, topographic forcing should likewise exert some non-trivial role in the motion of intrusive gravity currents. Most importantly, perhaps, with an irregular lower boundary, the flow cannot achieve steady state during the slumping phase of motion because the lower layer depth changes as

a function of the horizontal coordinate and thus there is a local acceleration or deceleration of the mean flow. Therefore, the steady state analysis summarized in Chapters 7 and 8 cannot be applied. Instead, if the topographic slopes are sufficiently small, a more appropriate alternative may be to employ the shallow water formulation of Rottman & Simpson [76] and D'Alessio *et al.* [22] for which unsteady terms in the momentum equation (i.e. $\partial \mathbf{u}/\partial t$) are explicitly retained. Critically, one must then determine a front condition of the type given by (7.7) of Shin *et al.* [81], which accurately describes unsteady gravity current flow over a non-uniform surface.

Topographic forcing will also impact upstream and downstream waves generated by the intrusion. In particular, if the lower layer becomes sufficiently shallow, the upstream long wave may steepen and break. This may have important ramifications for nutrient and/or pollution transport across a sharp density interface in stratified marine environments.

Further complications may arise if the intrusion contains sedimenting particles as is observed, for example, in the outflow of volcanic plumes. In this circumstance, the intrusion density decreases with time suggesting that a continuous vertical adjustment with respect to the upstream interface will occur. By assessing the impact of this effect on the front speed for a variety of conditions, it may be possible to predict the pattern of particle deposition for both planar and axisymmetric geometries.

Appendix A

Mathematical description of filling-box flows

A.1 Preliminary remarks

Following the studies of Linden, Lane-Serff & Smeed [55], Woods, Caulfield & Phillips [97], Kaye & Hunt [45] and many others, the ventilation analysis of Chapters 3, 4 and 5 makes liberal use of the turbulent plume equations in parameterizing buoyant convection from internal, time-invariant heat sources. Here, we present a rigorous derivation of these relations and provide a brief justification for their use[1]. As is demonstrated in mathematical detail below, plumes necessarily entrain external fluid and thus their behavior depends upon the properties and geometry of the ambient reservoir. Therefore the derivation is divided into two parts. First, it is assumed that the reservoir is infinite in extent so that temporal variations of the ambient are negligible, even if the flow is sustained over long time scales (Morton, Taylor & Turner [66]). Second, and of more relevance to building ventilation, we consider a finite reservoir for which the ambient density field evolves in time due to boundary deposition of plume fluid (Baines & Turner

[1] In contrast to the previous discussion, equations are here derived by assuming that the flow originates from a negatively-buoyant thermal source. Consistent with the discussion of Spiegel & Veronis [85] and Kundu [49], p. 112, this change of coordinate frame is immaterial so long as density differences are small so that the Boussinesq approximation may be applied.

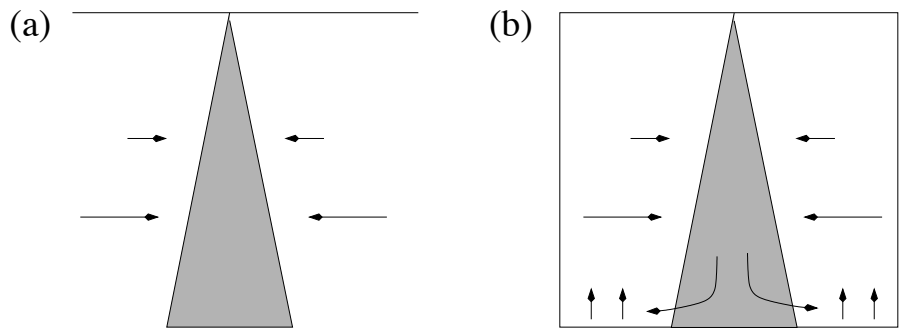

Figure A.1: Negatively-buoyant point-source plume falling into (a) an infinite, and, (b) a bounded environment.

[5], Germeles [30], Manins [62], Worster & Huppert [98]). The distinction between these disparate cases is illustrated schematically in figure A.1.

A.2 Formulation

Notwithstanding the differences between figure A.1a and A.1b, each flow is assumed to satisfy the following basic conditions:

(i) The volume and momentum fluxes are negligible at the (point) source,

(ii) The horizontal entrainment velocity is linearly related to the plume's local vertical velocity,

(iii) The buoyancy and velocity profiles of the plume are well-represented by Gaussian distributions[2].

From condition *(iii)*, we therefore define

$$b = B + (b_c - B)\mathrm{e}^{-r^2/a^2}\,, \qquad w = W + (w_c - W)\mathrm{e}^{-r^2/a^2}\,, \tag{A.1}$$

where $b_c(z)$ and $w_c(z)$ denote, respectively, the buoyancy and vertical speed at the plume core ($r = 0$) and $a(z)$ is the plume's characteristic radius. Furthermore, $B(z)$

[2]Alternatively, "top hat" profiles may be applied without any material change to the end result.

and $W(z)$ represent the buoyancy and velocity profiles in the far field, respectively. Localized plumes of the type considered here satisfy $|w_c| \gg |W|$. Hence, close to the centerline of the plume

$$w \simeq w_c \, \mathrm{e}^{-r^2/a^2} \, . \tag{A.2}$$

Regions over which the above approximation is valid are referred to as the "local scale." By contrast, regions far from the plume core where (A.1)b must be applied in place of (A.2) are referred to as the "global scale." Over both scales fluid motion is described by the mass, buoyancy (energy) and vertical momentum equations. In cylindrical coordinates, these are given, respectively, by

$$r^{-1}(r\,u)_r + w_z = 0 \, , \tag{A.3}$$

$$b_t + \vec{\nabla} \cdot (\mathbf{u} b) = \kappa \nabla^2 b \, , \tag{A.4}$$

$$w_t + r^{-1}(r\,u\,w)_r + (w^2)_z = b - B + \nu \nabla^2 w \, , \tag{A.5}$$

where r and u denote the radial coordinate and the corresponding radial velocity. Furthermore κ is the diffusivity, ν is the kinematic viscosity and subscripts indicate differentiation. For localized plumes, only the hydrostatic component of pressure is significant and hence fluctuating components due to turbulence may be neglected. Therefore, consistent with Turner [90], we write $B = p_z/\rho_0$ where ρ_0 denotes a reference density.

Integrating (A.3) over the local scale and applying (A.2) yields

$$[r\,u]_{r=r_1} + \tfrac{1}{2}(a^2\,w_c)_z = 0 \, , \tag{A.6}$$

where r_1 is selected such $r_1^2 \gg a^2$. The former term is evaluated using G. I. Taylor's entrainment hypothesis

$$[r\,u]_{r=r_1} = a\,u(a,z) = \alpha_p\,a\,w_c(z) \, ,$$

where $\alpha_p \simeq 0.1$ is the entrainment constant for an axisymmetric plume issuing from a point source (Turner [91]). Applying this result in (A.6) yields

$$(a^2\,w_c)_z = -2\alpha_p\,a\,w_c \, . \tag{A.7}$$

Table A.1: Mass, buoyancy and vertical momentum equations expressed in differential, integrated and flux form.

Differential form	
Mass	$r^{-1}(r\,u)_r + w_z = 0$
Buoyancy	$b_t + \vec{\nabla}\cdot(\mathbf{u}\,b) = \kappa\,\nabla^2 b$
Momentum	$w_t + r^{-1}(r\,u\,w)_r + (w^2)_z = b - B + \nu\,\nabla^2 w$
Integrated form	
Mass	$(a^2\,w_c)_z = -2\alpha_p\,a\,w_c$
Buoyancy	$\frac{1}{2}[a^2\,w_c(b_c - B)]_z = -a^2\,w_c\,B_z$
Momentum	$\frac{1}{2}(a^2\,w_c^2)_z = a^2\,(b_c - B)$
Flux form	
Mass	$Q_z = 2\alpha_p\,(2\pi\,M)^{1/2}$
Buoyancy	$F_z = -Q\,B_z$
Momentum	$M\,M_z = F\,Q$

In a similar fashion, the buoyancy and momentum equations can be integrated over the local scale (table A.1). Here, effects due to heat or momentum diffusion are neglected. Furthermore a quasi-steady state is assumed such that temporal variations are deemed insignificant *i.e.* $b_t = u_t \simeq 0$.

The integrated equations of table A.1 may be re-expressed in flux form by defining the volume, momentum and buoyancy fluxes as

$$Q = \pi\,a^2\,w_c\,, \qquad M = \tfrac{1}{2}\,\pi\,a^2\,w_c^2\,, \qquad F = \tfrac{1}{2}\,\pi\,a^2\,w_c(b_c - B)\,, \tag{A.8}$$

respectively. Thus it can be shown that

$$Q_z = 2\alpha_p(2\pi\,M)^{1/2}\,, \qquad F_z = -Q\,B_z\,, \qquad M\,M_z = F\,Q\,. \tag{A.9}$$

A.3 Infinite environment

Morton *et al.* [66] considered the behavior of the plume equations (A.9) for the special case of an unbounded ambient such that B and its vertical derivative represent independent variables. In the simplest possible scenario, $B_z = 0$, *i.e.* the

ambient is unstratified[3]. Hence $F_z = 0$ indicating that the buoyancy flux is a constant, $F = F_0 \equiv \frac{\pi}{2}[a^2\, w_c(b_c - B)]_{z=0}$. Scaling theory therefore suggests

$$Q \propto F_0^{1/3}\, z^{5/3}\,, \qquad M \propto F_0^{2/3}\, z^{4/3}\,. \tag{A.10}$$

The constants of proportionality are determined by forming the ratio of (A.9)a and c, separating variables and integrating. Thus it can be shown that

$$Q = \lambda(4F_0)^{1/3}\, z^{5/3}\,, \qquad M = \left(\frac{9\alpha_p\, F_0}{5}\right)^{2/3} \cdot \left(\frac{\pi}{2}\right)^{1/3}\, z^{4/3}\,, \tag{A.11}$$

where

$$\lambda = \frac{6\alpha}{5}\left(\frac{9\alpha}{10}\right)^{1/3}\, \pi^{2/3} \tag{A.12}$$

is the universal plume constant. Furthermore, the plume radius, a, and core velocity, w_c, are given by

$$a = \left(\frac{Q^2}{2\pi\, M}\right)^{1/2} = \tfrac{6}{5}\,\alpha_p\,|z|\,, \qquad w_c = \frac{2M}{Q} = -\frac{5}{6}\left(\frac{18F_0}{5\pi\,\alpha_p^2}\right)^{1/3}\, |z|^{-1/3}\,, \tag{A.13}$$

respectively. In the above equations, the ideal plume assumption has been invoked such that $Q(0) = M(0) = 0$. Plumes displaying a non-zero source volume and momentum flux are referred to as "non-ideal" and can be described by applying a "virtual origin" correction in the manner of Hunt & Kaye [40].

Uniformly-stratified environments are characterized by a buoyancy frequency $N = (-g\,\bar{\rho}_z/\rho_0)^{1/2}$ in which g is gravitational acceleration and $\bar{\rho}_z$ is the background density gradient. Vertically descending plumes of the type depicted in Figure A.1 increase in density as they fall due to entrainment. If the rate of entrainment is sufficiently rapid (or equivalently if $\bar{\rho}_z$ is sufficiently large), the plume will become neutrally-buoyant at a vertical distance $z_{neut} \propto F_0^{1/4}\, N^{-3/4}$ from the source. At this level, the plume fluid propagates into its surroundings as a radially-symmetric gravity current (Schooley [79], Wu [99], Schooley & Hughes [80], Manins [63], Faust & Plate [26], Flynn & Sutherland [29]).

[3]To leading order, this approximation is appropriate when modeling fluid discharge into the well-mixed surface boundary layer of the atmosphere.

A.4 Bounded environment

A.4.1 Evolution of the ambient density field

When the ambient is finite in extent (Figure A.1b), global dynamics are strongly coupled to local dynamics via entrainment and the deposition (and subsequent re-entrainment) of plume fluid. Explicitly, when the plume is first "switched on," dense fluid falls through the ambient and descends all the way to the bottom of the domain where it is discharged into a thin layer of approximately uniform thickness along the lower boundary of the control volume. A small fraction of this fluid is immediately recycled through the plume and the density of the layer deposited at the subsequent time step is therefore larger than that which formed at $t = 0$. By the same token, the layer formed over the following time interval must be denser still. The above process repeats *ad-infinitum* as the isopycnal layers in the far-field are slowly advected upward resulting in a stable, continuously-varying ambient density profile (Germeles [30]).

The spatio-temporal evolution of this stratification is determined by integrating (A.3) and (A.4) over the global scale. Applying (A.1) and the no-penetration boundary condition on the side and bottom surfaces, we find

$$A\,W + \pi\,a^2\,w_c = 0\,, \tag{A.14}$$

$$B_t + W\,B_z = \kappa\,B_{zz}\,. \tag{A.15}$$

where A is the total cross-sectional area. Heuristically speaking, (A.14) demonstrates that "the [upward] volume flux in the environment at any level must equal the [downward] flux in the plume" (Baines & Turner [5]). By the same token, (A.15) reveals that temporal variations in B are due to an imbalance between the upward advection and downward diffusion of the active scalar.

The far-field vertical velocity, W, can be eliminated from the problem by combining (A.14) and (A.15) whence

$$B_t - \frac{Q}{A}\,B_z = \kappa\,B_{zz}\,. \tag{A.16}$$

For filling-box flows of the type shown in figure A.1b, (A.9) and (A.16) quantify the dynamic interaction between the plume and the surrounding ambient.

A.4.2 Analytical solution of (A.9) and (A.16)

Baines & Turner [5] studied the long-time behavior of filling-box flows under the assumptions that $B_t \to$ constant and $\kappa = 0$. In this case, there exists a well-defined "first front" that separates discharged plume fluid from that which occupied the domain at the initial instant. Because diffusion effects are assumed negligible, the density jump across this front remains constant in time. The vertical position of the first front, z_{ff}, can be determined from

$$\frac{\mathrm{d}z_{ff}}{\mathrm{d}t} = -\frac{\pi\, a^2\, w_c}{A}\,, \tag{A.17}$$

where the plume radius, a, and core velocity, w_c, are determined by the analysis of §A.3, which is applicable for $z > z_{ff}$. Thus employing (A.13) in (A.17) yields

$$t = \frac{5}{4\alpha_p}\left(\frac{5}{18\alpha_p\,\pi^2\,F_0\,H^2}\right)^{1/3} A\left[\left(\frac{-H}{z_{ff}}\right)^{2/3} - 1\right], \tag{A.18}$$

where H is the total height of the control volume. Note that $z_{ff} < 0$ for all $t < \infty$ and hence in the absence of diffusion, a closed domain forced by an ideal source cannot become completely filled with dense plume fluid in finite time.

To determine the behavior of Q, M and F, non-dimensional independent variables ζ and τ are introduced such that

$$z = \zeta\, H\,, \qquad t = \frac{A\,\tau}{4\pi^{2/3}\,\alpha^{4/3}\,H^{2/3}\,F_0^{1/3}} \tag{A.19}$$

(Baines & Turner [5], Worster & Huppert [98]). Furthermore, non-dimensional volume (q), momentum (m) and buoyancy (f) fluxes are defined whereby

$$q = \frac{Q}{4\pi^{2/3}\,\alpha^{4/3}\,H^{5/3}\,F_0^{1/3}}\,, \tag{A.20}$$

$$m = \frac{M}{2\pi^{1/3}\,\alpha^{2/3}\,H^{4/3}\,F_0^{2/3}}\,, \tag{A.21}$$

$$f = F/F_0\,. \tag{A.22}$$

Finally, assuming $B_t \to$ constant for large t, we write

$$B = \frac{F_0^{2/3}\,(\delta - \tau)}{4\pi^{2/3}\,\alpha^{4/3}\,H^{5/3}}\,, \tag{A.23}$$

in which the non-dimensional variable δ captures the spatial variation of B, *i.e.* $\delta = \delta(\zeta)$. The governing equations (A.9) and (A.16) are therefore rewritten as

$$q_\zeta = m^{1/2}\,, \qquad f_\zeta = -q\,\delta_\zeta\,, \qquad m\,m_\zeta = f\,q\,, \qquad \delta_\zeta = -q^{-1}\,. \tag{A.24}$$

Baines & Turner [5] solved this 4×4 system subject to a constant buoyancy flux boundary condition at $\zeta = 0$, *i.e.*

$$\text{BC}: \;\; q(0) = 0\,, \qquad m(0) = 0\,, \qquad f(0) = 1\,.$$

Hence from (A.24) b,d we find that $f = 1 + \zeta$ and therefore

$$q_\zeta = m^{1/2}\,, \qquad m\,m_\zeta = q(1+\zeta)\,. \tag{A.25}$$

Equations (A.25) a,b are amenable to solution via perturbation techniques (see for example Ch. 3 of Bender & Orszag [6]). Consistent with (A.10), it can be shown that

$$q \sim 0.4597\zeta^{5/3} + 0.0589\zeta^{8/3} + \ldots\,, \tag{A.26}$$

and

$$m \sim 0.5872\zeta^{4/3} + 0.2409\zeta^{7/3} + \ldots\,. \tag{A.27}$$

These results offer insights into the plume's spatial variation for large t and are suitable for most flows of engineering interest. It must be emphasized, however, that (A.26) and (A.27) do not describe a steady solution to the filling-box equations because $B_t \neq 0$ by assumption. Analytical solutions in the long time limit $t \to \infty$ are of primary relevance in the context of large-scale geophysical flows and are given by Manins [62].

A.4.3 Numerical solution of (A.9) and (A.16)

An alternate, strictly numerical method for solving the coupled equations was proposed by Germeles [30]. The central feature of Germeles's algorithm is the assumption of separation of time scales such that "the evolution of the plume ... occur[s] much more rapidly than the evolution of the ambient density field ..." (Caulfield & Woods [19]), the latter being represented by a series of discrete steps (Conroy, Llewellyn Smith and Caulfield [21]). Thus for a particular instant in time, $t_\star$, the background stratification is assumed fixed, which allows (A.9) or its non-dimensional analogue to be integrated from $z = 0$ to $z = H$. With a prescribed time step, Δt, (A.16) may then be solved[4] for B, which yields the ambient density profile at time $t_\star + \Delta t$. As a result of entrainment into the plume, pre-existing density layers become smaller in vertical extent. In addition, because existing layers are advected towards the thermal source, mass continuity requires the addition of a new layer at the bottom of the control volume. This corresponds to the physical process of boundary deposition of dense plume fluid.

Once the discretized density field, B, is updated, the local equations given by (A.9) may be solved anew. Thus, for a well-defined initial condition, the system's evolution may be determined for arbitrarily large t.

A.5 Concluding remarks

Although somewhat involved, the foregoing discussion provides a useful analytical tool, which, when coupled with analogue laboratory experiments and/or full-scale CFD simulations, offers key qualitative and quantitative insights into fluid flow within ventilated buildings (Linden [53]). For example, (A.11) gives the convective volume flux above an isolated thermal source as a function of the vertical coordinate for unstratified surroundings. As suggested by the displacement ventilation analysis of Chapter 3, this result may be used to predict the volume of

[4] Again, it is assumed that mass diffusion effects may be neglected, *i.e.* $\kappa \simeq 0$.

buoyant fluid supplied to a chamber's hot, upper layer. For simple geometries, such of those considered in Chapter 3, this in turn specifies the system's total ventilation flow rate. Moreover, Germeles's algorithm may be easily extended to open control volumes that exchange mass and buoyancy with the external environment. In this case, flows are driven by pressure differences arising from stack effects, which introduces further terms into the conservation equations. This approach is applied in Chapter 4 when describing multi-chamber ventilation.

As noted in § 2.3, however, certain care is required in pursuing this line of inquiry. In particular, both the analytical treatment of §§ A.3 and A.4.2 and the numerical treatment of § A.4.3 assume that buoyant convection originates from a compact source and further that the resulting plume occupies a relatively small fraction of the chamber's total cross-sectional area. These assumptions are justified provided thermal inputs may be modeled as a series of discrete sources, no single one of which supplies a significant volume flux. Thus, for example, a ventilated filling-box model may be applied when describing the displacement ventilation of a single chamber whose thermal sources include building occupants and light machinery or electrical equipment. The virtual source correction described by Hunt & Kaye [40] may be used in parameterizing sources distributed over a small area. However, this model is inadequate for instances of broadly-distributed heat sources as is often associated with solar radiation through large windows. In this circumstance, *(i)* the interior space is typically well-mixed such that vertical gradients of temperature are small, and, *(ii)* heat transfer is more appropriately modeled by applying the expressions for Rayleigh-Bénard convection given, for example, by Denton & Wood [24]. Specific details of this approach are described by Gladstone & Woods [33], who examine the disparate flow regimes associated with the areal thermal forcing of a single chamber in the presence of an assistive or adverse external wind gradient.

A further limitation of the filling-box model in general, and Germeles's algorithm in particular, is that discharged plume fluid is assumed to spread instan-

taneously with no mixing. Although the consequence of the former assumption is believed to be small for most geometries of practical interest, mixing effects (for example due to overturning motions) have the impact of reducing vertical density gradients in the layer of discharged plume fluid. Thus, in certain cases, it may be acceptable to model this layer as being well-mixed for all time[5]. Conditions under which this assumption is valid in the context of multi-chamber ventilation flows are rigorously explored for a particular geometry in Chapters 4 and 5.

A final impact of mixing is to "smear" the first front. Thus, in industrial settings, the sharp density step predicted by the filling-box equations is typically diffused over some non-trivial vertical distance (Liu & Linden [59]). Some margin of error is therefore required in designing displacement ventilation systems for which the chamber's buoyant, upper layer and working space must not intersect.

[5]Linden *et al.* [55] apply this well-mixed hypothesis in their discussion of displacement ventilation flows. However, they consider solutions in the limit $t \to \infty$ rather than the transient approach towards steady state.

Appendix B

Fires and naturally-ventilated buildings

B.1 Ventilation and fire safety

The dangers associated with accidental fires in buildings and homes are due in large part to the noxious byproducts of combustion such as carbon dioxide, carbon monoxide and partially-burned fuel, all of which pose a severe threat of asphyxiation. Clearly, a critical aspect of occupant safety is the efficacy with which such byproducts are discharged to the external environment as the building is being evacuated of personnel. Natural ventilation of the type described in chapters 3, 4 and 5 offers some non-trivial advantages in this regard (Kramer & Gerhardt [48], Rooney & Linden [75]). Significantly, because natural ventilation relies upon a stable indoor stratification of temperature, a properly-designed system will by-and-large confine buoyant fluid (i.e. smoke) along the ceiling. This provides a relatively cool and smoke-free layer close to the floor, which is continually replenished by inflow of ambient fluid at low level.

By providing adequate ventilation for evacuating occupants, however, additional oxygen is also supplied for combustion. Hence fire growth within naturally-ventilated buildings is typically not ventilation-controlled. Although this may in-

crease the rate at which fuel is consumed, it also reduces the probability of "backdraft" or "flashover," which is typically associated with oxygen-depleted spaces that are rich in partially-burned or vaporized fuel. More specifically, flashover occurs once the chamber's internal pressure is sufficient to break a window or blow a door ajar at which point oxygen is supplied at a rapid rate, leading to an explosive (and potentially lethal) combustion of unburned hydrocarbons. Thus, Bishop & Drysdale [12] note that "life safety is closely associated with the duration of the growth period, both for those in the room of origin, and for those elsewhere in the building. The greater the duration of the preflashover phase, the longer the period of time available for the occupants to escape to a place of safety."

Fortunately, the non-Boussinesq effects associated with fire plumes have a relatively minor impact so that many of the salient results described previously (as well as those derived in the complementary analyses of Linden, Lane-Serff & Smeed [55], Hunt & Linden [41], [42], Kaye & Hunt [45] and others) also apply to the ventilation of relatively small fires. To the extent that non-Boussinesq effects are important, they are principally due to a modified entrainment relationship (Rooney & Linden [74]). Technical aspects of this difference are briefly reviewed in the following section.

B.2 Quantitative discussion

G. I. Taylor's entrainment hypothesis proposes that the radial entrainment velocity into an ascending or descending plume is linearly related to the plume's (height-dependent) vertical velocity, i.e.

$$u_e \propto w\,. \tag{B.1}$$

This relationship is consistent with the self-similar behavior of Boussinesq plumes. However, (B.1) proves inadequate when there exists a significant density disparity between the plume and ambient fluids in which case the flux of density deficiency rather than buoyancy is conserved (assuming unstratified surroundings). For this

non-Boussinesq circumstance, Ricou & Spalding [73] and Rooney & Linden [74] propose the following modification to (B.1)

$$u_e \propto w \left(\frac{\rho}{\rho_O}\right)^{1/2}, \tag{B.2}$$

where ρ and ρ_O denote, respectively, the densities of the plume and ambient. As a result of this adjustment, the plume radius, a, varies with ρ, ρ_O and the vertical coordinate, z, according to

$$a \propto |z| \left(\frac{\rho}{\rho_O}\right)^{-1/2}. \tag{B.3}$$

Comparison with (A.13)a shows that positively- and negatively-buoyant non Boussinesq plumes will be, respectively, wider and narrower than their Boussinesq counterparts.

Density effects also appear in the expressions describing the ventilation of a single chamber of height H with upper and lower openings of cross-sectional areas A_o and A_i, respectively. Assuming the interior space is stratified in the manner of chapter 4, the interface height, H_l, is given by

$$\lambda^3 H_l^5 = \tilde{A}_\star^2 (H - H_l), \tag{B.4}$$

where

$$\tilde{A}_\star = \frac{\Theta^{1/2} A_o A_i}{\left[\frac{1}{2}\left(A_o^2 + \frac{A_i^2}{\Theta}\right)\right]^{1/2}},$$

in which λ is the universal plume constant and Θ gives the ratio of the upper and lower layer densities. It must be emphasized, however, that due to turbulent entrainment, $\Theta^{1/2} \simeq 1$ in most instances. Therefore H_l "is little affected by departures from the Boussinesq value" (Rooney & Linden [75]). Because similar conclusions may also be drawn for more complicated flow domains involving multiple chambers, a naturally-ventilated building that effectively removes waste heat should also provide adequate ventilation in the event of an accidental fire.

Appendix C

Multi-chamber ventilation (non-ideal source) – Mathematical details

C.1 Illustrative derivation

Because the theoretical results of Chapter 5 are developed rather quickly[1], a representative derivation is performed herein to further illuminate the previously applied methodology. More specifically, we shall consider the results of table 5.1 to demonstrate how the quartic polynomial equations in q_o are determined. For simplicity, dimensional variables are favored with scalings applied only at the end of the discussion to make an explicit connection with the results given above.

Attention is first of all focused on the system's early-time dynamics for which the directions of flow through the lower openings must be as indicated in figure C.1. Although the forced chamber supports a two-layer stratification, contaminated plume fluid cannot yet accumulate in the unforced chamber because $Q_B > 0$ indicating flow from left-to-right through the lower internal opening. Consequently, the expressions of hydrostatic pressure balance for the forced and un-

[1]This material has been submitted as an extended abstract to the 6th International Symposium on Stratified Flows (ISSF) for which there is a rigid page limit.

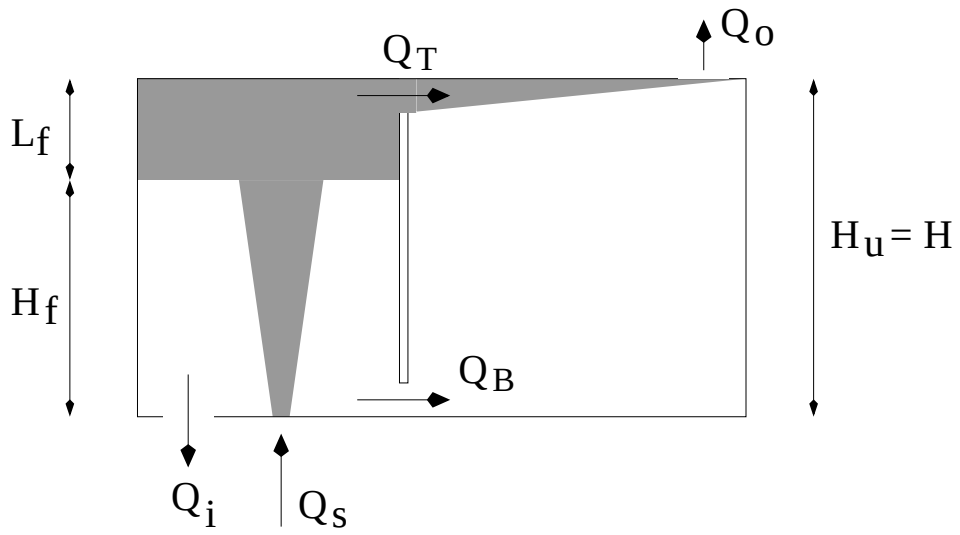

Figure C.1: Ventilation flow behavior for $t = 0^+$. Consistent with the discussion of Chapter 5, flows are defined to be positive in the directions specified above.

forced chambers read

$$\frac{p_f(H)}{\rho_a} = \frac{p_f(0)}{\rho_a} - g\,H_f - \frac{g\,\rho_f}{\rho_a}\,L_f\,, \tag{C.1}$$

$$\frac{p_u(H)}{\rho_a} = \frac{p_u(0)}{\rho_a} - g\,H\,, \tag{C.2}$$

respectively, where variables are defined as in Chapter 5. Equations (C.1) and (C.2) therefore suggest that

$$\frac{p_f(0) - p_u(0)}{\rho_a} = \frac{p_f(H) - p_u(H)}{\rho_a} - I_f\,, \tag{C.3}$$

where the integral buoyancy term I_f is given by (5.5). Hence, applying Bernoulli's principle for orifice flow to both sides of (C.3), we find

$$\frac{Q_B}{A} = \sqrt{\frac{Q_T^2}{A^2} - 2I_f}\,. \tag{C.4}$$

Similar reasoning shows that

$$\frac{Q_i}{A} = \sqrt{\frac{Q_T^2}{A^2} + \frac{Q_o^2}{A^2} - 2I_f}\,. \tag{C.5}$$

The preceding expressions may be combined with the equations describing mass balance. For the Boussinesq system considered here, these are given by

$$Q_s = Q_i + Q_o \,, \tag{C.6}$$

$$Q_o = Q_T + Q_B \,. \tag{C.7}$$

More specifically, applying (C.4) in (C.7) yields

$$Q_T = \tfrac{1}{2}\, Q_o + \frac{A^2\, I_f}{Q_o} \,. \tag{C.8}$$

Combining this result with (C.5) it can be shown that

$$\frac{Q_i^2}{A^2} = \tfrac{5}{4}\frac{Q_o^2}{A^2} + \frac{A^2\, I_f^2}{Q_o^2} - I_f \,. \tag{C.9}$$

Equation (C.6) may now be applied to eliminate Q_i from (C.9). After some elementary algebra, we find

$$0 = \tfrac{1}{4} Q_o^4 + 2 Q_s\, Q_o^3 - Q_o^2\, (Q_s^2 + A^2\, I_f) + A^4\, I_f^2 \,. \tag{C.10}$$

Dividing each term by $Q_v^4 = (A^{2/3}\, B_s^{1/3}\, H^{1/3})^4$ yields

$$0 = \tfrac{1}{4} q_o^4 + 2 q_s\, q_o^3 - q_o^2\, (q_s^2 + i_f) + i_f^2 \,, \tag{C.11}$$

which is identical to the first equation of table 5.1.

As the two-chamber system illustrated in figure C.1 evolves in time, we expect one or both of Q_B and Q_i to change sign, indicating a change of flow direction through either the lower internal or external opening. The governing polynomial equations germane to these cases may be obtained through a similar analysis to that outlined above. In each case, however, it is assumed that both chambers contain a layer of contaminated plume fluid. This necessitates a slight modification to (C.2), the expression for hydrostatic balance in the unforced chamber and is reflected by the appearance of i_u in equations 2, 3 and 4 of table 5.1.

C.2 Further remarks

Whereas the analytical results presented in table 5.1 do not by themselves describe the time evolution of the multi-chamber system, a surprising amount of information may nonetheless be derived through simple inspection of these expressions. For example, although the direction of flow through the lower openings must be as shown in figure C.1 immediately after the (non-ideal) plume is "switched on," both Q_B and Q_i must change sign if the chambers are to evolve towards a ventilated final state. These flow adjustments are not expected to occur simultaneously, however, so clearly one of Q_B or Q_i must change sign before the other. Moreover, since such transitions are expected to be smooth, a corresponding mathematical continuity is required between equations 1 and 2/4 of table 5.1 in the respective limits $Q_B \to 0$ and $Q_i \to 0$. Interestingly, this continuity is observed only in the former case, from which we deduce that it is unlikely to observe inflow through the lower external opening with flow from left-to-right through the lower internal opening. Detailed analysis of the ordinary differential equations given by (5.6) and (5.7) confirms this supposition. Furthermore, with $Q_B = 0$ and outflow through the lower external opening, equations 1 and 2 of table 5.1 show that $Q_o = Q_i = Q_T = Q_s/2$, i.e. equal volumes of fluid are discharged at floor- and ceiling-level.

Unfortunately, the results summarized above appear to be specific to the particular building geometry under investigation and are therefore not easily extended to multi-chamber systems involving a different number/positioning of internal and external openings. Further study is required to determine whether a simple analysis of the type given above is worthwhile in more general settings.

C.3 Analysis of (5.14) for $\zeta_s \to 0$

Although it is too difficult to solve for $h_{f\infty}$ analytically from (5.14), for small ζ_s (*i.e.* small Q_s) one can show that

$$h_{f\infty} = h_{f\infty,0} - \frac{\zeta_s \, h_{f\infty,0}^4}{\frac{2\zeta_s^5}{15 q_s^3} + h_{f\infty,0}^4} + \mathcal{O}(\zeta_s^{4/3}) \,, \tag{C.12}$$

where $h_{f\infty,0}$ solves the following non-linear equation

$$\lambda^3 \, h_{f\infty,0}^5 = \frac{2}{3} \, \lambda^3 \frac{\zeta_s^5}{q_s^3} (1 - h_{f\infty,0}) = \frac{2}{3} \left(\frac{A}{H^2} \right)^2 (1 - h_{f\infty,0}) \,. \tag{C.13}$$

This result complements the analysis of Linden, Lane-Serff & Smeed [55] who studied the ventilation of a single chamber by an ideal (*i.e.* zero volume flux) plume source and derived a steady state condition of the form

$$\lambda^3 \, h_\infty^5 = \left(\frac{A}{H^2} \right)^2 (1 - h_\infty) \,. \tag{C.14}$$

To lowest order in Q_s, therefore, the impact of the unforced chamber is to reduce the effective opening area by a factor of $\sqrt{2/3}$, as is suggested by (4.15) with $A_t = A_\star = A$.

Appendix D

Riemann invariants of the shallow water equations

D.1 The shallow water approximation

In many two-dimensional flows of geophysical relevance, the channel or basin depth is much smaller than typical horizontal wavelengths. Thus, the fluid layer may be considered "shallow" meaning that *(i)* the vertical velocity, w, is small with respect to the horizontal velocity, u, *(ii)* the vertical pressure gradient is hydrostatic, and, *(iii)* u is depth-independent in each fluid layer (Kundu [49], Pratt & Whitehead [71]). If the flow geometry is sufficiently simple, the equations of motion may then admit closed, analytical solutions by which combinations of flow variables termed "Riemann invariants" remain fixed for observers traveling at the Doppler-shifted, long wave speeds. These concepts are explored in mathematical detail below, both for homogeneous and density-stratified systems.

D.2 One-layer flow

We consider the flow of a uniform density fluid of depth $D(x,t)$ over a flat, horizontal boundary (figure D.1). For simplicity, rotational effects are assumed negligible, as is appropriate provided the Rossby number $\mathrm{Ro} \equiv \hat{U}/f\,\hat{L}$ is much less

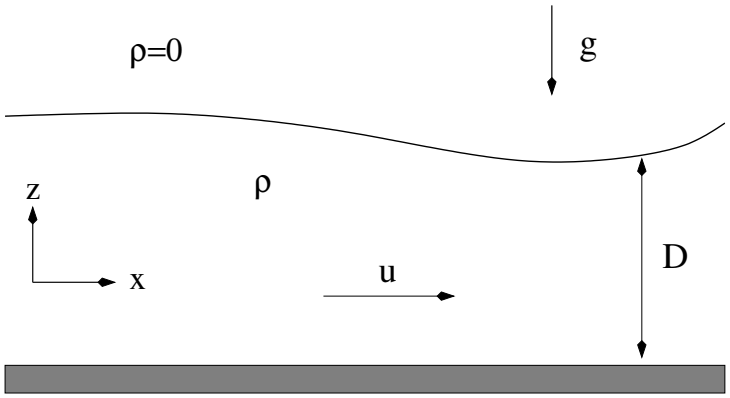

Figure D.1: One-layer flow over a rigid horizontal surface.

than unity. Here, $\hat{U}$ and $\hat{L}$ denote characteristic velocity and horizontal length scales, respectively. Moreover, f is the Coriolis parameter defined by (7.4.1) of Gill [32]. Mass and momentum conservation are therefore expressed as

$$\frac{\partial D}{\partial t} + u\,\frac{\partial D}{\partial x} + D\,\frac{\partial u}{\partial x} = 0\,, \tag{D.1}$$

$$\frac{\partial u}{\partial t} + u\,\frac{\partial u}{\partial x} + g\,\frac{\partial D}{\partial x} = 0\,, \tag{D.2}$$

respectively (Howell [38], Stoker [86]). By suitable change of variables to canonical or "characteristic" coordinates, this coupled system of hyperbolic partial differential equations can be re-written as a pair of ordinary differential equations. To illustrate this technique, we first note that

$$\mathrm{d}D = \frac{\partial D}{\partial t}\,\mathrm{d}t + \frac{\partial D}{\partial x}\,\mathrm{d}x\,, \qquad \mathrm{d}u = \frac{\partial u}{\partial t}\,\mathrm{d}t + \frac{\partial u}{\partial x}\,\mathrm{d}x\,. \tag{D.3}$$

Thus (D.1), (D.2) and (D.3) may be expressed in matrix form as

$$\begin{bmatrix} 1 & u & 0 & D \\ 0 & g & 1 & u \\ \mathrm{d}t & \mathrm{d}x & 0 & 0 \\ 0 & 0 & \mathrm{d}t & \mathrm{d}x \end{bmatrix} \begin{bmatrix} D_t \\ D_x \\ u_t \\ u_x \end{bmatrix} = \begin{bmatrix} 0 \\ 0 \\ \mathrm{d}D \\ \mathrm{d}u \end{bmatrix} \tag{D.4}$$

Here subscripts denote differentiation with respect to time, t, and the (horizontal) spatial coordinate, x. Along the characteristic curves, the determinant of the

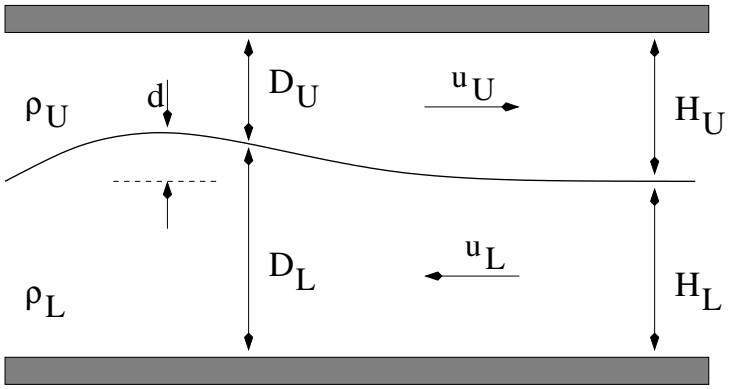

Figure D.2: Two layer flow between rigid horizontal surfaces.

above 4×4 matrix must vanish (Ames [2], Zauderer [101]). In the present context, therefore, these space-time curves are given by the characteristic equations

$$\frac{\mathrm{d}x}{\mathrm{d}t} \equiv \lambda_{\pm} = u \pm \sqrt{g\,D}\,. \tag{D.5}$$

Motivated by (D.5), a total derivative is defined such that

$$\frac{\mathrm{D}}{\mathrm{D}t} = \frac{\partial}{\partial t} + (u \pm \sqrt{g\,D})\,\frac{\partial}{\partial x}\,,$$

whereby the governing equations (D.1) and (D.2) reduce to

$$\frac{\mathrm{D}}{\mathrm{D}t}(u \pm 2\sqrt{g\,D}) = 0\,. \tag{D.6}$$

Recognizing $\sqrt{g\,D}$ as the non-shifted long wave speed, c, we conclude that the Riemann invariants $u \pm 2c$ are conserved along the respective characteristics $\lambda_{\pm} = u \pm c$ (Baines [4], Howell [38]).

D.3 Two-layer flow

Unfortunately, system complexity increases markedly as extra degrees of freedom are introduced (Rottman & Simpson [76], Keller & Chyou [46], Klemp, Rotunno & Skamarock [47], Baines [4], Lowe, Rottman & Linden [61]). This is shown below for the case of two-layer stratified flow, which is depicted schematically in figure D.2. The lower layer, of density ρ_L, has perturbed and unperturbed depths

of $D_L(x,t)$ and H_L, respectively. Conversely, the upper layer, of density ρ_U, has perturbed and unperturbed depths of $D_U(x,t)$ and H_U, respectively. The total channel height is assumed constant, *i.e.* $H = H_U + H_L = D_U + D_L$. Moreover, it is assumed that the density difference across the interface is relatively small so that the flow is Boussinesq.

Proceeding as before, mass conservation may be applied in the upper and the lower layers, whence

$$\frac{\partial D_U}{\partial t} + \frac{\partial}{\partial x}(D_U\, u_U) = 0\,, \tag{D.7}$$

$$\frac{\partial D_L}{\partial t} + \frac{\partial}{\partial x}(D_L\, u_L) = 0\,. \tag{D.8}$$

Adding and subtracting these results, it can be shown that

$$D_U\, u_U + D_L\, u_L = Q(t)\,, \tag{D.9}$$

$$\frac{\partial}{\partial t}(D_L - D_U) + \frac{\partial}{\partial x}(D_L\, u_L - D_U\, u_U) = 0 \tag{D.10}$$

in which Q is the (time-varying) mean flow. For simplicity, we assume that the lateral boundaries of the domain are closed such that $Q = 0$.

Momentum conservation is expressed via the Euler equations, which become

$$\frac{\partial u_U}{\partial t} + \frac{\partial}{\partial x}\left[\tfrac{1}{2}u_U^2 + g\,H + \frac{p^\star}{\rho_U}\right] = 0\,, \tag{D.11}$$

$$\frac{\partial u_L}{\partial t} + \frac{\partial}{\partial x}\left[\tfrac{1}{2}u_L^2 + g\,\left(D_L + \frac{\rho_U}{\rho_L}\,D_U\right) + \frac{p^\star}{\rho_L}\right] = 0\,, \tag{D.12}$$

in the upper and lower layers, respectively. Here $p^\star$ is the (spatially-variable) pressure along the upper boundary, which may be eliminated by taking the difference between (D.11) and (D.12). Thus

$$\frac{\partial}{\partial t}(u_L - u_U) + \frac{\partial}{\partial x}\left[\tfrac{1}{2}(u_L^2 - u_U^2) - g'_{LU}\,D_U\right] = 0\,, \tag{D.13}$$

where the reduced gravity g'_{LU} is given by

$$g'_{LU} = g\,\left(\frac{\rho_L - \rho_U}{\rho_O}\right)\,,$$

in which ρ_O denotes a reference density.

With H fixed, (D.9), (D.10) and (D.13) represent three equations in the three unknowns D_L, u_U and u_L. This 3×3 system may be reduced to a 2×2 system by applying the coordinate transformation suggested by Baines [4] in which

$$v = u_L - u_U \,, \qquad d = H_U - D_U = D_L - H_L \tag{D.14}$$

are defined, respectively, as the velocity jump across the interface and the magnitude of the interfacial displacement[1] (figure D.2). Using this approach, the mass and momentum balances quantified by (D.9), (D.10) and (D.13) may be re-written as

$$\frac{\partial d}{\partial t} + \frac{\partial}{\partial x}\left[\frac{v\,(H_U - d)\,(H_L + d)}{H}\right] = 0\,, \tag{D.15}$$

$$\frac{\partial v}{\partial t} + \frac{\partial}{\partial x}\left[g'_{LU}\,d + \frac{v^2\,(H_U - H_L - 2d)}{2H}\right] = 0\,. \tag{D.16}$$

In matrix form, therefore,

$$\begin{bmatrix} 1 & \alpha_1 & 0 & \alpha_2 \\ 0 & \alpha_3 & 1 & \alpha_1 \\ \mathrm{d}t & \mathrm{d}x & 0 & 0 \\ 0 & 0 & \mathrm{d}t & \mathrm{d}x \end{bmatrix} \begin{bmatrix} d_t \\ d_x \\ v_t \\ v_x \end{bmatrix} = \begin{bmatrix} 0 \\ 0 \\ \mathrm{d}d \\ \mathrm{d}v \end{bmatrix} \tag{D.17}$$

where, for notational economy, the following variables have been introduced

$$\alpha_1 = \frac{v\,(H_U - H_L - 2d)}{H}\,, \quad \alpha_2 = \frac{(H_U - d)\,(H_L + d)}{H}\,, \quad \alpha_3 = g'_{LU} - \frac{v^2}{H}\,. \tag{D.18}$$

Consistent with the analysis of § D.1, special values of $\lambda_\pm \equiv \frac{\mathrm{d}x}{\mathrm{d}t}$ are sought that result in a null determinant. These are given by

$$\begin{aligned} \lambda_\pm &= \alpha_1 \pm \sqrt{\alpha_2\,\alpha_3} \\ &= \frac{v\,(H_U - H_L - 2d)}{H} \pm \sqrt{\left(g'_{LU} - \frac{v^2}{H}\right)\,\frac{(H_U - d)\,(H_L + d)}{H}} \end{aligned} \tag{D.19}$$

[1] Note that the definition of d applied here is somewhat different from that considered in Chapter 7. There, d represents the amplitude of the upstream wave, whose value is fixed by the initial conditions through (7.30). Here, d denotes the interface displacement at any point along the wave, not merely the wave crest. Thus, in the present discussion, d is a function of both time, t, and the horizontal coordinate, x.

The characteristic equations defined by (D.19) may be exploited in re-writing the mass and momentum equations given, respectively, by (D.15) and (D.16). Hence

$$\frac{\mathrm{D}d}{\mathrm{D}t} + (\alpha_1 - \lambda_\pm)\,\frac{\partial d}{\partial x} + \alpha_2\,\frac{\partial v}{\partial x} = 0\,, \tag{D.20}$$

$$\frac{\mathrm{D}v}{\mathrm{D}t} + (\alpha_1 - \lambda_\pm)\,\frac{\partial v}{\partial x} + \alpha_3\,\frac{\partial d}{\partial x} = 0\,, \tag{D.21}$$

where the material derivative is defined by

$$\frac{\mathrm{D}}{\mathrm{D}t} \equiv \frac{\partial}{\partial t} + \lambda_\pm\,\frac{\partial}{\partial x}\,.$$

Adding (D.20) and (D.21), it can be shown that the Riemann invariant appropriate to two-layer, Boussinesq, shallow water flow is given by the solution of the following ordinary differential equation[2]

$$\frac{\mathrm{d}v}{\mathrm{d}d} = \frac{\alpha_3}{\alpha_1 - \lambda_\pm} = \mp\sqrt{\frac{\alpha_3}{\alpha_2}} = \mp\sqrt{\frac{g'_{LU}\,H - v^2}{(H_U - d)\,(H_L + d)}}\,. \tag{D.22}$$

Solving this relation by separation of variables and applying the relevant boundary conditions while writing $v = -w_U\,H/D_L$ yields (7.26), the desired result.

[2]Here, it is assumed that $\alpha_3 \neq 0$, *i.e.* the flow is subcritical with $v^2 < g'_{LU}\,H$. Exact analytical solutions to the governing equations do not exist when this condition is invalid. For details, see for example Lowe *et al.* [61]

Appendix E

Direct numerical simulation algorithm

E.1 Preliminary remarks

In their most general form, the mass, momentum and energy equations that describe density-stratified, two-dimensional Boussinesq turbulent flow are given by

$$\nabla \cdot \mathbf{u} = 0\,, \tag{E.1}$$

$$\frac{\mathrm{D}u}{\mathrm{D}t} = -\frac{1}{\rho_0}\frac{\partial \mathcal{P}}{\partial x} + \nu\,\nabla^2 u\,, \tag{E.2}$$

$$\frac{\mathrm{D}v}{\mathrm{D}t} = -\frac{1}{\rho_0}\frac{\partial \mathcal{P}}{\partial y} - \frac{\rho'\,g}{\rho_0} + \nu\,\nabla^2 v\,, \tag{E.3}$$

$$\frac{\mathrm{D}\rho}{\mathrm{D}t} = \frac{\nu}{\mathrm{Sc}}\,\nabla^2 \rho\,. \tag{E.4}$$

This set of equations is identical to that provided in Chapter 8 except that, consistent with the engineering as opposed to the geophysical literature, y rather than z is used to denote the vertical coordinate. Subject to the appropriate initial and boundary conditions, these (primitive-variable) equations describe both the initial collapse and subsequent propagation of intrusive gravity currents. Here, (E.1) through (E.4) are solved numerically using the direct numerical simulation (DNS) algorithm Diablo, which was originally designed by Prof. Thomas R. Bewley and

adapted for stratified flow by John R. Taylor. Diablo may in general be applied to two- or three-dimensional flow where the dependent variables satisfy periodic boundary conditions in at least two directions. In the present context, a symmetric channel flow configuration is selected in which flow variables are periodic in the streamwise direction, x, and non-periodic in the wall-normal direction, y (see for example figure 6 of Sutherland, Flynn & Dohan [87]). For the purposes of numerical accuracy in evaluating derivatives with respect to the streamwise coordinate, a Fourier decomposition is applied in this (periodic) direction whereby

$$\mathcal{N}(x,\, y,\, t) = \sum_{-\frac{N_x}{2}+1}^{\frac{N_x}{2}-1} \hat{\mathcal{N}}(k_n,\, y,\, t)\, \mathrm{e}^{\mathrm{i}\, k_n\, x}\,. \tag{E.5}$$

Here $k_n = 2\pi\, n/L_x$ denotes the horizontal wavenumber in which L_x is the total horizontal extent, N_x is the number of grid points in the x-direction and $\mathcal{N} = \mathbf{u}$, ρ or $\mathcal{P}$, which are defined in Chapter 8 (Birman, Martin & Meiburg [11]). Thus with $\mathcal{N}$ given by (E.5),

$$\frac{\partial \mathcal{N}}{\partial x} = \sum_{-\frac{N_x}{2}+1}^{\frac{N_x}{2}-1} \mathrm{i}\, k_n\, \hat{\mathcal{N}}(k_n,\, y,\, t)\, \mathrm{e}^{\mathrm{i}\, k_n\, x}\,, \tag{E.6}$$

i.e. differentiation in physical space corresponds to multiplication in wavenumber space. Nonetheless, the efficacy of the decomposition given by (E.5) depends critically on the computational ease with which the Fourier modes $\hat{\mathcal{N}}$ may be determined. To this end, Diablo employs a uniform, non-staggered grid in the x-direction and utilizes the optimized, open-source discrete fast-Fourier-transform routine FFTW (http://www.fftw.org)[1]. Orszag's 2/3 de-aliasing rule is applied such that $\hat{\mathcal{N}} \equiv 0$ if $|n| > N_x/3$, which significantly reduces spurious energy transfer from high- to low-wavenumber modes (Canuto *et al.* [17]).

[1] A detailed discussion of FFT algorithms is provided in Press *et al.* [72].

E.2 Spatial discretization in the wall-normal direction

In order to couple the pressure at adjacent nodes and avoid spurious, fine-scale oscillations, a staggered (non-stretched) grid is selected in the y-direction, as illustrated schematically in figure E.1. This staggered grid is, in effect, composed of two inter-woven coarse grids: GYF (black circles in figure E.1) and GY (white circles in figure E.1). Consistent with the discussion of Bewley [8], the horizontal velocity, pressure and density are defined at the GYF nodes whereas the vertical velocity is defined at the GY nodes. Because each GY node lies exactly half-way in between adjacent GYF nodes and vice-versa, interpolation from one grid to another is straightforward. Such interpolations are necessary when considering "cross" terms such as $\partial(u\,v)/\partial x$ or $\partial(u\,v)/\partial y$.

E.3 Temporal discretization

An explicit, third-order, low-storage Runge-Kutta-Wray (RKW3) scheme and an implicit Crank-Nicholson (CN) scheme are used to advance the flow in time. The latter algorithm is selected because it is unconditionally-stable for purely diffusive processes. Although unconditional stability is not preserved once advective transport is included, the Crank-Nicholson algorithm nonetheless represents a robust numerical scheme provided the timestep, Δt, is sufficiently small.

Because a relatively fine resolution is selected in the wall-normal direction, diffusive terms involving a y-derivative are treated implicitly. All other terms are treated explicitly. Thus at each fractional timestep and for each dependent variable, a linear system of equations must be solved. However, because second-order finite differences are applied, $\Upsilon = 3$ in which Υ is the matrix bandwidth (i.e. the matrix is tridiagonal). Thus, the highly-efficient Thomas algorithm[2] may be employed.

The governing equations are solved starting with (E.4) in which the (di-

[2]See for example p. 142 of Pozrikidis [70]

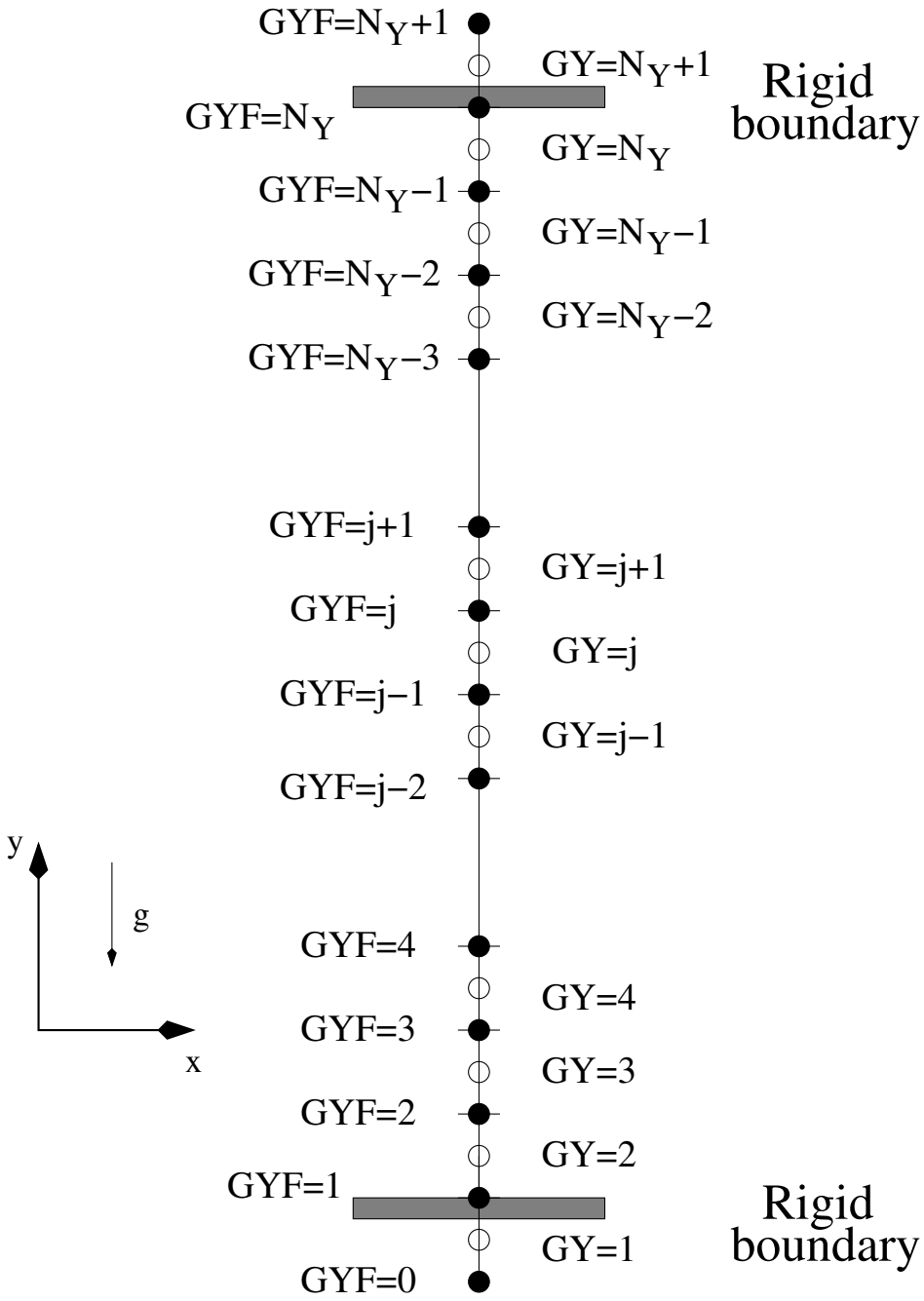

Figure E.1: Grid structure in the wall-normal (y) direction. "Ghost" cells are required when Neumann boundary conditions are specified.

vergence free) velocity field from the previous fractional timestep is applied in advecting the scalar component ρ. Thereafter, (E.3) then (E.2) are solved for the vertical and horizontal components of velocity, respectively. In general, this intermediate field, $\hat{\mathbf{u}}$ does not satisfy the solenoidal condition expressed by (E.1). Rather the velocity field is made divergence-free by considering the pressure correction, $\phi \propto \mathcal{P}^{rk+1} - \mathcal{P}^{rk}$, in which $\mathcal{P}^{rk+1}$ and $\mathcal{P}^{rk}$ denote, respectively, the pressure at fractional timesteps $rk+1$ and rk. More specifically, it can be shown that (T. R. Bewley – personal communication)

$$\mathbf{u}^{rk+1} = \hat{\mathbf{u}} - \nabla\phi\,, \tag{E.7}$$

in which $\mathbf{u}^{rk+1}$ is the updated, solenoidal velocity field. Thus, taking the divergence of (E.7) yields

$$\nabla^2\,\phi = \nabla\cdot\hat{\mathbf{u}}\,. \tag{E.8}$$

The pressure correction, ϕ, may therefore be determined by solving a Poisson equation. Once ϕ is known, the velocity and pressure fields may be updated accordingly and the solution at the next fractional timestep can be computed.

E.4 Further considerations

E.4.1 Pressure field

The pressure, $\mathcal{P}$, is not specified at the initial instant. Rather it is determined from (E.2) and (E.3) via

$$\frac{1}{\rho_0}\,\nabla^2\mathcal{P} = -\nabla\cdot(\mathbf{u}\cdot\nabla\mathbf{u})\,. \tag{E.9}$$

Contributions due to the density perturbation term $\partial\rho'/\partial y$ are omitted because these are vanishingly small when $t = 0$.

E.4.2 Momentum and density diffusion

Simulations employ a physical value for momentum diffusivity, i.e. $\nu = 0.01\,\mathrm{cm}^2/\mathrm{s}$. Consistent with related analyses, however, the Schmidt number, Sc =

ν/κ_ρ, is set to unity, which overestimates the mass diffusivity of salt water, κ_ρ, by approximately three orders of magnitude. As noted in Chapter 8, this choice is necessary for the purposes of numerical stability. However its dynamic impact to the particular problem at hand[3] is believed to be small. Summarizing related numerical simulations, Sutherland *et al.* [87] note that "...the [scalar] diffusivity term...acted solely as a filter to damp small-scale numerical noise. The value we used [for κ_ρ] was still sufficiently small that the essential dynamics of the gravity current's propagation and wave generation were not affected." Indeed the most significant physical consequence of selecting $\mathrm{Sc} = 1$ is that the interface separating the upper and lower layers becomes progressively more diffuse over the course of a particular numerical simulation. With $g'_{LU} = 9.8\,\mathrm{cm/s^2}$, this limits the maximum run time to $\tau \lesssim 10\,\mathrm{s}$, since, as was demonstrated by Faust & Plate [26], a finite interface thickness may exert some non-trivial influence on the intrusion's speed of propagation.

[3]Overestimating Sc may prove more dangerous in the numerical modeling of chemically reacting and/or non-Boussinesq flows for which the dependent variables can exhibit a sensitive dependence on the fluid's composition and/or temperature.

Bibliography

[1] R. Amen and T. Maxworthy. The gravitational collapse of a mixed region into a linearly stratified solution. *J. Fluid Mech.*, 96:65–80, 1980.

[2] W. F. Ames. *Nonlinear Partial Differential Equations in Engineering*. Academic Press, New York, 1965.

[3] L. Armi. Some evidence for boundary mixing in the deep ocean. *J. Geophys. Res.*, 83:1971–1979, 1978.

[4] P. G. Baines. *Topographic effects in Stratified Flows*. Cambridge University Press, Cambridge, England, 1995.

[5] W. D. Baines and J. S. Turner. Turbulent buoyant convection from a source in a confined region. *J. Fluid Mech.*, 37:51–80, 1969.

[6] C. M. Bender and S. A. Orszag. *Advanced Mathematical Methods for Scientists and Engineers*. Springer Verlag, New York, 1999.

[7] T. B. Benjamin. Gravity currents and related phenomena. *J. Fluid Mech.*, 31:209–248, 1968.

[8] T. R. Bewley. *Optimal and Robust Control and Estimation of Transition, Convection, and Turbulence*. PhD thesis, Stanford University, 1999.

[9] T. R. Bewley, P. Moin, and R. Temam. DNS-based predictive control of turbulence: an optimal benchmark for feedback algorithms. *J. Fluid Mech.*, 447:179–225, 2001.

[10] V. K. Birman, V. A. Battandier, E. Meiburg, and P. F. Linden. Lock-exchange flows in sloping channels. *J. Fluid Mech.*, submitted, 2006.

[11] V. K. Birman, J. E. Martin, and E. Meiburg. The non-Boussinesq lock-exchange problem. Part 2. High-resolution simulations. *J. Fluid Mech.*, 537:125–144, 2005.

[12] S. R. Bishop and D. D. Drysdale. Fires in compartments: the phenomenon of flashover. *Phil. Trans. R. Soc. Lond.*, 356:2855–2872, 1998.

[13] L. J. Bloomfield and R. C. Kerr. Turbulent fountains in a stratified fluid. *J. Fluid Mech.*, 358:335–356, 1998.

[14] L. J. Bloomfield and R. C. Kerr. Turbulent fountains in a confined stratified environment. *J. Fluid Mech.*, 389:27–54, 1999.

[15] R. T. Bonnecaze, H. E. Huppert, and J. R. Lister. Particle-driven gravity currents. *J. Fluid Mech.*, 250:339–369, 1993.

[16] R. E. Britter and J. E. Simpson. A note on the structure of the head of an intrusive gravity current. *J. Fluid Mech.*, 112:459–466, 1981.

[17] C. Canuto, M. Y. Hussaini, A. Quarteroni, and T. A. Zang. *Spectral Methods in Fluid Dynamics*. Springer-Verlag, New York, 1988.

[18] C. P. Caulfield and A. W. Woods. The evolution of plume with non-monotonic mixing behaviour. *Geophys. Astrophys. Fluid Dyn.*, 79:173–199, 1995.

[19] C. P. Caulfield and A. W. Woods. The mixing in a room by a localized finite-mass-flux source of buoyancy. *J. Fluid Mech.*, 471:33–50, 2002.

[20] H.-B. Cheong, J. J. P. Kuenen, and P. F. Linden. The front speed of intrusive gravity currents. *J. Fluid Mech.*, 552:1–11, 2006.

[21] D. T. Conroy, S. G. Llewellyn Smith, and C. P. Caulfield. Evolution of a chemically reacting plume in a ventilated room. *J. Fluid Mech.*, 537:221–253, 2005.

[22] S. J. D. D'Alessio, T. B. Moodie, J. P. Pascal, and G. E. Swaters. Intrusive gravity currents. *Stud. Appl. Math.*, 98:19–46, 1997.

[23] F. de Rooij. *Sedimenting particle-laden flows in confined geometries*. PhD thesis, University of Cambridge, 1999.

[24] R. A. Denton and I. R. Wood. Turbulent convection between two horizontal plates. *Int. J. Heat Mass Transfer*, 22:1339–1346, 1979.

[25] E. V. Ermanyuk and N. V. Gavrilov. A note on the propagation speed of a weakly dissipative gravity current. *J. Fluid Mech.*, in–press, 2006.

[26] K. M. Faust and E. J. Plate. Experimental investigation of intrusive gravity currents entering stably stratified fluids. *J. Hydraul. Res.*, 22(5):315–325, 1984.

[27] M. R. Flynn and C. P. Caulfield. Natural ventilation in interconnected chambers. *J. Fluid Mech.*, 564:139–158, 2006.

[28] M. R. Flynn and P. F. Linden. Intrusive gravity currents. *J. Fluid Mech.*, 568:193–202, 2006.

[29] M. R. Flynn and B. R. Sutherland. Intrusive gravity currents and internal gravity wave generation in stratified fluid. *J. Fluid Mech.*, 514:355–383, 2004.

[30] A. E. Germeles. Forced plumes and mixing of liquids in tanks. *J. Fluid Mech.*, 71:601–623, 1975.

[31] C. Ghiaus and C.-A. Roulet. Strategies for natural ventilation. In C. Ghiaus and F. Allard, editors, *Natural Ventilation in the Urban Environment*, pages 136–157. Earthscan, 2005.

[32] A. E. Gill. *Atmosphere-Ocean dynamics*. Academic Press, San Diego, 1982.

[33] C. Gladstone and A. W. Woods. On buoyancy-driven natural ventilation of a room with a heated floor. *J. Fluid Mech.*, 441:293–314, 2001.

[34] C. Härtel, L. Kleiser, M. Michaud, and C. F. Stein. A direct numerical simulation approach to the study of intrusion fronts. *J. Eng. Math.*, 32:103–120, 1997.

[35] C. Härtel, E. Meiburg, and F. Necker. Analysis and direct numerical simulation of the flow at a gravity-current head. Part 1. Flow topology and front speed for slip and no-slip boundaries. *J. Fluid Mech.*, 418:189–212, 2000.

[36] P. Heiselberg, Y. Li, A. Andersen, M. Bjerre, and Z. Chen. Experimental and CFD evidence of multiple solutions in a naturally ventilated building. *Indoor Air*, 14:43–54, 2004.

[37] J. Y. Holyer and H. E. Huppert. Gravity currents entering a two-layer fluid. *J. Fluid. Mech.*, 100:739–767, 1980.

[38] P. Howell. Online lecture notes: Waves and compressible flow. *http://www.maths.ox.ac.uk/current-students/undergraduates/lecture-material/B/wcf/pdf/wcf4.pdf*, 2005.

[39] G. R. Hunt, P. Cooper, and P. F. Linden. Thermal stratification produced by plumes and jets in enclosed spaces. *Building Environ.*, 36:871–882, 2001.

[40] G. R. Hunt and N. G. Kaye. Virtual origin correction of lazy turbulent plumes. *J. Fluid Mech.*, 435:377–396, 2001.

[41] G. R. Hunt and P. F. Linden. Steady-state flows in an enclosure ventilated by buoyancy forces assisted by wind. *J. Fluid Mech.*, 426:355–386, 2001.

[42] G. R. Hunt and P. F. Linden. Displacement and mixing ventilation driven by opposing wind and buoyancy. *J. Fluid Mech.*, 527:27–55, 2004.

[43] H. E. Huppert. Geological fluid mechanics. In G. K. Batchelor, H. K. Moffat, and M. G. Worster, editors, *Perspectives in Fluid Mechanics*, pages 289–345. Cambridge University Press, 2000.

[44] H. E. Huppert. Gravity currents: a personal perspective. *J. Fluid Mech.*, 554:299–322, 2006.

[45] N. B. Kaye and G. R. Hunt. Time-dependent flows in an emptying filling box. *J. Fluid Mech.*, 520:135–156, 2004.

[46] J. J. Keller and Y.-P. Chyou. On the hydraulic lock-exchange problem. *J. Appl. Math. Phys.*, 42, 1991.

[47] J. B. Klemp, R. Rotunno, and W. C. Skamarock. On the dynamics of gravity currents in a channel. *J. Fluid Mech.*, 269:169–198, 1994.

[48] C. Kramer and H. J. Gerhardt. Ventilation and heat smoke extraction from industrial buildings. *J. Wind Engng Ind. Aerodyn.*, 29:309–335, 1988.

[49] P. K. Kundu. *Fluid Mechanics*. Academic Press, San Diego, USA, 1st edition, 1990.

[50] Y. Li and A. Delsante. Natural ventilation induced by combined wind and thermal forces. *Building Environ.*, 36:59–71, 2001.

[51] Y. Li, A. Delsante, Z. Chen, M. Sandberg, A. Andersen, M. Bjerre, and P. Heiselberg. Some examples of solution multiplicity in natural ventilation. *Building Environ.*, 36:851–858, 2001.

[52] Y. J. P. Lin and P. F. Linden. Buoyancy-driven ventilation between two chambers. *J. Fluid Mech.*, 463:293–312, 2002.

[53] P. F. Linden. The fluid mechanics of natural ventilation. *Ann. Rev. Fluid Mech.*, 31:201–238, 1999.

[54] P. F. Linden. Convection in the environment. In G. K. Batchelor, H. K. Moffat, and M. G. Worster, editors, *Perspectives in Fluid Mechanics*, pages 289–345. Cambridge University Press, 2000.

[55] P. F. Linden, G. F. Lane-Serff, and D. A. Smeed. Emptying filling boxes: the fluid mechanics of natural ventilation. *J. Fluid Mech.*, 212:309–335, 1990.

[56] P. F. Linden and J. E. Simpson. Microbursts: a hazard for aircraft. *Nature*, 317:601–602, 1985.

[57] B. Lishman and A. W. Woods. The control of naturally ventilated buildings subject to wind and buoyancy. *J. Fluid Mech.*, 557:451–471, 2006.

[58] E. J. List. Turbulent jets and plumes. *Ann. Rev. Fluid Mech.*, 14:189–212, 1982.

[59] Q. A. Liu and P. F. Linden. The fluid dynamics of an underfloor air distribution system. *J. Fluid Mech.*, 554:323–341, 2006.

[60] R. J. Lowe, P. F. Linden, and J. W. Rottman. A laboratory study of the velocity structure in an intrusive gravity current. *J. Fluid Mech.*, 456:33–48, 2002.

[61] R. J. Lowe, P. F. Linden, and J. W. Rottman. The non-Boussinesq lock exchange problem. Part 1: Theory and experiments. *J. Fluid Mech.*, 537:101–124, 2005.

[62] P. C. Manins. Turbulent buoyant convection from a source in a confined region. *J. Fluid Mech.*, 91:765–781, 1979.

[63] P.C. Manins. Intrusion into a stratified media. *J. Fluid Mech.*, 74:547–560, 1976.

[64] T. Maxworthy, J. Leilich, J. Simpson, and E. H. Meiburg. The propagation of a gravity current in a linearly stratified fluid. *J. Fluid Mech.*, 453:371–394, 2002.

[65] A. Mehta, B. R. Sutherland, and P. J. Kyba. Interfacial gravity currents: Part II - wave excitation. *Phys. Fluids*, 14:3558–3569, 2002.

[66] B. R. Morton, G. I. Taylor, and J. S. Turner. Turbulent gravitational convection from maintained and instantaneous sources. *Proc. Roy. Soc. A*, 234:1–23, 1956.

[67] J. Neufeld. Lobe-cleft patterns in the leading edge of a gravity current. Master's thesis, Univ. of Toronto, 2002.

[68] J. C. Phillips and A. W. Woods. On ventilation of a heated room through a single doorway. *Building Environ.*, 39:241–253, 2004.

[69] M. C. Potter and D. C. Wiggert. *Mechanics of Fluids*. Prentice Hall, Inc., Upper Saddle River, NJ, USA, 1997.

[70] C. Pozrikidis. *Numerical Computation in Science and Engineering*. Oxford University Press, New York, NY, 1998.

[71] L. Pratt and J. Whitehead. Online lecture notes. *http://www.whoi.edu/science/PO/dept/scientist/biosketch/PrattSec1.2.pdf*, 2005.

[72] W. H. Press, B. P. Flannery, S. A. Teukolsky, and W. T. Vetterling. *Numerical Recipes: The Art of Scientific Computing*. Cambridge University Press, New York, 2nd edition, 1993.

[73] F. P. Ricou and D. B. Spalding. Measurements of entrainment by axisymmetric turbulent jets. *J. Fluid Mech.*, 8:21–32, 1961.

[74] G. G. Rooney and P. F. Linden. Similarity considerations for non-boussinesq plumes in an unstratified environment. *J. Fluid Mech.*, 318:237–250, 1996.

[75] G. G. Rooney and P. F. Linden. Strongly buoyant plume similarity and 'small fire' ventilation. *Fire Safety J.*, 29:235–258, 1997.

[76] J. W. Rottman and J. E. Simpson. Gravity currents produced by instantaneous releases of a heavy fluid in a rectangular channel. *J. Fluid Mech.*, 135:95–110, 1983.

[77] C.-A. Roulet and C. Ghiaus. Specific devices for natural ventilation. In C. Ghiaus and F. Allard, editors, *Natural Ventilation in the Urban Environment*, pages 136–157. Earthscan, 2005.

[78] M. Santamouris. Energy in the urban built environment: The role of natural ventilation. In C. Ghiaus and F. Allard, editors, *Natural Ventilation in the Urban Environment*, pages 1–19. Earthscan, 2005.

[79] A. H. Schooley. Wake collapse in a stratified fluid. *Science*, 157:421–423, 1967.

[80] A. H. Schooley and B. A. Hughes. An experimental and theoretical study of internal waves generated by the collapse of a two-dimensional mixed region in a density gradient. *J. Fluid Mech.*, 51:159–175, 1972.

[81] J. O. Shin, S. B. Dalziel, and P. F. Linden. Gravity currents produced by lock exchange. *J. Fluid Mech.*, 521:1–34, 2004.

[82] J. E. Simpson. *Gravity Currents in the Environment and the Laboratory*. Ellis Horwood, Chichester, 1987.

[83] J. E. Simpson. *Gravity Currents*. Cambridge University Press, Cambridge, England, 2nd edition, 1997.

[84] K. R. Smith. In *Workshop on the Energy-Environment Nexus: Indian Issues and Global Impacts*. Center for the Advanced Study of India, Univ. of Pennsylvania, 1994.

[85] E. A. Spiegel and G. Veronis. On the Boussinesq approximation for a compressible fluid. *Astrophys. J.*, 131:442–447, 1960.

[86] J. J. Stoker. *Water Waves*. Interscience, New York, USA, 1957.

[87] B. R. Sutherland, M. R. Flynn, and K. Dohan. Internal wave excitation from a collapsing mixed region. *Deep Sea Res. II*, 51:2889–2904, 2004.

[88] B. R. Sutherland, P. J. Kyba, and M. R. Flynn. Intrusive gravity currents in two-layer fluids. *J. Fluid Mech.*, 514:327–353, 2004.

[89] J. S. Turner. Buoyant plumes and thermals. *Ann. Rev. Fluid Mech.*, 1:29–44, 1969.

[90] J. S. Turner. *Buoyancy Effects in Fluids*. Cambridge University Press, Cambridge, England, 1973.

[91] J. S. Turner. Turbulent entainment: the development of the entrainment assumption. *J. Fluid Mech.*, 173:431–472, 1986.

[92] M. Ungarish. On energy balances and Froude number correlations for gravity currents produced by lock exchange. *J. Fluid Mech.*, submitted, 2006.

[93] M. Ungarish and H. E. Huppert. On gravity currents propagating at the base of a stratified fluid. *J. Fluid Mech.*, 458:283–301, 2002.

[94] H. K. Versteeg and W. Malalasekera. *An Introduction to Computational Fluid Dynamics: The Finite Volume Method*. McGraw-Hill, 1st edition, 1995.

[95] T. von Kármán. The engineer grapples with nonlinear problems. *Bull. Am. Math. Soc.*, 46:615–683, 1940.

[96] A. B. D. Wong and R. W. Griffiths. Two-basin filling boxes. *J. Geophys. Res.-Oceans*, 106:26,929–26,941, 2001.

[97] A. W. Woods, C. P. Caulfield, and J. C. Phillips. Blocked natural ventilation: the effect of a source mass flux. *J. Fluid Mech.*, 495:119–133, 2003.

[98] M. G. Worster and H. E. Huppert. Time-dependent density profiles in a filling box. *J. Fluid Mech.*, 132:457–466, 1983.

[99] J. Wu. Mixed region collapse with internal wave generation in a density stratified medium. *J. Fluid Mech.*, 35:531–544, 1969.

[100] C.-S. Yih. *Dynamics of Nonhomogeneous Fluids*. Macmillan, 1965.

[101] E. Zauderer. *Partial Differential Equations of Applied Mathematics*. John Wiley and Sons, New York, 1989.

[102] Y. B. Zeldovich. The asymptotic laws of freely-ascending convective flows. *Zhur. Eksper. Teor. Fiz.*, 7:1463–1465, 1937.